Centre for Geo-Information

Thesis Report GIRS-2007-05

ESTIMATION OF FOREST PARAMETERS USING MULTI-ANGULAR CHRIS/PROBA DATA AND THE LI-STRAHLER GOMS MODEL

Valérie Laurent

April 2007

WAGENINGEN UNIVERSITY
WAGENINGEN UR

Formation des Ingénieurs Forestiers
FIF-ENGREF

Estimation of forest parameters using multi-angular CHRIS-PROBA data and the Li-Strahler GOMS model

Valérie Laurent

Registration number: 83 06 22 504 010

Supervisors:

Prof. Dr. Michael Schaepman (1)

Dr. Michel Deshayes (2)

(1) Wageningen University and Research Centre (WUR)
Laboratory of Geo-Information Science and Remote Sensing
Wageningen, the Netherlands

(2) French Institute of Forestry, Agricultural and Environmental Engineering (ENGREF)
Unité Mixte de Recherche Territoires, Environnement, Télédétection et Informations Spatiales (TETIS)
Montpellier, France

A thesis submitted in partial fulfilment of the degrees of:

- Master of Science at Wageningen University and Research Centre, the Netherlands
- Master of Forestry at the French Institute of Forestry, Agricultural and Environmental Engineering (ENGREF), France

April 2007

Wageningen, the Netherlands

Thesis code number: GRS-80436
Thesis Report: GIRS-2007-05
Wageningen University and Research Centre
Laboratory of Geo-Information Science and Remote Sensing

Foreword

This research constitutes both the thesis for the Master of Geo-Information Sciences at Wageningen University (Wageningen, the Netherlands) and the final internship of my degree of Forest Engineer at the ENGREF (Ecole Nationale du Génie Rural, des Eaux et des Forêts, Nancy, France).

Acknowledgements

First of all, I would like to thank the ENGREF for letting and encouraging me to pursue the Master of Geo-Information Sciences at Wageningen University. I am particularly grateful to Anne Michaut and Christophe Voreux.

I would like to thank Michael Schaepman for proposing me a nice remote sensing thesis topic related to forests when I was not enthusiastic about the topics on the MGI website and Michel Deshayes who accepted to be my ENGREF supervisor.

I am grateful to Jochem Verrelst who was always so enthusiastic about my research and my progresses, even small. He always was always glad to provide advice or to teach me a bit of IDL. It would probably have taken me weeks to write the scripts needed in this study on my own.

I also thank Yuan Zeng who accepted to perform the model inversion on top of her PhD and her job in China. She has been very patient when the image of the proportion of viewed sunlit background was a bit long to come because of a changing methodology and she helped me to understand the Li-Strahler model better.

Raul Zurita-Milla contributed a great deal to the elaboration of the methodology. He kindly provided the Matlab scripts for spatial and spectral unmixing.

Finally, I would like to thank the student of the thesis room for the nice atmosphere I could enjoy while working on my thesis: both relaxed and studious. I guess all of them participated in my work by helping out with either ArcMap or ENVI or giving some ideas about the methodology.

Abstract

The aim of this study is to retrieve pixel-based canopy cover and crown diameter for a boreal mountain forest located in the Swiss National Park to help evaluating the quality of the protection provided by the forest against natural hazards. The methodology involved the use of a radiative forest canopy reflectance model – the Geometric-Optical Mutual Shadowing (GOMS) model of Li and Strahler, high resolution ROSIS and multi-angular CHRIS/PROBA data.

The ROSIS image was classified in 5 classes (sunlit background, sunlit canopy, shadow, riverbed and road). This classification was used to spatially unmix the nadir CHRIS image and retrieve the signatures of the sunlit background, sunlit canopy and shadow endmembers. The 5 CHRIS angular acquisitions were then spectrally unmixed using those 3 endmembers to provide images of the proportion of sunlit background for each viewing angle. Finally, the Li-Strahler model was inverted over the proportion images using stand and tree parameters, viewing and solar angles, slope and aspect data. Since the field measurements could not be obtained simultaneously, the canopy cover and crown diameter reference data was computed, by using LiDAR-derived tree data.

The backward CHRIS viewing angles did not provide realistic results for a sufficient number of pixels and were discarded from the study. The analysis showed that the proportion of sunlit background was underestimated for the nadir viewing angle and overestimated for the forward scatter viewing angles. As a consequence, both the canopy cover and the crown diameter were overestimated for the nadir viewing angle and underestimated for the forward scatter viewing angles. The correlation between the model inversion output and the reference data were very weak. The combination of the inversion outputs for the individual viewing angles did not provide better results. The results were better for the canopy cover (R-squares between 0.01 and 0.13) than for the crown diameter (R-squares between 0.01 and 0.05). The nadir estimate provided the best results for the canopy cover. No best estimate could be distinguished for the crown diameter.

The poor quality of the results might be due to the presence of small trees in the understory, the assumption that the relative illumination and viewing geometry of the ROSIS and CHRIS nadir images were identical, the assumption of Lambertian behaviour of the canopy endmember for the spectral unmixing, the choice of an ellipsoid crown shape and the use of a random distribution to characterize the repartition of the trees over the scene for the model inversion.

Further research should first compare the model outputs to the field data. Then, different crown shapes may be used for the model inversion. It may also be useful to input the pixel tree density. To solve for the non-Lambertian behaviour of the canopy endmember, one could try to simulate the canopy signature for the zenith angles corresponding to the CHRIS acquisition geometry. Finally, to be able to evaluate the quality of the protection provided by the forest, the study area has to be extended to the whole forested area. This should involve the collection of protection, meteorological and soil data.

Keywords:

Conifer forest, canopy cover, crown diameter, hazard protection, multi-angular data, CHRIS/PROBA, Li-Strahler BRF model

Table of contents

List of figures

List of tables

List of appendices

List of acronyms

A9	CHRIS acquisition at 0° theoretical zenith angle
AA	CHRIS acquisition at +36° theoretical zenith angle
AB	CHRIS acquisition at -36° theoretical zenith angle
AC	CHRIS acquisition at +55° theoretical zenith angle
AD	CHRIS acquisition at +55° theoretical zenith angle
BRF	Bidirectional Reflectance Factor
CHRIS	Compact High Resolution Imaging Spectrometer
CC	Canopy Cover
CD	Crown Diameter
DEM	Digital Elevation Model
fAPAR	Fraction of Absorbed Photosynthetically Active Radiation
FAO	Food and Agriculture Organization
GHOST	G-function and HOt SpoT
GOMS	Geometric-Optical Mutual Shadowing
HDRF	Hemispherical-Directional Reflectance Factor
IDL	Interactive Data Language
LiDAR	Light Detection and Ranging
LAI	Leaf Area Index
LWF	Long-term Forest Ecosystem Research
MEA	Millennium Ecosystem Assessment
MISR	Multi-angle Imaging SpectroRadiometer
NaN	Not a Number
NIR	Near Infra Red
POLDER	POLarization and Directionality of the Earth’s Reflectances
PROBA	Project for On-Board Autonomy
RMSE	Root Mean Square Error
ROI	Region Of Interest
ROSIS	Reflective Optics Imaging Spectrometer
SAA	Solar Azimuth Angle
SZA	Solar Zenith Angle
TIFF	Tagged Image File Format
VAA	Viewing Azimuth Angle
VZA	Viewing Zenith Angle
WSL	Swiss Federal Institute for Forest, Snow and Landscape Research

Notations

$A(\theta,\phi,r)$	Area of an ellipsoid of radius r projected at zenith angle θ and azimuth angle ϕ onto the background
$\hat{A}(\theta,\phi)$	Average of $A(\theta,\phi,r)$
b	Half height of the crown
C	Spectral signature of sunlit canopy
E	Column vector containing the error
G	Spectral signature of sunlit background
h	Height of the crown base
j	Low resolution image band number
K	Matrix containing the proportions of each endmember
K_c	Proportion of the pixel area covered by sunlit canopy viewed by the sensor
K_g	Proportion of the pixel area covered by sunlit background viewed by the sensor
K_t	Proportion of the pixel area covered by shadowed canopy viewed by the sensor
K_z	Proportion of the pixel area covered by shadowed background viewed by the sensor
l	Size of the square neighbourhood
m	Treeness parameter
M	Average of the treeness parameter
nb	Number of bands
ne	Number of endmembers
$O(\theta'_i,\theta'_v,\phi,r)$	Overlap function between illumination and viewing shadows of an ellipsoid of radius r projected onto the background = $O(\theta_i,\phi_i,\theta_v,\phi_v,r)$
$\hat{O}(\theta'_i,\theta'_v,\phi)$	Average of the overlap function = $\hat{O}(\theta_i,\phi_i,\theta_v,\phi_v)$
P	Spectral signature of the pixel
P_i	Reflectance of the pixel in band i
r	Crown horizontal radius
R	Average crown horizontal radius for the stand
S	Matrix of the endmembers signatures
T	Spectral signature of shadowed canopy
V(m)	Variance of the treeness parameter
Z	Spectral signature of shadowed background

λ	Density of the trees
Λ	Average number of trees in a pixel
θ_i	Solar zenith angle
θ'_i	Solar zenith angle adjusted for the sphere-shaped crown
θ''_i	Solar zenith angle adjusted for the sphere-shaped crown in the slope coordinate system
θ_s	Slope angle

θ''_s	Slope angle in the slope coordinate system (=0)
θ_v	Viewing zenith angle
$\theta'v$	Viewing zenith angle adjusted for the sphere-shaped crown
θ''_v	Viewing zenith angle adjusted for the sphere-shaped crown in the slope coordinate system
ϕ_i	Solar azimuth angle
ϕ''_i	Solar azimuth angle adjusted for the sphere-shaped crown in the slope coordinate system
ϕ_s	Slope aspect
ϕ''_s	Slope aspect in the slope coordinate system (=0)
ϕ_v	Viewing azimuth angle
ϕ''_v	Viewing azimuth angle adjusted for the sphere-shaped crown in the slope coordinate system

1 Introduction

1.1 Context and background

Forests are an important component of the earth's biosphere; they cover 30 % of the land surface (FAO, 2006). Besides their wide geographic extent, forest ecosystems have a great importance with regard to human well-being: they provide us with a wide range of services such as biodiversity, soil and water protection, supply of wood and non-timber forest products, carbon sequestration and socio-cultural services (MEA, 2005). In addition, forest ecosystems can protect human habitations and activities from natural hazards (Stoffel et al., 2006). This protection service is especially important in mountainous areas where not only floods but also mudslides, avalanches, stone falls and earthquakes can occur (Hewitt, 1992). If the forest management is adapted to take the hazards into account, forests can reduce the frequency and the magnitude of the hazards events and thus reduce the damages caused to humans and their activities (Schönenberger et al., 2005).

First of all, a protection forest has to be dense enough to fix the snow and the ground and to block the falling rocks effectively. Secondly, to resist to storms and to offer a long term protection, the forest has to be stable (Motta and Haudemand, 2000). In practice, this means that the tree density shouldn't exceed a certain threshold. Therefore, tree density is an important forest parameter to ensure a good protection level. When considering the flood hazard, it is necessary to take also the green part of the trees into consideration. Indeed, the leaves physically intercept the rain and they evapotranspirate water absorbed from the ground, increasing the recharge of the groundwater aquifers for the next rain event (Xiao et al., 1998). Therefore, for monitoring purposes, information on Canopy Cover (CC) and Leaf Area Index (LAI) is required. Finally, four parameters are of particular interest when assessing the hazard protection level provided by a forest, namely tree density, standing timber volume, canopy cover and LAI.

Remote sensing techniques are able to retrieve those four parameters over large forest areas. Indeed, canopy cover and LAI were among the first parameters estimated using satellite images, and later, retrieval of stand density was achieved through the inversion of geometric-optical radiative transfer models of the forest canopy, and the standing timber volume can be estimated from LiDAR data. Remote sensing techniques can therefore improve the monitoring of mountainous forests with respect to their protective role, especially in areas that are difficult to access.

New developments in this field involve the use of multi-angular data and canopy radiative transfer models. The combined use of both sources of information is capable of retrieving forest stand parameters. The multi-angular data and the inversion process are described in the next two paragraphs.

1.1.1 Information content of multi-angular data

Multi-angular data represent a set of mono-angular data of the same target acquired from different viewing angles. At the beginning, multi-angular data were obtained by gathering mono-angular data acquired by the sensor over a few overpasses of the target. Many weeks were usually necessary to acquire a sufficient number of images with different viewing geometries. Due to the changes of vegetation, sun geometry and atmospheric conditions, it was very complex to use multi-angular data (Diner et al., 1999). In the 90s, special platforms with a high hinging capacity were built to acquire the multi-angular data. They enable the sensor to take several images from different points of the trajectory during the overpass. The images from the different angles are then acquired in a few minutes, which minimizes the changes of vegetation, sun geometry and atmosphere characteristics. Examples of such remote sensing instruments are: the Multi-angle Imaging SpectroRadiometer (MISR), the POLarization and Directionality of the Earth's Reflectances (POLDER) and the Compact High Resolution Imaging Spectrometer - Project for On-Board Autonomy (CHRIS/PROBA).

Since these data contain directional information in addition to the standard spectral information of remote sensing acquisitions, multi–angular sensors open a wider range of scientific applications in cloud, aerosols, cryosphere and vegetation studies (Diner et al., 1999). It was shown that multi–angular data enables a better discrimination of canopy structural details (Diner et al., 2005) such as foliage clumping index that cannot be calculated using mono-angular data (Chen et al., 2003). In addition, Weiss et al. (2000) showed that using multi-angular data instead of mono-angular nadir data improves the accuracy of the estimates of LAI, the Fraction of Absorbed Photosynthetically Active Radiation (fAPAR), the leaf chlorophyll content and the canopy cover.

1.1.2 The inversion of canopy radiative transfer models

A method to retrieve these forest parameters is to invert a canopy radiative transfer model. A canopy radiative model uses a range of inputs to simulate the spectral signature of a canopy. Model inversion can produce estimates only for the inputs of the model. Before realising the inversion itself, the model has to be calibrated since it uses the measured spectral signatures and the calibrated parameters to calculate the chosen parameter. One can divide canopy radiative transfer models into two categories: 1D or turbid medium models and 3-dimensional or geometric optical models. The 3D models perform better than the 1D models: Le Roux et al. (1997) found that the simulations of the 3D Radiation Interception in Row Intercropping (RIRI) model (Sinoquet and Bonhomme, 1992) matched the field measurements better than the simulations of the turbid Scattering by Arbitrarily Inclined Leaves (SAIL) model (Verhoef, 1984). In addition Asrar et al.(1992) compared Shultis' 1D model (1988) to Myneni's 3D model (1990) and concluded that the reflectance and the fAPAR of a heterogeneous canopy could only be correctly estimated by using the 3D radiative model. The 3D canopy models are able to simulate the Bidirectional Reflectance Factor (BRF) of a scene. They can be inverted over multi-angular data. For example, Lacaze and Roujean (2001) successfully inverted the G-function and HOt SpoT (GHOST) model over muli-angular POLDER data to retrieve the vegetation clumping index.

1.2 Problem definition

Mountain forests are of particular importance for the protection of human lives and activities. The study area was therefore chosen in a mountainous area, namely, in the Eastern Ofenpass valley, located in the East of Switzerland. It was used as a test site to investigate if protection-related forest parameters could be retrieved by inverting a canopy radiative transfer model over multi-angular remote sensing data.

The Li-Strahler Geometric-Optical Mutual Shadowing (GOMS) BRF model (1985; 1992) has been chosen for the study. It was inverted over the multi angular CHRIS data available for the study area. Both the model and the data are further described in section 2.

As aforementioned, the canopy cover is an important parameter to take into account when evaluating the hazard protection level provided by a forest. The code used for the model inversion enabled the retrieval of both canopy cover and crown diameter. Therefore, this study solely focussed on the estimates of canopy cover and crown diameter.

1.3 Research objectives and research questions

The objective of this study was to evaluate the hazard protection level provided by the mountainous boreal forest of the study area by assessing the canopy cover and crown diameter. The performance of the Li-Strahler model inversion to estimate those parameters was evaluated, as well as the added value of the use of multi-angular CHRIS data to produce the estimates. The research questions associated to these goals are:

(A) What is the quality of the protection against natural hazards provided by the mountainous boreal forest of the study area?

(B) How accurately can structural parameters be estimated over a mountainous forest using multi-angular CHRIS data and the Li-Strahler model?

This study used the version of the Li-Strahler model of 1992 which accounts for the mutual shadowing effects. The methodology described by Schaaf et al. (1994) was used to deal with the slope of the study area.

1.4 Report outline

Chapter 2 presents the materials used in the study: the study area, the remote sensing images and the field and elevation data. The Li-Strahler model which was inverted to retrieve the forest structural parameters is extensively described. Chapter 3 describes the methods used to retrieve the results. An important place is given to the methods used to obtain the inputs for the model inversion. Chapter 4 presents the final inversion outputs and the intermediary results of the different steps of the methodology. Chapter 5 discusses the results and the methodology. The conclusions and recommendations for further research are presented in Chapter 6.

2 Materials

2.1 Study area

The study area is located in the Eastern Ofenpass valley, which is part of the Swiss National Park (SNP) (Figure 1). It has been used for a number of environmental studies (Koetz et al., 2004; Morsdorf et al., 2004; Koetz et al., 2005) and is described by Koetz et al. (2004). The Ofenpass represents an inner-alpine valley at an average altitude of about 1900 m above sea level, with an annual precipitation of 900–1100 mm.

Figure 1: Location of the Swiss National Park.

The study area is located on a rather flat area downhill the valley, on the South facing mountainside. Its extent is approximately 1600 by 500 meters. The location and the extent of the study area were chosen in such a way to avoid as much as possible the topographic effects on the results. The study area was selected based on criteria of spatial homogeneity for topographic and illumination conditions. A sensitivity analysis showed that the mean and the standard deviation of the CHRIS reflectances varied very little while raising the slope from 0 to 10.5% and decreasing the illumination from 100 to 85%. A slope of 10.5% and an illumination of 85% were thus chosen as boundary conditions.

Figure 2 shows a situation map of the study area with the plots used during the field work. The data was georeferenced in the Swiss coordinate system whose parameters are given in Appendix 8.1. The study area contains 4 core test sites from the SNP2002 field data campaign (Koetz, 2003): the sites STA 1 and 2 are located in a dense forest area and the sites LWF 1 and 2 are located in a low density area. A plot of the Long-term Forest Ecosystem Research (LWF) is also present in the study area. It is a long term plot used by the Swiss Federal Institute for Forest, Snow and Landscape Research (WSL) in the frame of the Long-term Forest Ecosystem Research program.

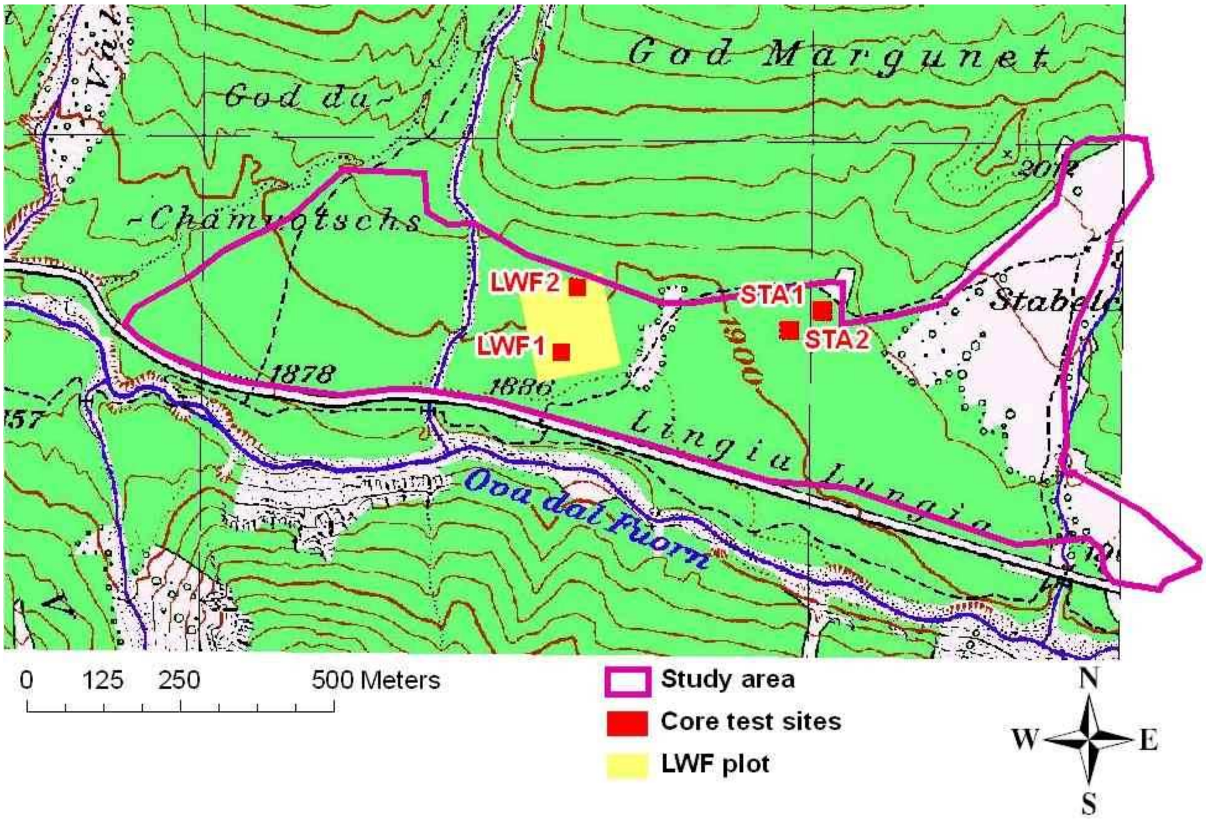

Figure 2: Map of the situation of the study area and of the measurement sites.

The forest of the study area is largely dominated by mountain pine (*Pinus montana ssp. arborea*) and contains some stone pine (*Pinus cembra* L.). The understory is characterized by low and dense vegetation composed mainly of various *Ericaceae* and *Sesleria* species.

The forest of the study area is old. The LWF plot stand has regenerated after a period of clear cutting in the 18th and 19th centuries and has been without any management since the foundation of the Swiss National Park in 1914. The age of the trees ranges from 90 to 200 years, the average being 150 years. More than 20% of the stand is constituted by upright standing dead trees.

2.2 Multi-angular CHRIS data

The CHRIS/PROBA instrument and its capacities are extensively described by Barnsley et al. (2004). CHRIS measures the reflectance of the scene in the spectral wavelength range from 400 to 1050 nm with 18, 37 or 62 spectral bands, at a spatial resolution of either 17 or 34 m. The user can choose between full swath (13 km) and half swath recording. CHRIS is programmed to offer 5 operational modes. These are described in Table 1.

Table 1: Characteristics of the 5 operational modes of CHRIS (Source: Barnsley et al., 2004).

	Swath width	**Spatial resolution**	**Number of spectral bands**	**Intended use**
Mode 1	Full	34 m	62	
Mode 2	Full	17 m	18	studies of water bodies
Mode 3	Full	17 m	18	studies of land surface and atmospheric aerosols
Mode 4	Full	17 m	18	studies of chlorophyll
Mode 5	Half	17 m	37	

Thanks to the hinging capacity of the PROBA platform, CHRIS can acquire up to 5 images from 5 different viewing zenith angles between -60° and +60° from zenith (in theory: ±55°, ±36° and 0°) in a few minutes when passing over the scene.

The 5 images of the study area were recorded on June 27th 2004, in the operational mode 3 of CHRIS, under partly cloudy conditions (1/8th cloud cover). The viewing geometry of the 5 images is shown in Table 2. The position of the sun at the recording moment was characterized by a zenith angle of -24.3º and an azimuth angle of 161.0º. A polar view of the situation is represented in Figure 3. It shows that the AC, AA and A9 images are in the forward scatter direction and the AB and AD images in the backscatter direction.

Table 2: Acquisition geometry of the five CHRIS images as of June 27, 2004.

CHRIS image	Chronological order	Theoretical Zenith Angle (º)	Effective Viewing Zenith Angle (º)	Viewing Azimuth Angle (º)
AC	1	+55	+51.1	357.0
AA	2	+36	+33.3	341.2
A9	3	0	+21.2	315.2
AB	4	-36	-37.8	216.0
AD	5	-55	-54.6	208.9

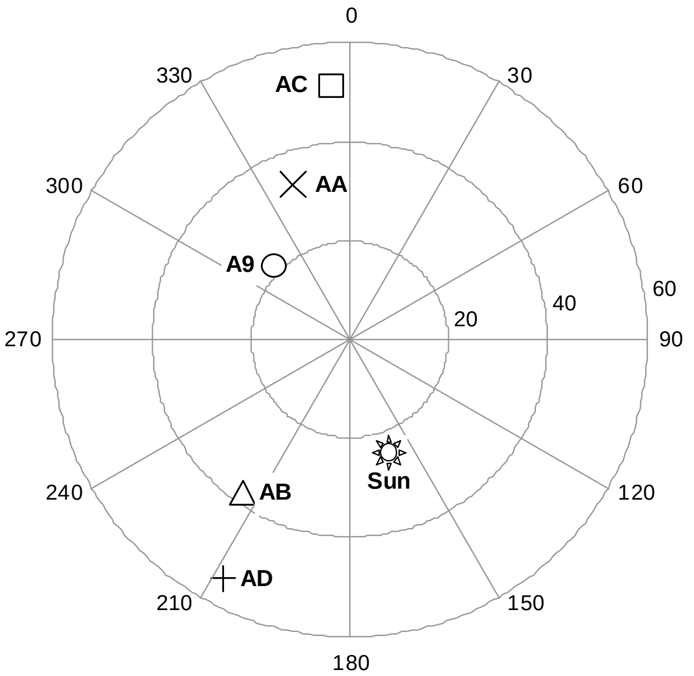

Figure 3: Polar plot of the acquisition geometry of the CHRIS images and of the illumination geometry as of June 27, 2004.

The 5 images have been geometrically and radiometrically corrected by Kneubühler et al. (2005). The result of the preprocessing of the CHRIS data is geo-corrected Hemispherical-Directional Reflectance Factor (HDRF) data, following the reflectance terminology of Schaepman-Strub et al. (2006), with a spatial resolution of 18 meters. The CHRIS images are shown in Figure 4. The AC image presents a big cloud which was masked for the results analyses.

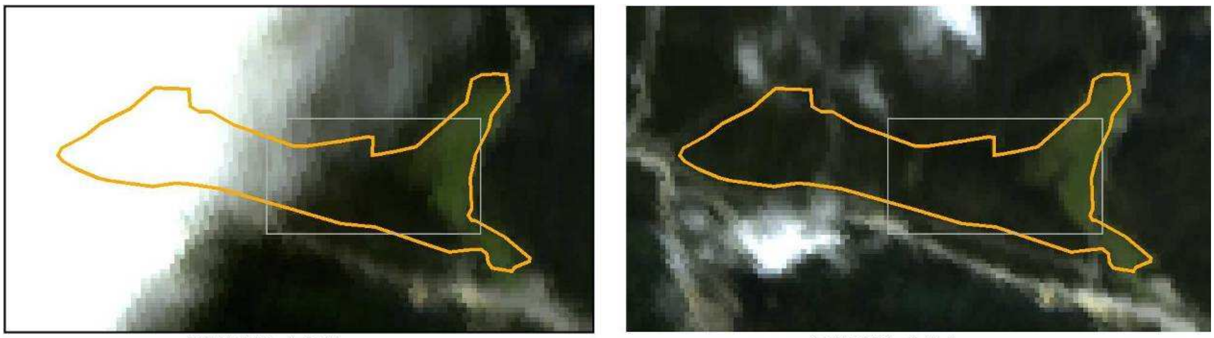

CHRIS AC image **CHRIS AA image**

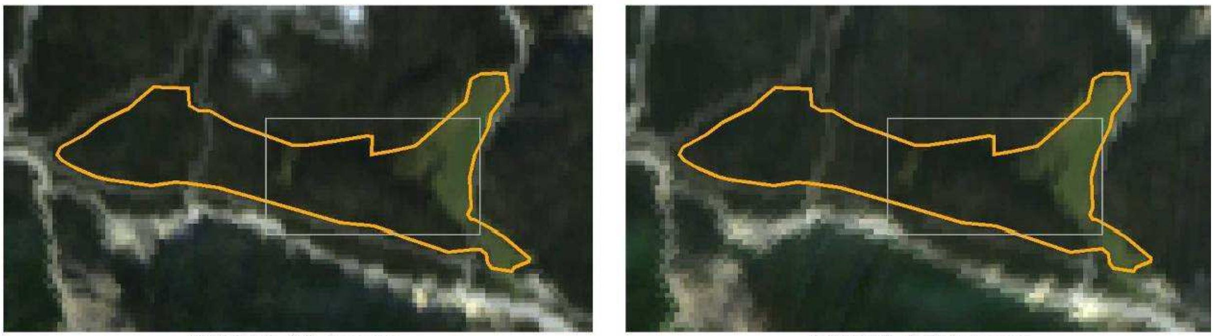

CHRIS A9 image **CHRIS AB image**

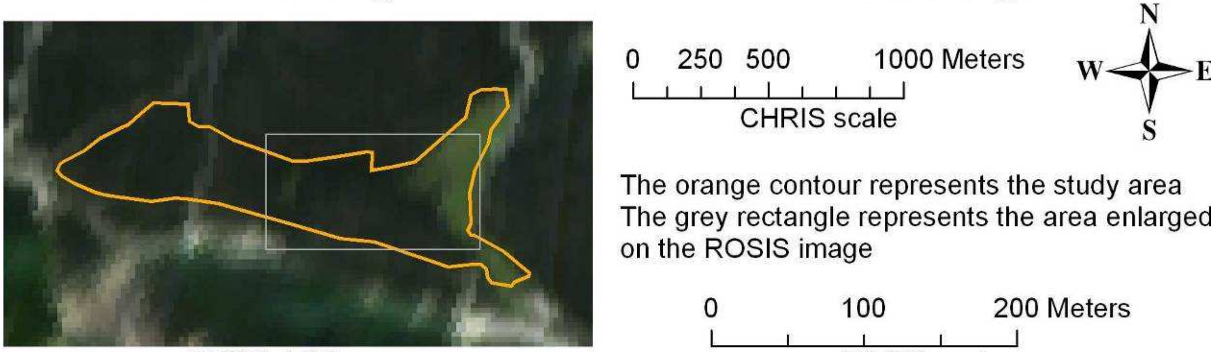

CHRIS AD image

The orange contour represents the study area
The grey rectangle represents the area enlarged on the ROSIS image

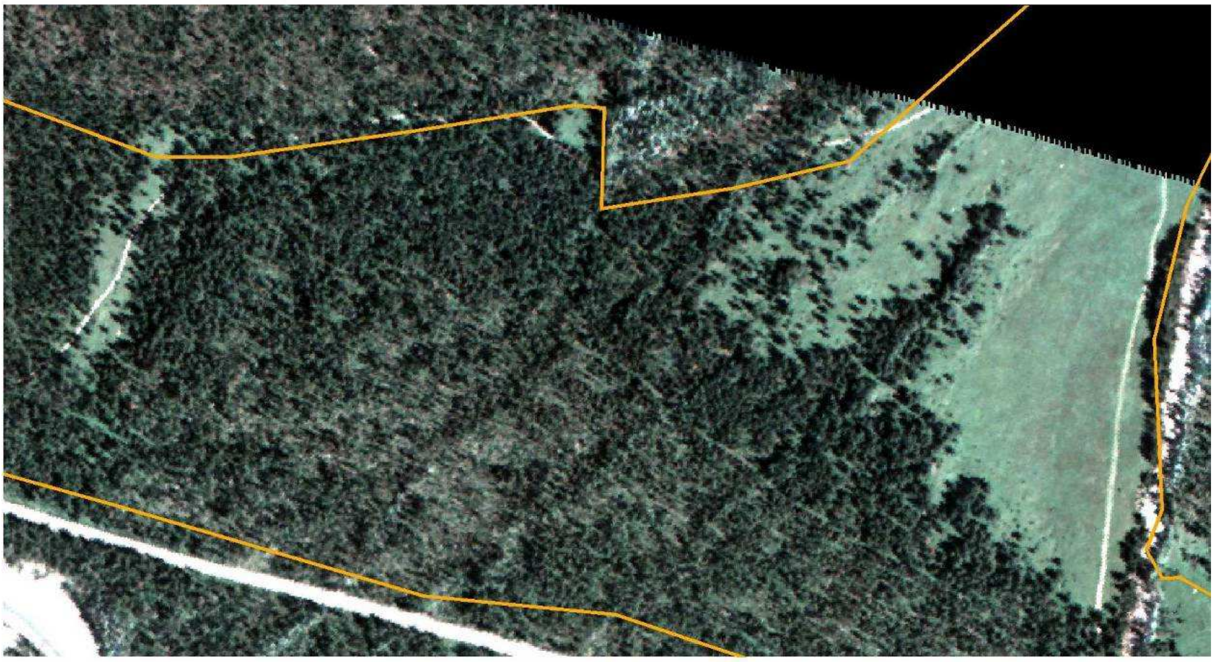

ROSIS image

Figure 4: CHRIS and ROSIS images as used in the study.

2.3 High resolution ROSIS data

The Reflective Optics Imaging Spectrometer (ROSIS) is a pushbroom imaging spectrometer. It records the spectral signal with a 2-dimensional CDD array in 115 spectral bands in the spectral range 430 - 850 nm, with a sampling interval of 4 nm (Schulz and Piepen, 1998).

The ROSIS image of the study area is presented in Figure 4. It was acquired on August 14th 2002. As described by Schaepman et al. (2004), the ROSIS spectrometer was operated onboard of the DLR (German Aerospace Centre) Dornier DO-228 aircraft. The local illumination and observation conditions were a solar zenith angle of 45.3 °, a solar azimuth angle of 122.9 ° and the flight heading of 293 °. There was no cloud coverage at the overflight time. The flight line was oriented close to the principal plane of the sun to minimize the directional effects. The image was geo-atmospherically corrected to obtain geocoded, topographically and atmospherically corrected surface reflectances (Koetz, 2003). The spatial resolution of the ROSIS data is 1m.

2.4 LiDAR data

The Light Detection and Ranging (LiDAR) data of the study area was acquired in October 2002. The helicopter flight covered a total area of about 14 km^2. The LiDAR system used was the Falcon II Sensor developed and maintained by the German company TopoSys. It is a pushbroom laser altimeter recording both first and last reflection from the laser signal on the ground (first/last pulse). The flight was conducted with a nominal height over ground of 850 m, leading to an average point density of more than 10 points per square meter (p/m^2). A smaller subset of the area (0.6 km^2) was overflown with a height of 500 m above ground, resulting in a point density of more than 20 p/m^2, thus, combining the two datasets yields to a point density of more than 30 p/m^2 for both first and last pulse. The LiDAR data and its quality are further described by Morsdorf et al. (2004). In their study, they used the LiDAR data to derivate the geographic location and geometric characteristics of the trees. They validated the results with field data.

In this study, the LiDAR data itself was not used, but the outputs from Morsdorf et al. (2004). Processed altimetric data was provided about more than 18000 trees in the study area. It contained: x and y coordinates, height, crown diameter, crown volume, crown area and height of the base of the crown. This data was used to calculate the ω parameter (see Table 3) and to compute the reference images of canopy cover and crown diameter to check the results of the study.

2.5 Digital elevation model

The terrain topography is described by a Digital Elevation Model (DEM) with a spatial resolution of 18 meters. The DEM was used to correct geometrically both the CHRIS images and the ROSIS data. However, the DEM pixels were not co-registered to the CHRIS data: there was a shift of 9 meters in the x axis and of 5 meters in the y axis. To obtain a DEM co-registered to the CHRIS data, the elevation data was resampled to 1 meter, then cut to the extent of the CHRIS images and aggregated again to 18 meters.

In this study, slope, illumination and aspect data were derived from the DEM, using the topographic modelling possibilities of ENVI. The slope and illumination data were used to define the study area (see paragraph 2.1). The aspect data was used together with the slope data as an input for the inversion of the Li-Strahler model. The slope and aspect images are shown in Appendix 8.2.

2.6 Stand and tree data

Most of the forest stand and tree data was collected on the LWF plot monitored by the Swiss Federal Institute for Forest, Snow and Landscape Research (WSL) in the frame of the Long-term Forest Ecosystem Research program (see the map in Figure 2). The LWF plot contains 2456 trees with a diameter at brEast height larger than 0.12 m over an area of 2 ha. The tree density is 1228 trees/ha. The height of the trees and the crown radius (r) were measured and enabled the retrieval of the mean tree height from ground to mid-crown (h) and the mean crown radius (R). The height of the crown base was visually estimated on the 4 core test sites during the field campaign of August 7-15, 2002. Together with the height of the trees, it enabled the retrieval of the mean half height of the crown (b). The stand and tree data is summarized in Table 3. More details about the collection of this data can be found in (Schaepman et al., 2004).

Table 3: Recapitulative table of the stand and tree characteristics
(Source: Schaepman et al., 2004).

Parameter	Notation	Unit	Value
Tree density	λ	ha^{-1}	1228
Mean half height of the crown	b	m	2.5
Mean horizontal crown radius	R	m	0.882
Coefficient $\omega = \frac{\text{mean}\left(r^2\right)}{\text{variance}\left(r^2\right)}$	ω	m^{-2}	1.235
Mean tree height from ground to mid-crown	h	m	9.5

2.7 GOMS model

2.7.1 Origin and evolution of the model

The Li-Strahler model (1985) is one of the first 3D canopy reflectance models. It was designed to model the nadir or near-nadir Bidirectional Reflectance Factor (BRF) of a conifer forest on a flat terrain. It uses parallel ray geometry to describe the illumination and viewing and it models the conifer trees as solid Lambertian cones casting shadows on a contrasting Lambertian background. The cones are randomly distributed and overlap freely. Geometric calculations are used to calculate the proportion of the following 4 components: sunlit canopy, shadowed canopy, sunlit background and shadowed background in the pixel. Knowing the signature of those four components and the illumination angle, the model calculates the nadir BRF of the pixel.

Li and Strahler (1986) showed that their model could also be used to simulate BRF patterns if extended from nadir viewing to arbitrary illuminating and viewing directions. They did the necessary modifications and they also corrected a weakness of the model of 1985: the assimilation of the trees to opaque cones. With opaque cones, the shadowed areas are black and do not emit any radiation which does not correspond to reality and causes errors when the shadowed areas are viewed by the sensor. Therefore, Li and Strahler modified the model to make the canopy translucent.

In 1992, Li and Strahler (1992) included the mutual shadowing effects in their model, thus obtaining a GOMS model. This enables to better simulate the high brightness of a forested scene when the illumination or/and the viewing directions have large zenith angles. This time, the model was developed with an ellipsoid as the basic crown shape to make the model more generally applicable than the cone shape used in the previous versions.

In 1994, Schaaf and Strahler (1994) extended the model of 1992 to compute the BRF and the Directional Hemispherical Reflectance (DHR) of vegetation on non flat terrain.

The advantages of the Li-Strahler model are that it is invertible, it accounts for mutual shadowing effects at high Solar Zenith Angles (SZA) and it has been proven that the ellipsoid model of 1992 performs better than the cone and cylinder models for North American boreal coniferous forests (Peddle et al., 1999). It has successfully been used in different studies for example to calculate the tree size and density in semiarid woodlands in West Africa (Franklin and Strahler, 1988), to simulate the canopy shadow of semiarid woodlands in California (Franklin et al., 1991), to estimate the tree size of a Californian forest (Woodcock et al., 1994; Woodcock et al., 1997) and to retrieve the crown closure and the crown diameter of the Three Gorges forest in China (Zeng et al., 2007).

2.7.2 The geometric basis of the model

This section describes the model version of 1994 as used in this study. The subscripts i, v and s refer respectively to the illumination, the viewing and the slope angles.

2.7.2.1 The geometric model of the forested scene

Strahler and Jupp (1990) explained that the forest is modelled as a collection trees that are randomly distributed over the scene, following the Poisson law. The trees are represented by an ellipsoid on a stick. Since the trunks are not taken into account in the model, the stick is just a term to represent the height of the ellipsoid above the background; it has a null thickness and does not cast a shadow. The ellipsoids are assumed to be translucent Lambertian surfaces. They cast their shadows on the background, also assumed Lambertian.

Four parameters are necessary to describe the forest: λ = density of the trees, r = crown horizontal radius, b = half height of the crown and h = height of the crown base (Figure 5). Lognormal distributions for the parameters h and r are very typical in forestry and are therefore used in the model.

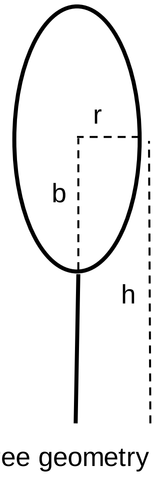

Figure 5: Tree geometry parameters.

2.7.2.2 The four model components

Based on the above description of the forest geometry, the scene can be decomposed into 4 components: sunlit canopy (C), sunlit background (B), shadowed canopy (T) and shadowed background (Z) as depicted in Figure 6.

The scene consists of the four components only, as shown in equation (1). Then, for a given viewing direction, the spectral signature of a pixel is the area-weighted sum of the signatures of the 4 components. This is transposed mathematically in equation (2).

$$K_c + K_g + K_t + K_z = 1 \qquad (1)$$

$$P = K_c C + K_g G + K_t T + K_z Z \qquad (2)$$

Where K_c, K_g, K_t and K_z are the proportions of the pixel area covered by sunlit canopy, sunlit background, shadowed canopy and shadowed background viewed by the sensor, P is the spectral signature of the pixel, C, G, T, and Z are the spectral signatures of sunlit canopy, sunlit background, shadowed canopy and shadowed background (Source: Li and Strahler, 1986).

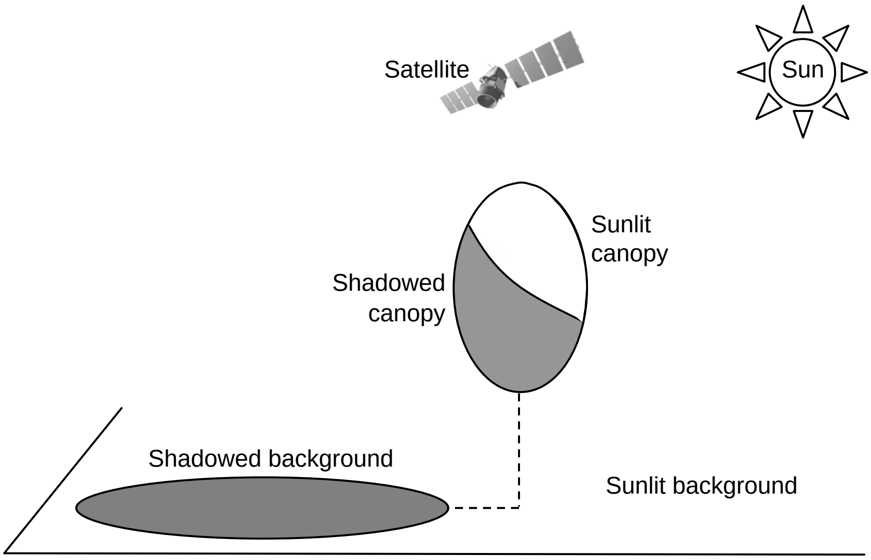

Figure 6: The four components of the Li-Strahler model (Source: Franklin and Strahler, 1988).

Based on geometrics, the proportion of each of the four components can be calculated using forest and tree structural parameters. To invert the model, the proportion of viewed sunlit background (K_g) is of particular interest. It is calculated according to an overlap function, as described in the next paragraph.

2.7.2.3 The proportion of viewed sunlit background and the overlap function

The viewed proportion of each of the four components depends on the size and shape of the tree crowns, on the illumination and viewing angles, on the slope and aspect of the scene and on the degree of overlap of the crowns and components, which is a function of the tree density. Strahler and Jupp (1990) proved that it is possible to estimate the proportion of each component using geometric optics and Boolean models in flat terrain conditions. Here is an overview of the calculation of the viewed sunlit background proportion K_g.

Since the tree distribution is random, the Boolean models can be applied. They show that the gap probability between objects within a layer is $e^{-\lambda \cdot \hat{A}(\theta,\phi)}$ where λ is the density of the object centres on the plane at the base of the layer, θ the zenith angle, ϕ the azimuth angle and

$\hat{A}(\theta,\phi)$ is the average of the function $A(\theta,\phi,r)$ representing the area of a sphere of radius r projected at angles θ and ϕ onto the base of the layer. So the proportion of viewed background is $e^{-\lambda\cdot\hat{A}(\theta_v,\phi_v)}$ and the proportion of sunlit background is $e^{-\lambda\cdot\hat{A}(\theta_i,\phi_i)}$. K_g is the proportion of background that is both viewed and sunlit. It is given by the joint probability of the two events "the point of background is sunlit" and "the point of background is viewed". If those two variables were independent the joint probability would be: $e^{-\lambda\cdot\hat{A}(\theta_i,\phi_i)}\cdot e^{-\lambda\cdot\hat{A}(\theta_v,\phi_v)}=e^{-\lambda\cdot\left[\hat{A}(\theta_i,\phi_i)+\hat{A}(\theta_v,\phi_v)\right]}$. However, the variables are not independent since when illumination and viewing positions are coincident, each sunlit background point is visible and each shadowed background point is not visible. This is what creates the hotspot effect.

The proportion of viewed sunlit background has been proven to be:

$$K_g=e^{-\lambda\cdot\left[\hat{A}(\theta_i,\phi_i)+\hat{A}(\theta_v,\phi_v)-\hat{O}(\theta_i,\phi_i,\theta_v,\phi_v)\right]} \qquad (3)$$

Where $\hat{O}(\theta_i,\phi_i,\theta_v,\phi_v)$ is the mean of the overlap function $O(\theta_i,\phi_i,\theta_v,\phi_v,r)$ between illumination and viewing shadows of the crowns projected onto the background (Source: Strahler and Jupp, 1990).

This expression can be simplified by introducing $\phi=\phi_i-\phi_v$ and the angles θ'_i and θ'_v defined by the function $\tan\theta'=\frac{b}{r}\cdot\tan\theta$. The θ' angles are the zenith angles of the normals to the tangents of the ellipsoid surface at the point of intersection of a ray at angle θ that passes through the ellipsoid centre. This replaces θ_i by the angle θ'_i that would generate the same shadow area if the crown shape was a sphere. Similarly, θ_v is replaced by the angle θ'_v that would hide the same area from view if the crown shape was a sphere. For the nadir view, $A(0,0)=\pi\cdot r^2$, and for the off-nadir view, $A(\theta,\phi)=\frac{A(0,0)}{\cos\theta'}=\frac{\pi\cdot r^2}{\cos\theta'}=\pi\cdot r^2\cdot\sec\theta'$, because the area of the projection of the ellipsoid is the same whatever the azimuth angle ϕ. Thus, $\hat{A}(\theta,\phi)=\pi\cdot R^2\cdot\sec\theta'$ and equation (3) can be re-written as follows (Li and Strahler, 1992):

$$K_g=e^{-\lambda\cdot\pi\cdot R^2\cdot\left[\sec\theta'_i+\sec\theta'_v-\hat{O}(\theta'_i,\theta'_v,\phi)\right]} \qquad (4)$$

Li and Strahler (1992) proved that the exact solution for the overlap function on the principal plane is:

$$\hat{O}(\theta'_i,\theta'_v,\phi)=\frac{1}{\pi}(t-\sin t\cos t)(\sec\theta'_i+\sec\theta'_v) \qquad (5)$$

Where t is given by:

$$\cos t=\frac{h\cdot\left|\tan\theta'_i-\tan\theta'_v\cos\phi\right|}{b(\sec\theta'_i+\sec\theta'_v)} \qquad (6)$$

Kc, Kt and Kz are calculated in the same way as Kg. Equation (2) can then be used to calculate the spectral signature of the pixel for different illumination and viewing geometry, thus yielding BRF patterns. However, these equations do not take the mutual shadowing of the crowns into account and are then only valid for small solar and viewing angles.

2.7.2.4 The mutual shadowing

The mutual shadowing effect happens when the illumination and/or the viewing point are closed to the horizon: at such large zenith angles, the top of the trees are more likely illuminated and visible than the lower portions of the crown. Thus, the scene appears brighter than a model only based on random shadowing would predict. This effect is particularly important in the dense forests where the trees are close to one another. Li and Strahler (1992) developed a methodology to solve this problem. The mutual shadowing equations are important for the retrieval of the BRF at large zenith angles using the forward model, but they are not needed for the model inversion. The calculations are too complex to be presented here. One should retain that the mutual shadowing problem was solved by calculating the true proportion of sunlit canopy viewed by the sensor (K_c) and replacing it in the model calculations. Equation (4) is thus still valid. However, it can only be used for flat forested scenes, which is not the case of the Ofenpass study area. The model has to be adjusted to account for slope and aspect. This is done following the methodology described by Schaaf et al. (1994), as explained in the next section.

2.7.2.5 The slope and aspect

As shown in Figure 7, the slope of the terrain influences the shadowing within the forest: both the shadow of the crown on the background (Figure 7a and b) and the shadowed area within the crown (Figure 7c and d) are bigger on a slope facing away from sun than on a slope facing toward sun. It is then necessary to use the aspect to determine whether the slope faces away or toward the sun.

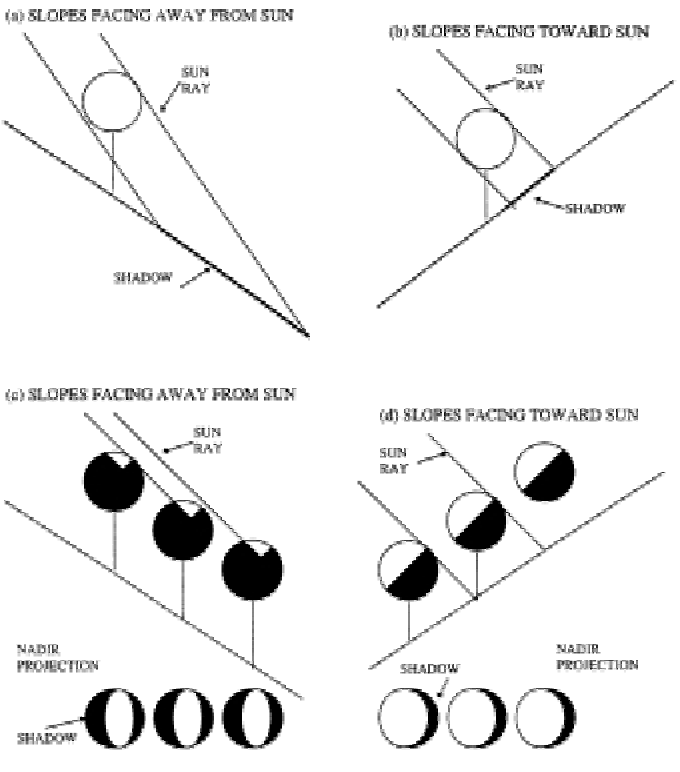

Figure 7: Effect of the slope on the shadowing within a forest stand (Source: Gemmell, 1998).

In the calculations, slope and aspect are accounted for by means of several coordinate system transformations (Schaaf et al., 1994). This process is described here.

Figure 8a shows the starting situation where the geometry is characterised by a slope angle θ_s, slope aspect ϕ_s, solar zenith angle θ_i, solar azimuth angle ϕ_i, viewing zenith angle θ_v and viewing azimuth angle ϕ_v.

The first transformation changes the crown ellipsoids into spheres (see section 2.7.2.3): the angles θ_i and θ_v are replaced by the angles θ'_i and θ'_v which would generate the same shadow area with a spherical crown shape. The situation is depicted in Figure 8b.

Once the crowns are represented by spheres and the trunks ignored, a second transformation converting the entire scene to the slope coordinate system can be performed. The y-axis remains the same and the scene is rotated about it. The slope normal becomes the z'-axis and the x'-axis runs along the slope surface, as drawn in Figure 8c. The slope angle θ''_s and the slope aspect ϕ''_s are set to zero. The solar and viewing zenith and azimuth angles are redefined against the z' and x'-axis to θ''_i, θ''_v, ϕ''_i and ϕ''_v.

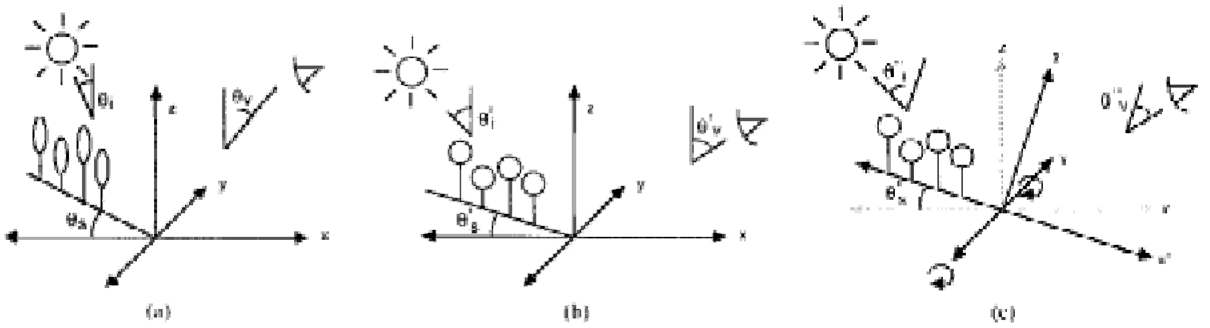

Figure 8: The coordinate transformations required to accommodate a sloping terrain in the Li-Strahler model (Source: Schaaf et al., 1994).

Once the illumination and viewing angles are transformed in the slope coordinate system, the scene with the crown spheres (Figure 8c) can be treated as a flat surface. Equation (4) is then written as:

$$K_g = e^{-\lambda \cdot \pi \cdot R^2 \cdot \left[\sec\theta''_i + \sec\theta''_v - \hat{O}\left(\theta''_i, \theta''_v, \phi\right)\right]} \qquad (7)$$

The reflectance of each pixel for each couple of viewing zenith θ''_v and viewing azimuth ϕ''_v angle are then calculated using equation (7) and the similar equations for Kc, Kt and Kz. These reflectance values are then associated back to the coordinates and viewing angles in the true space (Figure 8b) and finally, to a combination of true view zenith θ_v and true view azimuth ϕ_v angles (situation in Figure 8a) by transforming the crown spheres back into ellipsoids and by adding the slope aspect ϕ_s.

2.7.3 The model inversion

2.7.3.1 The "treeness" parameter

The model inversion is realized by introducing a new variable called "treeness" parameter that enables the retrieval of two forest parameters: the canopy cover and the crown diameter. The treeness parameter, noted m, is defined by Woodcock (1994) as : $m = \Lambda \cdot r^2$, where Λ is the number of trees in the pixel. The quantity $m \cdot \pi$ then represents the area of the pixel that would be covered by the tree crowns if they did not overlap. m is like a crown area index. It is an important parameter in the interface between the remote sensing signal and the forest parameters. The mean of m for a pixel is given by $M = \Lambda \cdot R^2$, where R is the average crown radius for the trees in the pixel. M can be used to re-write equation (7) as follows:

$$K_g = e^{-\pi \cdot M \cdot \left[\sec\theta_i'' + \sec\theta_v'' - \hat{O}\left(\theta_i'', \theta_v'', \phi\right)\right]} \tag{8}$$

Therefore, using equations (5), (6) and (8), M can be inferred as:

$$M = \frac{-\ln\left(K_g\right)}{\left(\sec\theta_i + \sec\theta_v\right) \cdot \left(\pi - t + \cos t \sin t\right)} \tag{9}$$

The variance of m, used later in the computation of the forest parameters (see next paragraph) is calculated over the whole image because its value is too close to zero for single pixels. It is noted V(m).

2.7.3.2 Calculation of canopy cover and crown diameter

Using the treeness parameter, the canopy cover (CC) and the mean crown diameter (CD) can be calculated for each pixel in the image, as shown in equations (10) to (12).

$$CC = 1 - e^{-\pi \cdot M} \tag{10}$$

$$R^2 = \frac{\sqrt{(1+\omega)^2 \cdot M^2 + 4 \cdot V(m) \cdot \omega} - (1+\omega) \cdot M}{2 \cdot \omega} \tag{11}$$

$$CD = 2 \cdot \sqrt{R^2} \tag{12}$$

2.7.3.3 Inputs for model inversion

In this study, the Li-Strahler model was inverted using the code in Interactive Data Language (IDL) of Zeng et al. (2007). It retrieves the pixel based variables forest canopy cover (CC) and crown diameter (CD). Those two parameters can be retrieved using only one component: the sunlit background. In addition, Peddle et al. (1999) found that three components are sufficient to calculate the proportion of sunlit background: sunlit background, sunlit canopy and shadow. The inputs required to invert the model are listed in Table 4. Since the forest of the study area consists of a unique type of forest, only one set of tree characteristics is necessary. The proportion of sunlit background is the input that influences the results most.

Table 4: Input parameters to invert the Li-Strahler model.

	Input parameter	Notation	Unit
Sun geometry	Solar zenith angle	θ_i	Degree
	Solar azimuth angle	ϕ_i	Degree
Viewing geometry	Viewing zenith angle	θ_v	Degree
	Viewing azimuth angle	ϕ_v	Degree
Stand characteristics	Tree density	λ	m^{-2}
	Proportion of sunlit background	K_g	Unitless
Tree characteristics	Mean half height of the crown	b	m
	Mean crown radius	R	m
	Coefficient $\omega = \frac{\text{mean}(r^2)}{\text{variance}(r^2)}$	ω	m^{-2}
	Mean height of the crown base	h	m
Terrain characteristics	Slope	θ_s	Degree
	Aspect	ϕ_s	Degree

The data for this study include multi-angular CHRIS data, a high resolution ROSIS image, forest and tree data from both a field campaign and a LiDAR study and a DEM. These data were processed to produce the inputs to invert the Li-Strahler model, following the methodology described in the next section.

3 Methods

Most of the methodology was dedicated to the retrieval of the images of the sunlit background proportion (K_g) required to invert the model. This is not a straightforward process. Section 3.2 briefly describes the first failed attempt to retrieve the K_g images before presenting extensively the successful methodology. Section 3.3 explains how the inversion of the Li-Strahler model was conducted. Section 3.4 describes the preparation of the reference data. Finally, section 3.5 presents the methodology used to analyse the different results obtained during the study. However, the first methodological step focussed on creating a mask of the forest in the study area.

3.1 Study area forest mask

As seen in section 2.1, the study area was selected based on two criteria: slope less than 10% and illumination more than 85%. A mask fitting those two conditions was built in ENVI and then imported in ArcMap. The scan of the topographic map was imported in ArcMap and georeferenced using 5 ground control points. It was used to avoid the riverbed and the road while drawing the study area polygon. The polygon was then converted to a raster having the same extent (121 x 67 pixels) and the same cell size (18 meters) as the CHRIS subsets using the “To Raster” conversion tool of the Arc toolbox. The raster was exported to the TIFF format so it could be used in ENVI. This TIFF file is the study area mask.

In parallel, Regions Of Interest (ROI) of forest, meadow and riverbed were drawn on the CHRIS A9 subset. They were used to classify CHRIS A9 into 3 classes using the maximum likelihood method. The classified image was used together with the TIFF study area mask to build the study area forest mask in ENVI. The flowchart of these actions is shown in Figure 9.

3.2 The images of the sunlit background proportion

3.2.1 Overview of the two tested methodologies

This section gives a global overview of the two tested methodologies. The general idea of both the first attempt and the final methodology is presented, notably in the form of flowcharts. The steps of the final methodology are extensively described in the following of section 3.2.

3.2.1.1 First methodology

Since the 1 meter resolution of the ROSIS image enables to find pure pixels of sunlit canopy, sunlit background and shadow, it was resampled to the CHRIS spectral bands and used to collect the signatures of those 3 endmembers. However, the magnitudes of the ROSIS and CHRIS reflectance values are different. Following Hall et al. (1991), the signatures of a forest ROI in both ROSIS and CHRIS A9 image were used to calculate a scaling factor for each band. The endmembers signatures obtained from the ROSIS image were then multiplied by the scaling factors to scale them to the CHRIS magnitude. The CHRIS A9 image was then spectrally unmixed using the scaled endmembers signatures, thus yielding the image of the sunlit background proportion. A flowchart of this method is shown in Appendix 8.3.

Unfortunately, the unmixing results were not successful. The proportion images of the endmembers presented in Appendix 8.4 (left column) show that the spatial patterns of sunlit canopy and sunlit background are “complementary”: K_g is null where K_c is non null and the other way around. This indicates that the signatures of sunlit canopy and sunlit background are too close and cannot be unmixed. The analysis of the signatures of each point ROI of sunlit background revealed 2 groups of ROIs. The group with the lower reflectance values and thus closer to the signature of the sunlit canopy was excluded from the sunlit background ROI, raising its signature. The second unmixing did not provide better results (see Appendix 8.4, right column). Therefore, another methodology was implemented to obtain the K_g images.

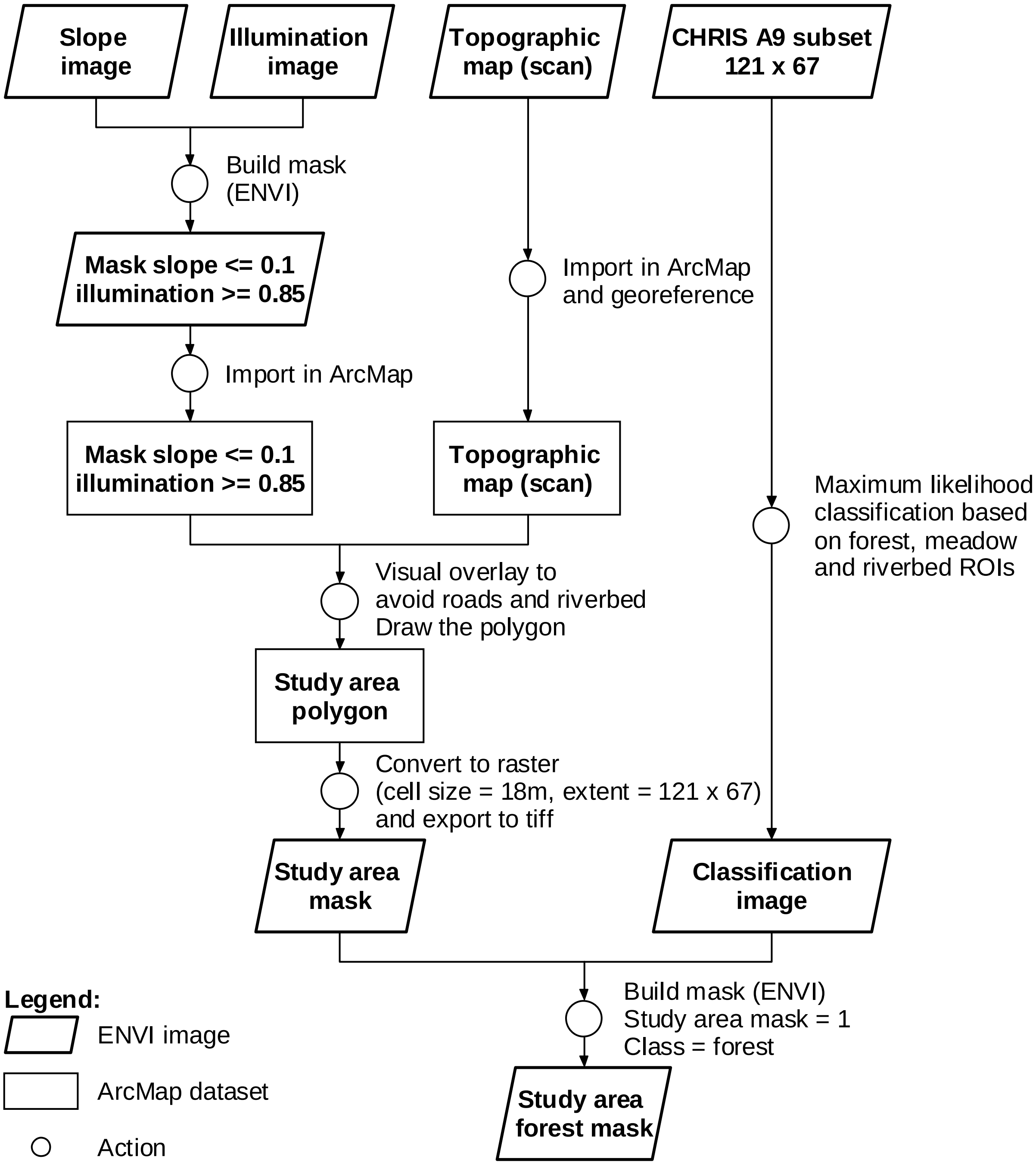

Figure 9: Flowchart of the preparation of the study area forest mask.

3.2.1.2 Final methodology

This method encompassed classifying the high resolution ROSIS image to spatially unmix the CHRIS image and thus yield the endmembers signatures directly from the CHRIS A9 image.

After removing the noisy bands and resampling the ROSIS data to the CHRIS spectral bands, the ROSIS image was classified in 5 generic classes: shadow, sunlit background, sunlit canopy, riverbed and road. Then, to perform the spatial unmixing, the classification and the CHRIS A9 image were resized to exactly the same geographic extent. The CHRIS signatures of the sunlit canopy, sunlit background and shadow endmembers could then be retrieved. The 5 CHRIS images were resized to the study area extent and to 12 bands before being spectrally unmixed, thus yielding the images of the proportion of the sunlit background. This methodology is extensively described in the following and its flowchart is shown in Figure 10.

3.2.2 Retrieval of the CHRIS endmembers signatures: spatial unmixing

3.2.2.1 ROSIS data preparation

A visual examination of the individual bands of the ROSIS image revealed the presence of some noisy bands, especially in the short wavelengths. Koetz (2003) used three methods to identify them. His results are shown in Table 5. The visual analysis considers the first 15 bands as noisy. The correlation matrix shows low correlation between the first 15 bands, revealing that they are affected with high noise. The signal to noise ratio calculated for the homogeneous Stabelchod meadow was less than 10 for the first 32 bands. In this study, the ROSIS data is used to obtain a classification at 1 m resolution. For this purpose, it was preferred not to use any noisy band in order to improve the classification result. In the end, the first 32 bands were removed.

Table 5: Noisy band list of the ROSIS image (Source: Koetz, 2003).

Deficiency	Noisy bands
Visual striping	1 to 15
Correlation matrix	1 to 15
Signal to noise ratio < 10	1 to 32

In addition, the analysis of a number of spectral signatures revealed the presence of a narrow pit about 0.760 µm. It does not correspond to a water absorption feature and its origin is unknown. So the bands involved in this pit, bands 82 to 86, were discarded. The first 15 bands were already not present in the ROSIS data file provided for this study: there were 100 bands instead of 115. So the only the first 17 bands and bands 82 to 86 were removed.

For the sake of consistency, it was decided to decrease the number of ROSIS bands by resampling the ROSIS data to the CHRIS bands. The spectral range of the ROSIS data was smaller than the one of CHRIS, especially after removing the noise. The resampled ROSIS data had only 12 bands which correspond to bands 3 to 14 of the CHRIS data.

3.2.2.2 Classification of the ROSIS image

Peddle et al. (1999) and Schaaf et al. (1994) showed that one endmember for both shadowed canopy and shadowed background is sufficient to retrieve the sunlit background proportion. Therefore, the ROSIS image was classified into 5 classes: sunlit canopy, sunlit background, shadow, riverbed and road, using the maximum likelihood classifier.

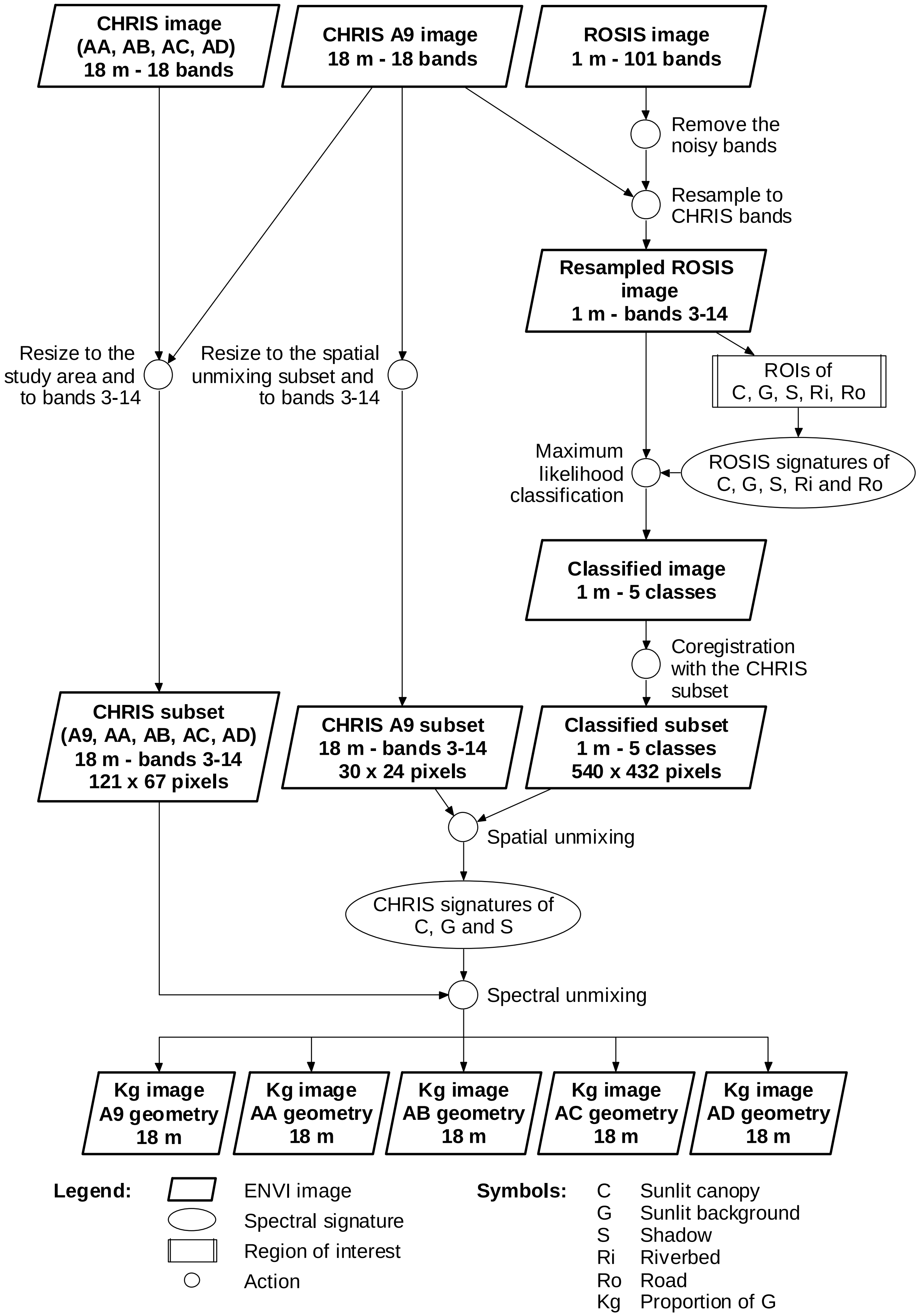

Figure 10: Flowchart of the methodology to obtain the images of the proportion of sunlit background.

The endmembers were collected from ROIs. The points from the shadow ROI were collected in the dark areas. The sunlit canopy points were collected among the bright tree pixels, preferentially located in the South Eastern part of the tree, since the sun was in the South East of the study area at the recording time. The ROI for the sunlit background included both pixels from the meadows and from the bright West-East "paths" in the forest. The classes riverbed and road were solely used to locate the non-forest pixels which are also of importance for the spatial unmixing (see paragraph 3.2.2.3). Figure 11 shows the endmembers signatures.

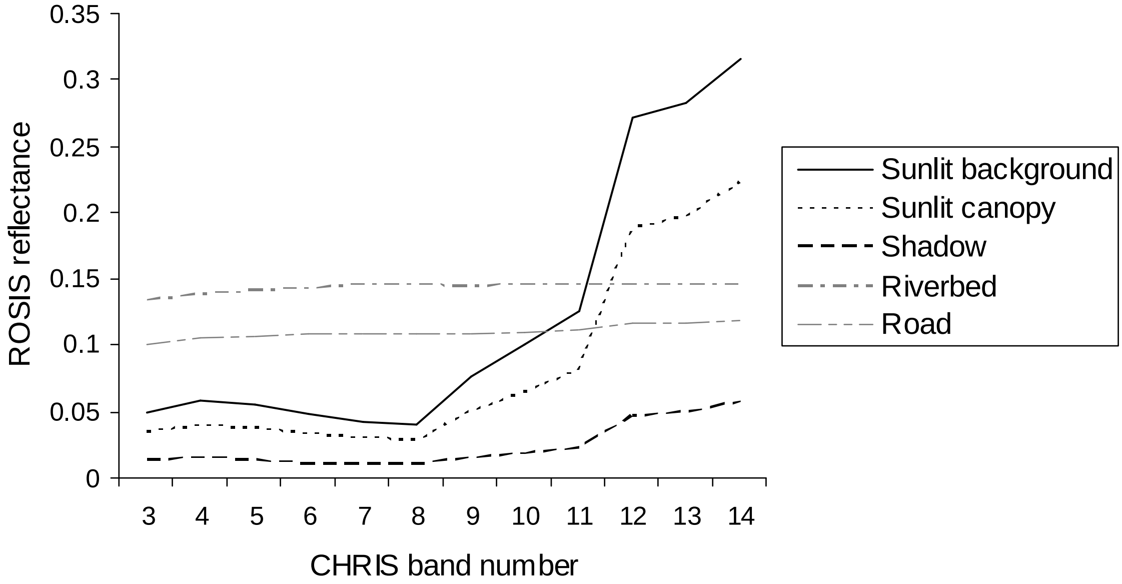

Figure 11: Signatures of the five endmembers used to classify the ROSIS image.

3.2.2.3 Retrieval of the endmembers signatures: linear spatial unmixing

Let 'ne' represent the number of endmembers. Assuming that the scene is composed of exactly 'ne' endmembers and that each endmember contributes linearly to the pixel signature, the general equation of spectral mixing can be written as:

$$P = \sum_{e=1}^{ne} K_e \cdot S_e \qquad \text{where} \qquad \sum_{e=1}^{ne} K_e = 1 \qquad (13)$$

where P is the pixel signature, ne the number of endmembers, K_e the proportion of the e^{th} endmember in the pixels and S_e the spectral signature of the e^{th} endmember.

The linear spatial unmixing of the CHRIS A9 image can retrieve the endmembers signatures if the endmembers proportions are known. Those proportions can be derived thanks to the classified ROSIS image. Indeed, one CHRIS pixel can be matched with 324 (=18*18) ROSIS pixels. Thus, the proportion of a given endmember is the number of pixels classified as this endmember in a CHRIS pixel divided by 324. It is therefore crucial that the ROSIS and CHRIS data are properly coregistered. In addition, to perform the spatial unmixing, it was necessary to assume that the viewing and illumination conditions of the CHRIS A9 image and ROSIS acquisitions were similar. This is why the CHRIS near-nadir A9 image was chosen among the 5 CHRIS scenes: its viewing conditions were closest to the ones of the ROSIS image.

The linear spatial unmixing was run according to the image fusion approach of Zurita-Milla et al. (2006). The fusion process consists of three different phases:

a) Computation of the proportions of each endmember in each pixel of the low resolution image using the high resolution classification image,
b) Computation of the endmembers signatures using the low resolution image and
c) Composition of the fused image with the spatial resolution of the high resolution image and the spectral resolution of the low resolution image.

The spatial unmixing problem was solved band per band, for a given neighbourhood size of the low resolution image, as shows equation (14).

$$P_j^{l^2} = K^{l^2,ne} \cdot S_{j,l}^{ne} + E_j^{l^2} \qquad (14)$$

where j is the low resolution image band number ($j \in [3;14]$), l the size of the square neighbourhood, ne the number of endmembers, P is a l^2 column vector containing the reflectance values in band j for each low resolution pixel in the neighbourhood, K is a (l^2xne) matrix containing the proportions of each endmember in each low resolution pixels in the neighbourhood, S is the unknown ne-column vector of the endmembers reflectances in band j and E is the l^2 column vector of the residual error of the pixels in the neighbourhood.

For a given band j, if no neighbourhood is taken into account (l=1), then there are n unknowns (the n reflectance values of the n endmembers in band j) for one equation, and (14) cannot be solved. The use of the neighbourhood of l by l pixels is to provide more equations in order to be able to solve (14). In the image fusion case, it is interesting to keep l as small as possible to preserve as much as possible the spectral information of the low resolution image in the fused output image. However, in the context of this study, the goal of the spatial unmixing was to retrieve endmembers signatures that are valid for the entire study area. Therefore, the neighbourhood was chosen as large as possible: equal to the entire CHRIS subset. This approach consisting in using the entire image was also used by Strahler and Jupp (1990).

The images for the spatial unmixing cannot contain any pixel that is not a number (NaN). Given the oblique shape of the ROSIS scene, the biggest subset that could be used had an extent of 540 by 432 meters (see Appendix 8.5 for the coordinates of the subset). In the end, the steps a) and b) were performed using the subsets to compute the signatures sunlit canopy, sunlit background and shadow using the entire subset as the neighbourhood.

3.2.3 Retrieval of the sunlit background proportion images: linear spectral unmixing

Like the spatial unmixing, the spectral unmixing was based on equation (13). However, here the goal was to retrieve the endmembers proportions K_j in each pixel. To reach this goal, it was necessary to know the endmembers spectral signatures.

The linear spectral unmixing was realized according to Zurita-Milla et al. (2007). Thus, Equation (13) had to be rewritten in matrix notations as shown in equation (15).

$$P^{nb} = S^{nb,ne} \cdot K^{ne} + E^{nb} \qquad (15)$$

where nb is the number of bands, ne is the number of endmembers, P^{nb} is the nb-column vector containing the reflectance values of the pixel in the nb bands, $S^{nb,ne}$ is the (nbxne) matrix containing the ne endmembers signatures reflectance values in the nb bands, K^{ne} is the unknown ne-column vector containing the proportions of the ne endmembers and E^{nb} is the nb-column vector containing the spectral error for the nb bands.

The fully constrained option was chosen to perform the linear spectral unmixing because it restricts the solutions for the endmembers proportions in the plausible physical domain: the proportions have to be positive, smaller than one and they have to sum up to one, as described mathematically in equations (16) and (17). The constrained approach was also chosen by Strahler and Jupp (1990).

$$0 \le K_e \le 1 \text{ where } e \in [1; ne] \tag{16}$$

$$\sum_{e=1}^{ne} K_e = 1 \tag{17}$$

where ne is the number of endmembers and K_e is the proportion of the endmember e.

Because of the set of inequalities in (17), the linear spectral unmixing was done by solving a constrained lEast squares problem. The solution for the proportions vector K has to yield the smallest possible residual error. The proportion of each endmember and the spectral Root Mean Square Error (RMSE) were calculated for each pixel. The RMSE represents the mean reflectance error by band, as shows equation (18). However, this measure is not handy to compare the RMSE between pixels. Therefore, a percentage RMSE was calculated using equation (19).

$$RMSE = \frac{\sum_{i-1}^{nb} E^{nb}(i)}{nb} \tag{18}$$

$$RMSE\ \% = \frac{RMSE}{\frac{1}{nb} \cdot \sum_{i=1}^{nb} P^{nb}(i)} \tag{19}$$

Prior to performing the spectral unmixing, the five CHRIS scenes were resized to fit the study area extent. The subsets used have an extent of 121 samples by 67 lines, being 2178 by 1206 meters. The map coordinates used to delineate the subsets are given in Table 6.

Table 6: Map coordinates delineating the study area subsets for the five CHRIS scenes.

	Upper left corner	**Lower right corner**
x coordinate (m)	812700	814878
y coordinate (m)	172260	171054

Assuming that the endmembers signatures do not depend on the viewing angle (assumption of Lambertian behaviour) and that only their proportions are different, the 5 CHRIS subsets were spectrally unmixed using the endmembers signatures of sunlit canopy, sunlit background and shadows from the spatial unmixing (paragraph 3.2.2). Since only three “forest” endmembers were considered, the non forest pixels yielded irrelevant proportions and were therefore masked.

In addition, only the spectral bands 3 to 14 were used to perform the fully constrained spectral unmixing. Bands 1-2 (blue) and bands 15-18 (water absorption) were discarded because they contain less relevant information about vegetation and possibly bring some noise in the unmixing. As a result, for the 5 CHRIS images, the mean of the percentage RMSE (see next paragraph for the definition) for the forest in the study area decrease from 0.089 to 0.070 of when using only bands 3 to 14.

3.3 The inversion of the Li-Strahler model

The model inversion was done according to Zeng et al. (2007), for each CHRIS viewing angle. It enabled the retrieval of crown diameter (CD) and canopy cover (CC) from the input data, as shown in Figure 12. A recapitulative of the input data with their values and associated images is presented in Appendix 8.2.

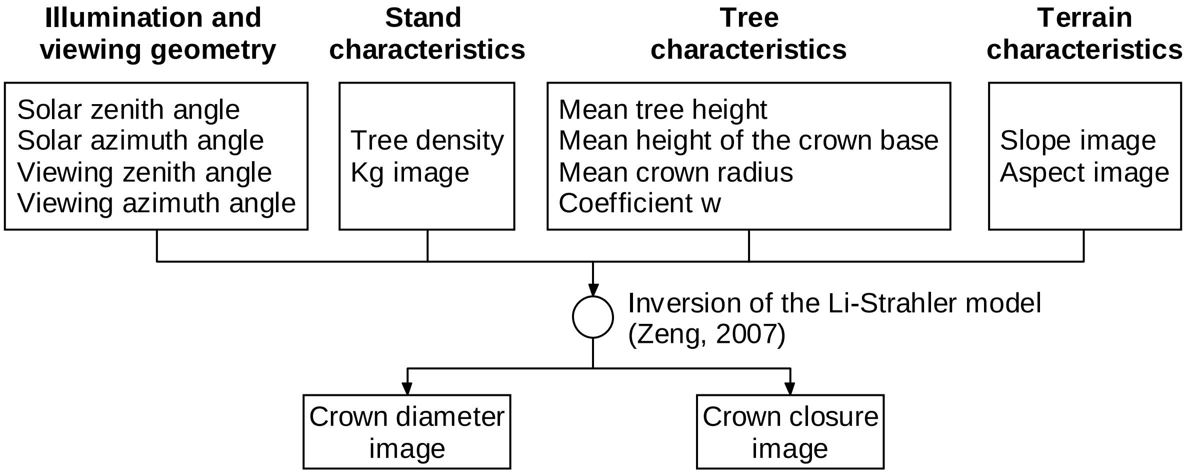

Figure 12: Flowchart of the model inversion.

Thresholds were used to avoid unrealistic results: the canopy cover is restricted to the interval [0;1] and the crown diameter was assumed to vary in the interval [0;14]. If the model outputs were beyond these ranges, the pixel was set to NaN. The pixel value was also NaN when its Kg is null, because of the logarithm used in the calculation of the mean of the treeness parameter M (see paragraph 2.7.3.1).

3.4 Preparation of the reference data

Two reference images were created from the tree data described in section 2.4: one for the canopy cover and one for the crown diameter. The tree data was imported into ArcMap using the x and y coordinates recorded with the tree parameters. A shapefile with one point per tree was then created, as well as an attribute table containing the tree parameter values. Since the canopy cover has a surface dimension whereas the crown diameter data is linked to the point location of the tree, two distinct methodologies had to be implemented to obtain the canopy cover and crown diameter images.

3.4.1 The canopy cover image

To obtain the canopy cover image from the derived LIDAR data, it was necessary to compute the area covered by tree crowns in each pixel. First, a buffer was created around each point using the crown radius from the attribute table. During the processing, the discs were dissolved to remove any overlap between the crowns, creating a unique multipart polygon which represents the canopy.

In order to overlay this polygon with the pixels squares, a shapefile containing squares polygons corresponding to the pixels had to be created. The shapefile was obtained by converting a raster with 121*67 different values (from 1 in the upper left corner to 8107 in the lower right corner) to polygon features.

The multipart canopy polygon was then intersected with the pixels squares polygons, yielding a shapefile containing one multipart canopy polygon for each pixel. The area of those polygons was calculated and then divided by 324, which is the area of the 18 by 18 meters pixels. Those two parameters were stored in new fields in the attribute table. Finally, the shapefile was exported to a TIFF file, using the canopy cover field to fill in the image. A flowchart describing the different steps is presented in Figure 13.

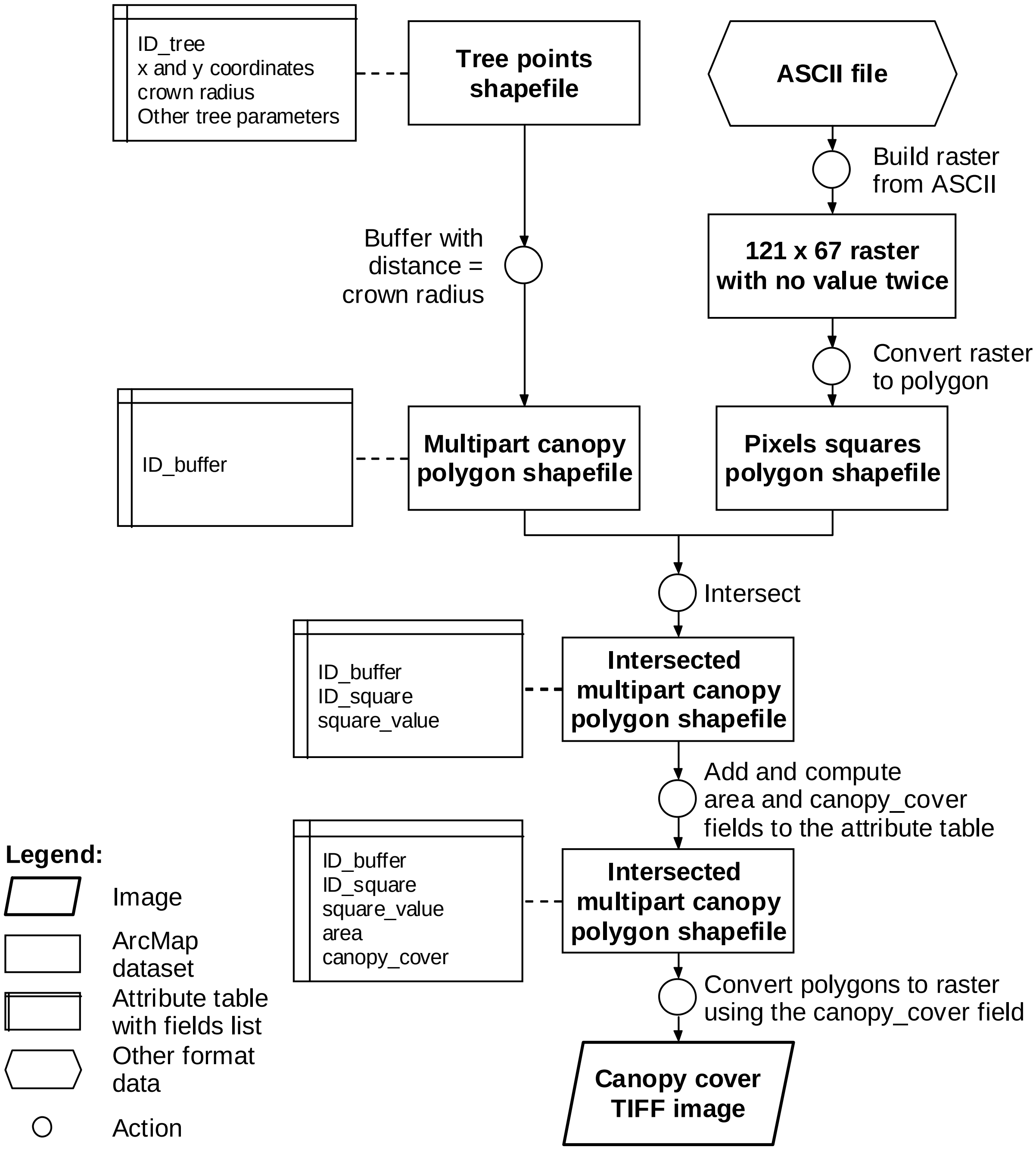

Figure 13: Flowchart of the preparation of the canopy cover reference image.

3.4.2 The crown diameter image

The crown diameter image represents the mean crown diameter of the trees located in the pixel. It was created thanks to a custom tool using twice the “Point Density” function from the Spatial Analyst Toolbox. This function calculates the density of point features around each output raster cell. The input parameters include a “population field” whose value determines the weight the point, the output cell size, the neighbourhood shape and the neighbourhood size. The neighbourhood shape was set to “rectangle” and the neighbourhood height and neighbourhood width were set to 1 cell in order to count only the points that are inside the pixel. Setting the other parameters to the values indicated in Figure 14, the “Point Density” function was used to compute a raster of the tree density (“number of trees per square meter”) and a raster of the crown diameter containing the sum of the diameter of the trees in the pixel per square meter (“sum diameter per square meter”). Finally, the “sum diameter per square meter” was divided by the “number of trees per square meter” to provide the mean crown diameter in the pixel.

In addition, the “sum diameter per square meter” raster was transformed into a raster of the number of trees per pixel to give a better idea of the density of the stand and to support the analysis of the results. It is presented in Appendix 8.5.

Finally, the rasters were transformed to an ENVI format and the no data pixels were set to “NaN”. The script used to perform this step is presented in Appendix 8.7.1.

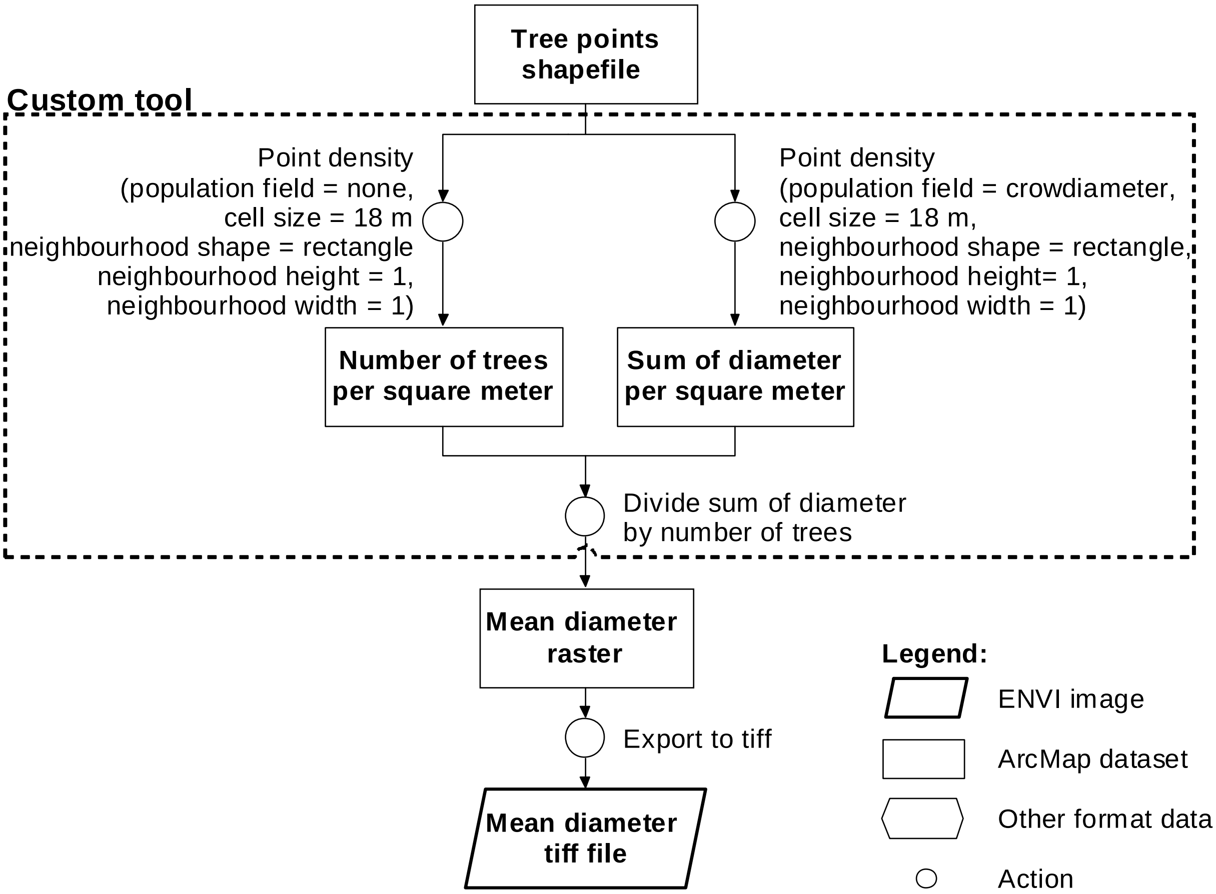

Figure 14: Flowchart of the preparation of the crown diameter reference image.

3.5 Methods for the analysis of the results

3.5.1 Confusion matrix and accuracy of the classification of the ROSIS image

The confusion matrix of the classification was calculated using the so-called “ground truth ROIs”. The ground truth ROIs were visually selected on the ROSIS image. For each class, the number of points in the ROI was proportional to the number of pixels in this class on the classified image.

Based on the confusion matrix, the overall accuracy, the producer’s and user’s accuracy and the omission and commission errors were calculated, as well as the Kappa coefficient. The latter indicates the percentage of errors avoided by the classification, compared to a random classification.

3.5.2 Validation samples for the analysis of the results

The validation sample had to cover only pixels included in the forest of the study area and having values for the output image of each viewing angle and for the two reference images. Those pixels were selected using the script presented in Appendix 8.7.2.

Since the pixel size is rather small, an error of one tree per pixel can result in non-negligible differences in the canopy cover and mean crown diameter of the pixel. Therefore, it was chosen to analyse the results based on squared samples of 2 by 2 pixels. This approach aggregating the pixels in a square window to validate the results was also used by Zeng et al. (2007). Because of the irregular shape of the usable area obtained in the previous step, the outputs were not resampled, but squared ROIs were drawn. There were 79 validation samples ROIs. They are presented in Appendix 8.8. The mean value of either canopy cover or crown diameter were calculated per validation sample for the model outputs and the reference images and used to calculate the Pearson R, R-square and RMSE of the correlation between the reference data and the model outputs.

4 Results

4.1 Intermediary results

4.1.1 ROSIS classification

The output of the maximum likelihood classification of the ROSIS image is presented in Figure 15. The classes road and riverbed have been merged to represent a single non-vegetation class.

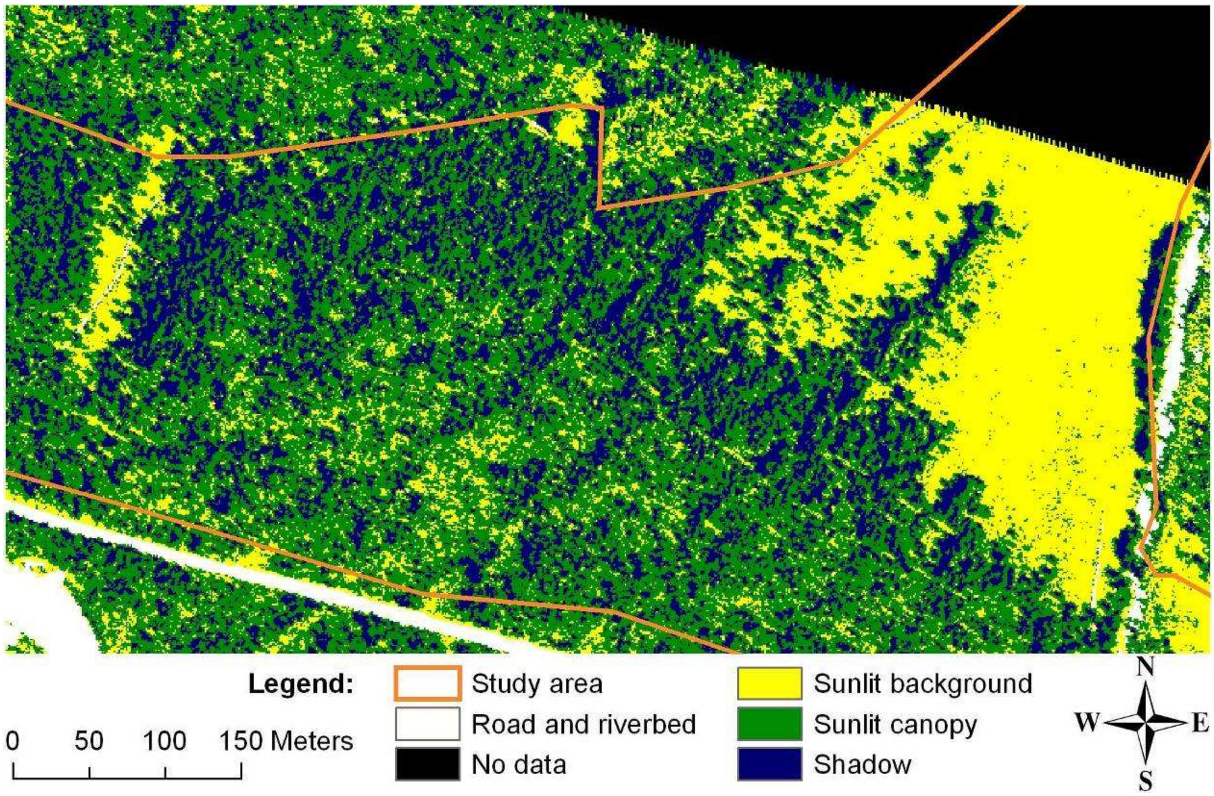

Figure 15: Classification of the ROSIS image in four classes: the three components of the Li-Strahler model and the non vegetated areas.

A visual examination of the classification as compared to the RGB ROSIS image revealed a good overlap of the patterns of the different classes. The good quality of the classification was confirmed by the confusion matrix presented in Appendix 8.9. The overall accuracy of the classification was 92.6%, meaning that 92.6% of the ground truth pixels were put in the correct class. The Kappa coefficient was 0.89. For all the classes, the producer's accuracy was higher than 87% and the user's accuracy was higher than 75%.

4.1.2 Endmembers signatures from the spatial unmixing

The spatial unmixing technique enabled the retrieval of the endmember signatures in terms of CHRIS reflectances. The signatures of sunlit background, sunlit canopy and shadow are shown in Figure 16.

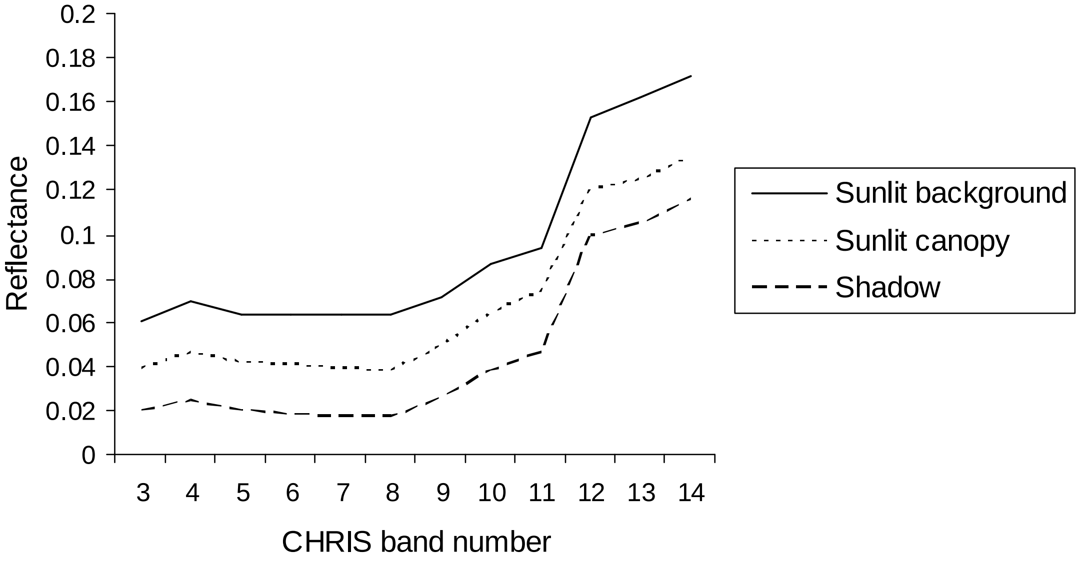

Figure 16: CHRIS signatures of the 3 endmembers derived from the spatial unmixing.

4.1.3 Spectral unmixing results and sunlit background proportion images

The output of the spectral unmixing were the images of the proportions of sunlit background, sunlit canopy and shadow and the image of the RMSE, expressed as a percentage of the total reflectance of the pixel for the five CHRIS viewing angles.

4.1.3.1 Spectral unmixing results for the A9 viewing angle

Figure 17 presents the results for the A9 viewing angle. A visual examination of the proportion images shows that the results are coherent with reality: the proportion of sunlit background is high in the meadow while the proportion of sunlit canopy is high in the forest. Shadow is present in all the forest, but its proportion is higher in the dense stand than in the stands that have a lower density, which also makes sense. One can refer to the map of the stand density in Appendix 8.5.

Since no field data is available to validate the proportion images, the RMSE is the only quality indicator of the spectral unmixing. One can see on Figure 17 that the patterns of high RMSE percentage correspond to the meadow, the road and the riverbed, which were not taken into account in the analysis of the model inversion outputs. The RMSE percentage of the study area forest was below 10%. The Western part (3 to 10%) had a higher RMSE than the Eastern part (0 to 5%).

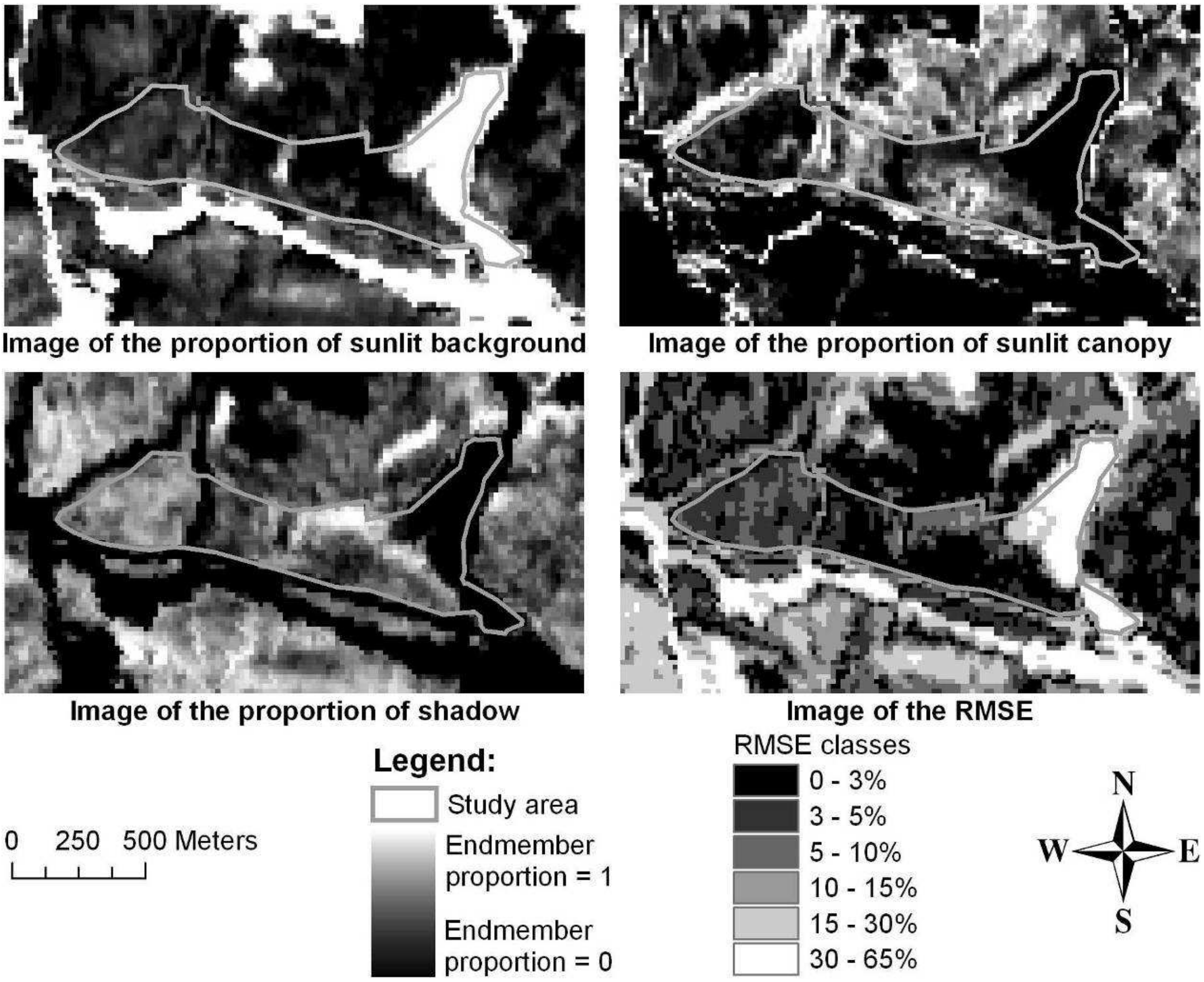

Figure 17: Output of the spectral unmixing for the A9 CHRIS image:
the three proportions images and the image of the root mean square error.

4.1.3.2 Sunlit background proportion and RMSE images for the other viewing angles

Figure 18 presents the sunlit background proportion images for the AC, AA, AB and AD viewing angles, since the model inversion requires only those. For each angle, the corresponding RMSE image is also shown to give an idea of the quality of the spectral unmixing.

AC spectral unmixing results

The high proportion of sunlit background in the Western part of the AC image is caused by cloud contamination. The sunlit background proportion of the non cloudy part of the forest is null. The analysis of the unmixing results shows that the entire reflectance is attributed to the shadow endmember. This is due to the large zenith angle in the forward scattering direction of the CHRIS AC image: the sensor then mainly sees shadowed canopy.

In addition to the null K_g, the RMSE is large: 5 to 30% of the pixel reflectance. It was therefore decided to discard the AC angle in the following of the study.

AA spectral unmixing results

The AA image of K_g contains many null pixels, especially in the Eastern part of the study area forest. The pixels with a non null K_g can be found in the Western part of the study area, where the forest is less dense. The high number of pixels with a null K_g can be explained, as for the AC image, by the forward direction of the AA viewing. The RMSE of most pixels was lower than 10%. The exceptions are the meadow and the denser forest stand.

AB spectral unmixing results

The proportions of sunlit background in the AB image were well related to the forest density: low K_g in dense stands and higher K_g in less dense stands. The RMSE for the AB image was lower than 10% for all the pixels in the study area forest. However, the higher values of the RMSE are located in the Western part of the image. In the Eastern part of the forest, the RMSE was lower than 5%.

AD spectral unmixing results

One will first notice the oblique line of pixels having a null K_g and a high RMSE. This is probably due to sensor malfunctioning. It was not visible in the CHRIS AD image itself but appeared during the image processing. Since this artefact was not present in the forest of the study area it had no consequence on the results for this zone.

The AD image of K_g showed the same pattern as the AB one: low K_g in dense stands and higher K_g in less dense stands. However, the K_g is usually lower than in the AB image. This can be explained by the higher zenith angle of AD: the sensor records more canopy and less background. The RMSE in the forested part of the study area is lower than 10%. It seems that the unmixing performed better in the Eastern part where some pixels had a RMSE lower than 5%.

Summary of the spectral unmixing results

The spectral unmixing yielded the best results for the A9, AB and AD viewing angles (lowest RMSE). The patterns of the sunlit background proportion follow the density of the forest in the real world. In addition, the results are better for the Eastern part of the forest of the study area.

The AC viewing angle was discarded for the following of the study.

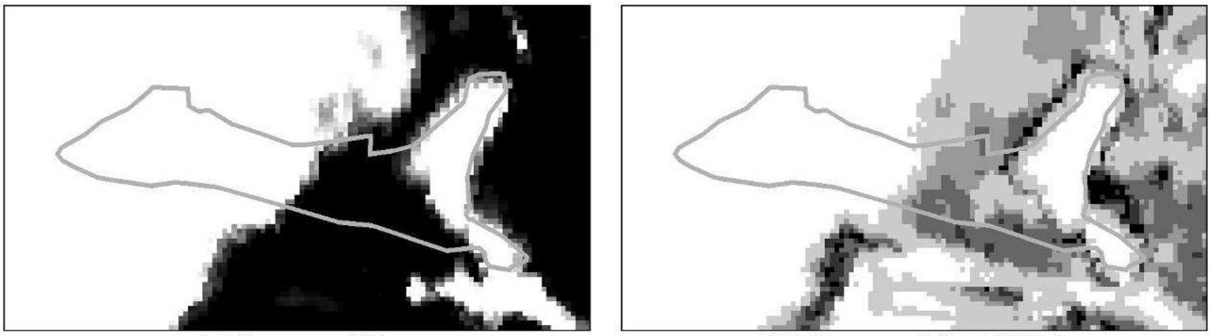

AC image of Kg

AC image of the RMSE

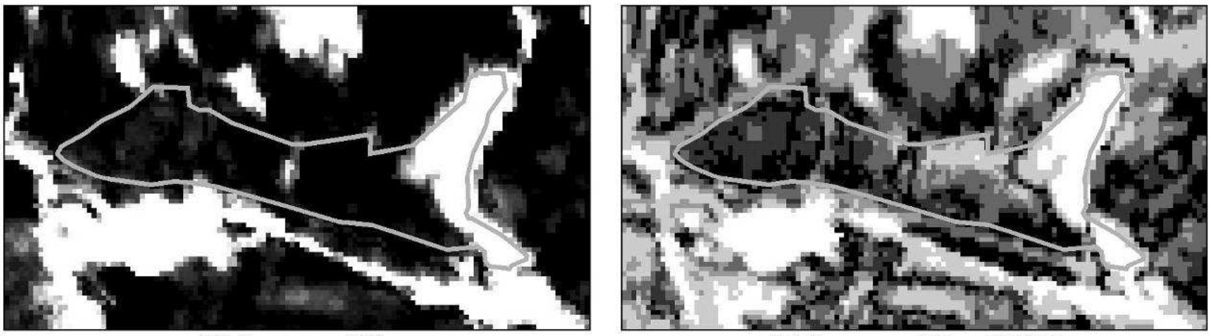

AA image of Kg

AA image of the RMSE

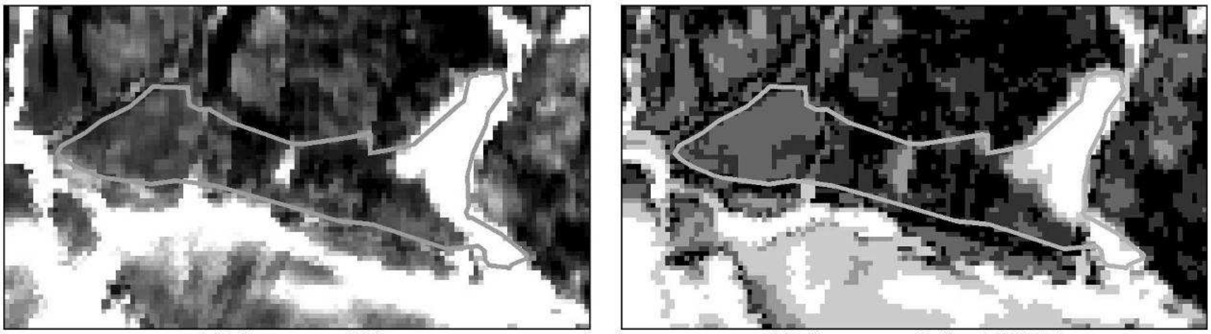

AB image of Kg

AB image of the RMSE

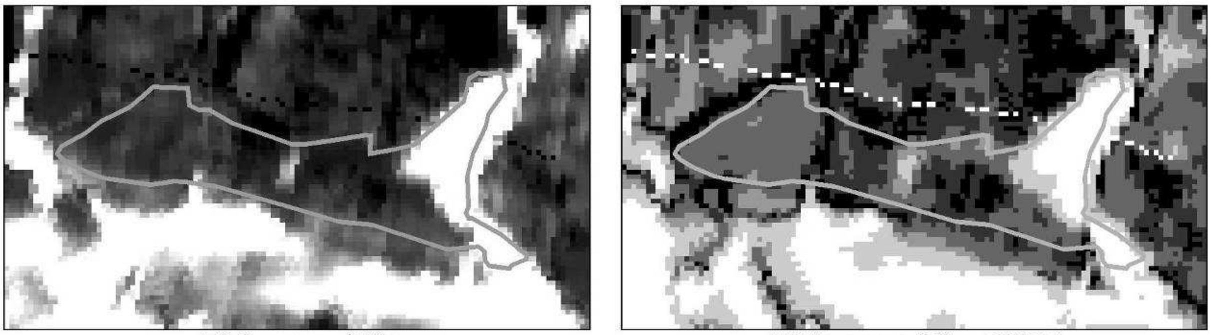

AD image of Kg

AD image of the RMSE

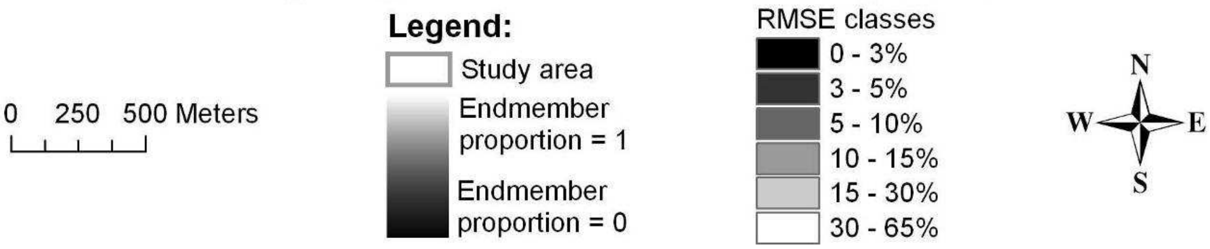

Figure 18: Images of the proportion of the sunlit background and the image of the root mean square error for the AC, AA, AB and AD viewing angles.

4.2 The reference images of canopy cover and crown diameter

As shown in Figure 19, the reference data covers only the Eastern part of the forest of the study area. Therefore, only this part was used later on for the analysis of the results. The canopy cover varied between 0 and 63%, the higher values corresponding to the dense stands. The crown diameter varied between 1.6 and 6.2 meters. However, most pixels had a mean crown diameter comprised between 2 and 4 meters.

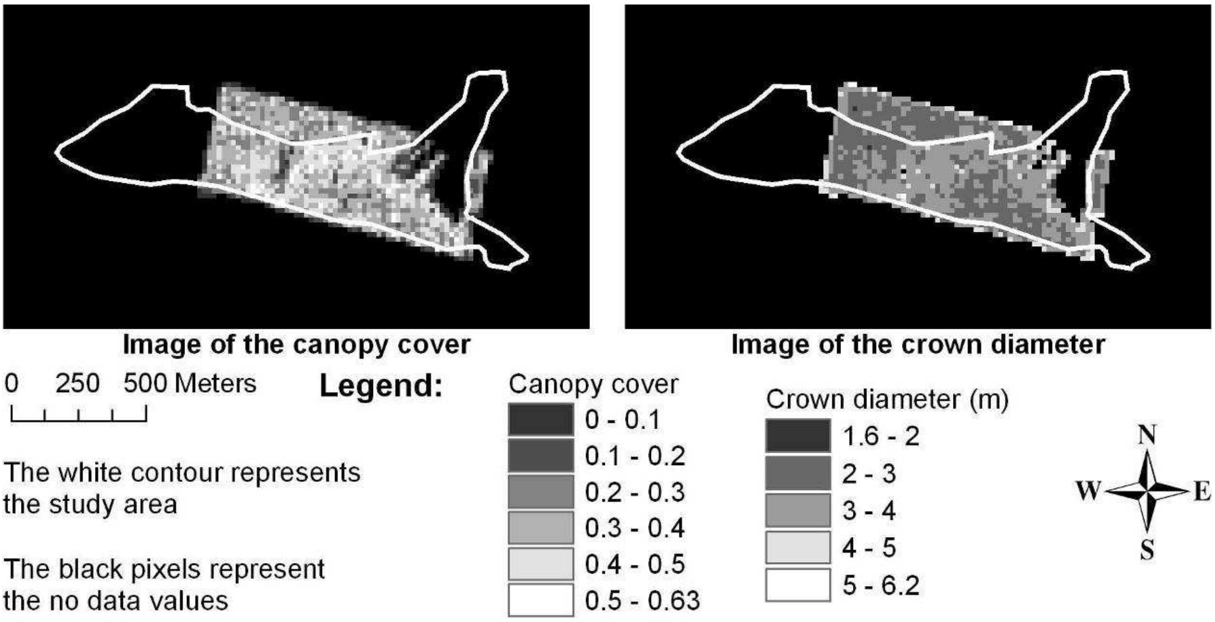
Image of the canopy cover

Image of the crown diameter

Figure 19: Reference images of canopy cover and crown diameter.

4.3 Final results

4.3.1 Number of usable pixels depending on the number of viewing angles considered

When examining the five output images of the model inversion, it appeared that many pixels did not retrieve valid results for all angles. In addition, the pixels which did not have a reference values and those located outside the study area were also discarded. Thus, a number of pixels could not be used for the analysis of the results. The number of usable pixels depended on the number of viewing angles considered, as shown in Table 7.

Table 7: Number of usable pixels depending on the number of viewing angles considered.

	Number of usable pixels	
Viewing angles used	**Canopy cover**	**Crown diameter**
AC AA A9 AB AD	40	49
AA A9 AB AD	154	160
A9 AB AD	425	430

The spreading of the 160 usable pixels when taking the AA viewing angle into account did not enable the drawing of a sufficient number of validation samples. The AA viewing angle was thus discarded. So finally, only the A9, AB and AD viewing angles were used for the analysis of the results.

Figure 20 shows the images of the usable pixels when using the A9, AB and AD viewing angles for both canopy cover and crown diameter analysis. The usable pixels were located in the Eastern part of the forest of the study area. Note that they are preferentially located in the low density stands.

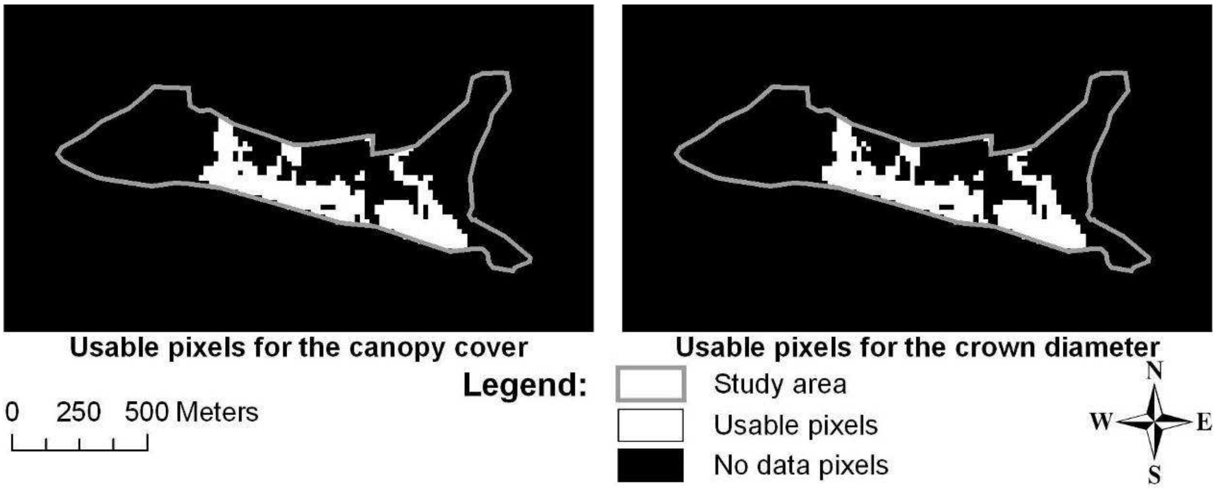
Usable pixels for the canopy cover

Usable pixels for the crown diameter

Figure 20: Images of the usable pixels when using the A9, AB and AD viewing angles for the analysis of the canopy cover and crown diameter results.

4.3.2 Canopy cover results

4.3.2.1 Using individual viewing angles

The output images of the model inversion for the canopy cover are shown in Figure 21. Due to the thresholds applied during the inversion, all the pixels resulted in a value between 0 and 1. However, one can notice that the [0,1] interval is not entirely covered for the AB and AD viewing angles: the maximum canopy cover decreases with the increasing zenith angle (from A9 to AB to AD).

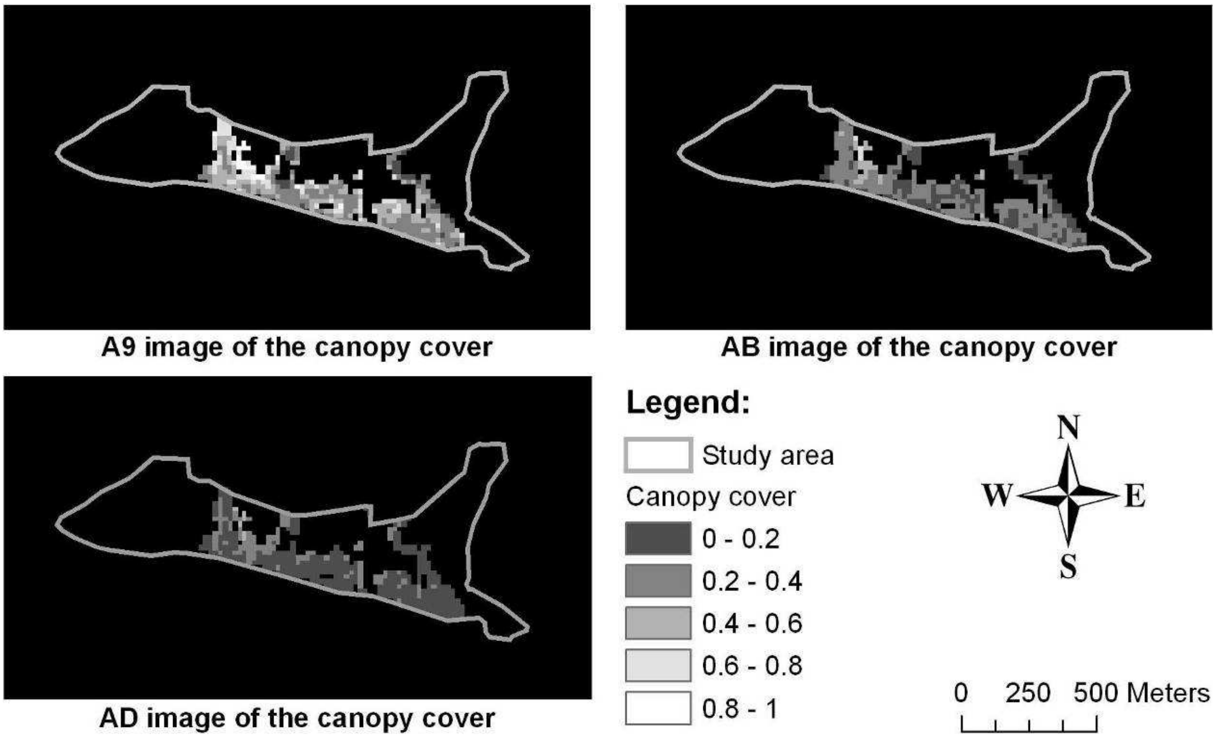
A9 image of the canopy cover

AB image of the canopy cover

AD image of the canopy cover

Figure 21: Output images of the model inversion for the canopy cover for the A9, AB and AD viewing angles.

The three graphs in Figure 22 show the estimated canopy cover for the A9, AB and AD viewing angles against the reference canopy cover value for each of the 79 validation samples. Those graphs confirm the tendency observed on the images of the estimate to decrease with the zenith angle: the maximum canopy cover is about 0.83 for the A9 estimate, 0.55 for the AB estimate and 0.39 for the AD estimate. Not only the maximum of the estimate decreases, but the whole cloud of points lowers when the zenith angle increases. The cloud of points for the A9 angle is above the y = x dotted line, and below it for the AB and AD angles. This means that the canopy cover was overestimated with the A9 angle and underestimated with the AB and AD angles. In addition, the vertical scattering of the points also decreases with increasing zenith angle.

In the ideal situation where the inputs would be perfectly accurate and where the model inversion would yield perfect results, the estimates for the 3 angles would be equal to the reference value and the correlation between the estimates for the 3 angles and the reference data would have an R-square of 1. As shown in Figure 22, this is not the case here. The R-squares values are low (0.13, 0.08 and 0.01 for the A9, AB and AD angles respectively) which indicates weak relationships. These values let one think that the estimates of the A9 angles are best. This is confirmed by the fact that A9 provides the best estimates for 45 of the 79 validation samples, against 29 and 5 for the AB and AD angles respectively. All these indications show that the quality of the estimate decreases from A9 to AB and to AD, i.e. when the viewing zenith angle increases.

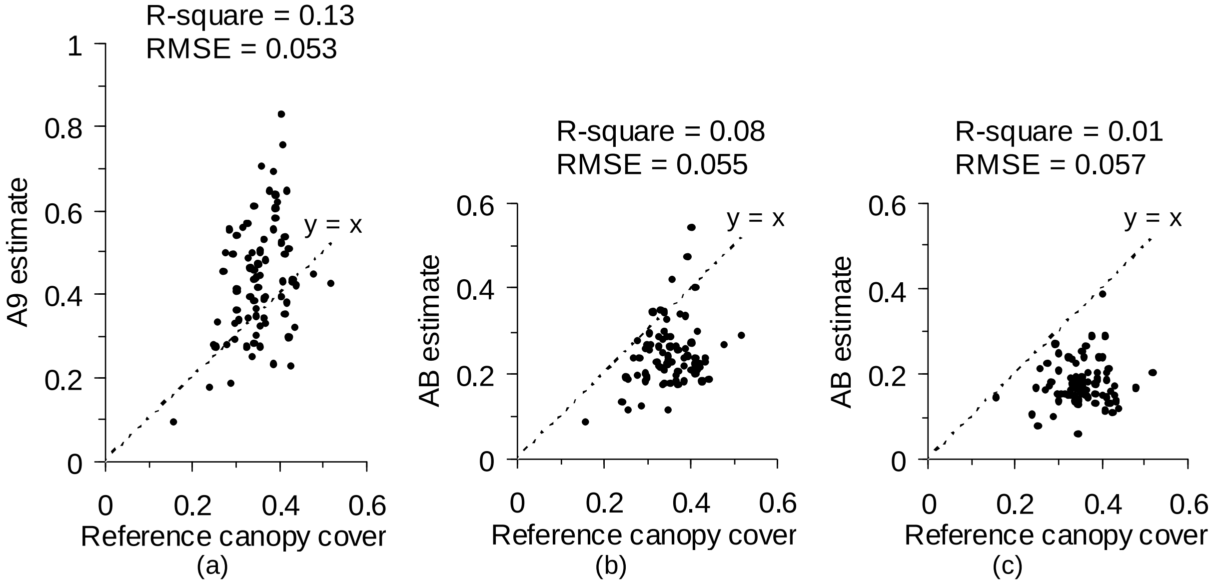

Figure 22: Comparison between the model outputs and the reference data for the canopy cover for the A9 (a), AB (b) and AD (c) viewing angles (79 validation samples).

The rather high R-squares values presented in Table 8 show the rather strong correlations between the estimates for the different angles and prove the good coherence of the outputs of the model inversion for the three angles.

Table 8: Correlation matrix of the canopy cover estimates for the A9, AB and AD viewing angles (79 validation samples).

	A9	**AB**	**AD**
A9	1.00	0.61	0.39
AB	0.61	1.00	0.54
AD	0.39	0.54	1.00

4.3.2.2 Combining the angles

Since both the AB and AD angles underestimated the canopy cover, the interesting angle combinations to try were: the mean of the 3 angles: mean(A9,AB,AD), the mean of A9 and AB: mean(A9,AB), the mean of A9 and AD: mean(A9,AD) and the linear combination of the 3 angles.

The scatter plots of mean(A9,AB,AD), mean(A9,AB) and mean(A9,AD) against the reference canopy cover are presented in Figure 23, together with the R-square and the RMSE of the linear regression. In the mean(A9,AB,AD) and mean(A9,AD) plots, most of the points are below the y = x line, showing that those two variables underestimated the canopy cover. The cloud of points in the mean(A9,AB) plot seems more evenly distributed. However, its R-square is low, like for the other 2 combinations. The means of the estimates also have a weak correlation to the canopy cover reference data.

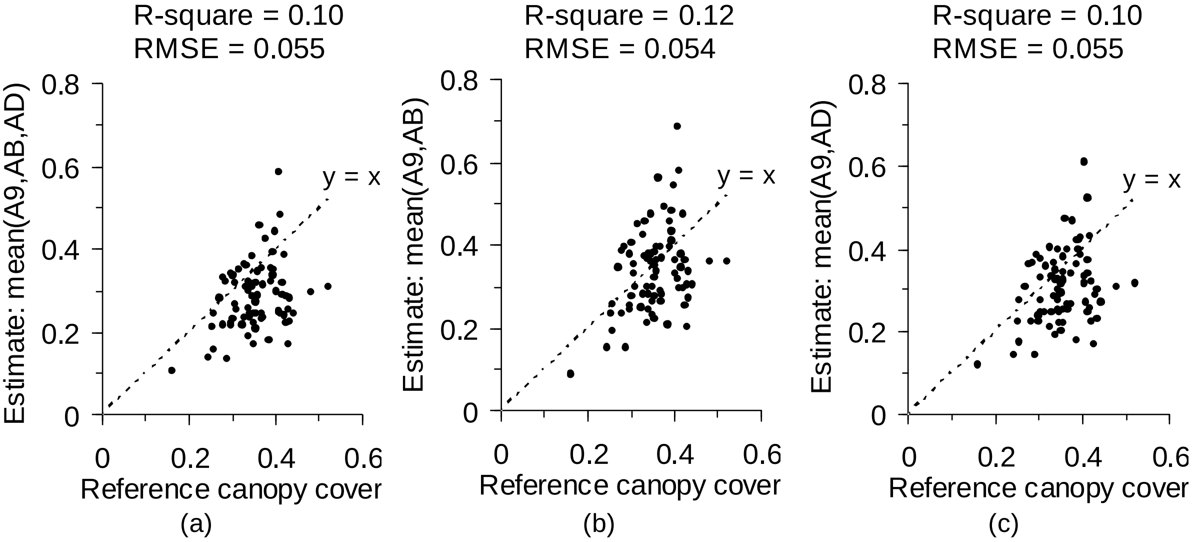

Figure 23: Comparison between mean(A9,AB,AD) (a), mean(A9,AB) (b), mean(A9,AD) (c) and the reference canopy cover (79 validation samples).

The three cases presented above are particular cases of a multiple linear regression with no constant and where the regression coefficients are either 1 or 0. A multiple linear regression was then performed to see if other regression coefficients for the A9, AB estimation and AD estimates and the addition of a constant in the regression equation could explain the dependent variable “reference canopy cover”.

The graph in Figure 24 shows that the canopy cover was underestimated by the linear combination. The R-square and adjusted R-square are low, revealing a weak correlation between the linear combination estimate and the reference canopy cover.

The regression coefficients for the A9, AB and AB estimates are close to 0, compared to the value of the constant, meaning that most of the variance in the reference data is explained by the constant. This explains the horizontal shape of the cloud of points. In addition, standard errors of the A9, AB and AB coefficients are large compared to their magnitude (Table 9).

Finally, the linear combination of the A9, AB and AB estimates is not a good predictor for the canopy cover.

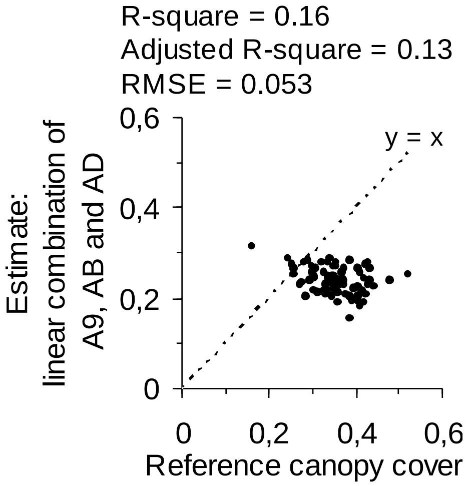

Figure 24: Comparison between the linear combination estimate and the reference canopy cover.

Table 9: Coefficients and their standard errors for the multiple linear regression of the reference canopy cover over the A9, AB and AD estimates.

	A9	AB	AD	Constant
Regression coefficient	-0,29	0,12	0,17	0,31
Standard error of the coefficient	0,18	0,15	0,07	0,02

4.3.2.3 Comparison of the estimates

Table 10 recapitulates the R-squares and the RMSE obtained for the tested estimates for the canopy cover. It is not possible to discriminate the estimates based on their RMSE, since they all have similar values. The estimates combining several viewing angles have (adjusted) R-squares varying between 0.10 and 0.13. They perform better than the AB and AD angles alone, but worse than the A9 angle, except for the linear combination. With R-squares values of 0.13 and RMSE values of 0.053 – 0.054, the A9 angle and the linear combination provide the best estimates. However, the linear combination is more complicated than the simple mono-angular A9 estimate for an equivalent performance. And, as seen in the previous paragraph, the linear combination explains most of the variance of the reference canopy cover by a constant, which is not very realistic. Therefore, the A9 estimate can be considered as the best estimate of the canopy cover.

Table 10: Comparative table of the R-squares and RMSE obtained with the different mono or multi-angular estimates for the canopy cover.

Estimate	**R-square**	**RMSE**
A9 estimate	0.13	0.054
AB estimate	0.08	0.055
AD estimate	0.01	0.057
mean(A9,AB,AD)	0.10	0.055
mean(A9,AB)	0.12	0.054
mean(A9,AD)	0.10	0.055
linear combination	0.16	0.053
Adjusted R-square of the multiple linear combination	0.13	

4.3.3 Crown diameter results

4.3.3.1 Using individual viewing angles

The output images of the crown diameter show that the estimate has a tendency to decrease when the viewing zenith angle increases (Figure 25). Due to the applied thresholds, all the pixels have a value between 0 and 14. However, the maximum crown diameter found in the tree data was 6.80 meters, so one can see that the crown diameter was over estimated for many pixels. On the other hand, the order of magnitude of the estimates is correct.

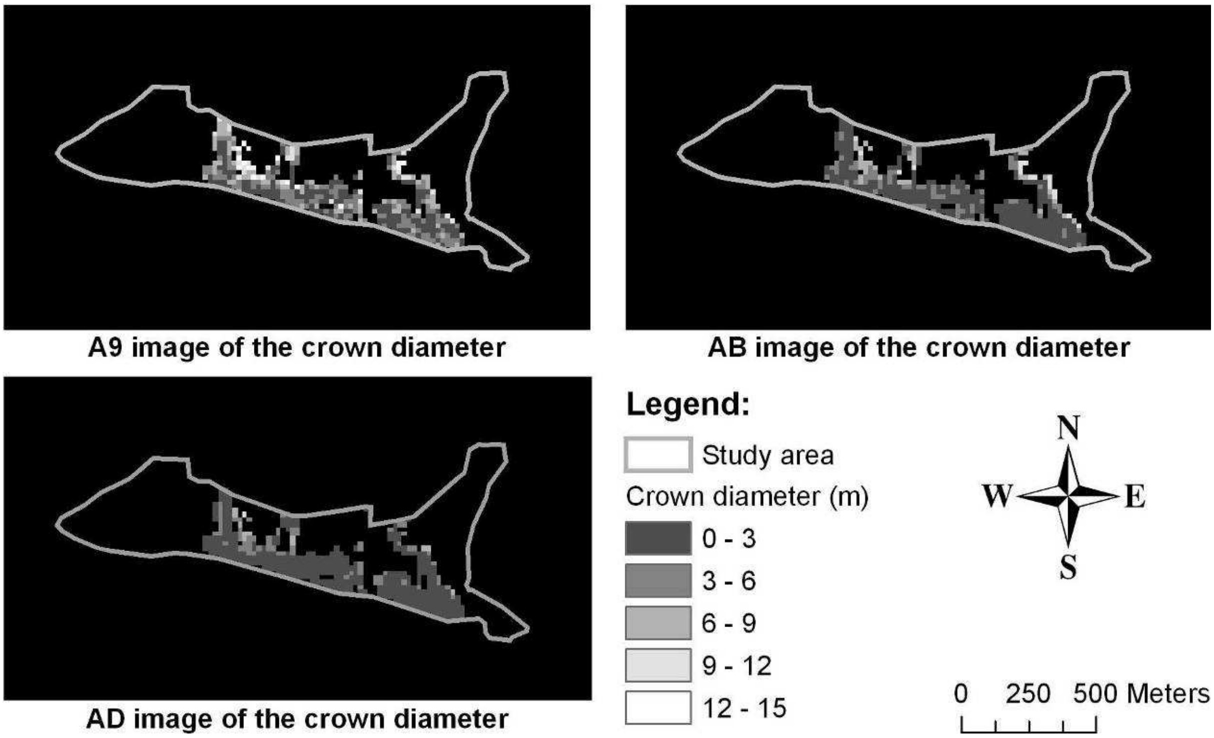
A9 image of the crown diameter

AB image of the crown diameter

AD image of the crown diameter

Figure 25: Output images of the model inversion for the crown diameter for the A9, AB and AD viewing angles.

The graphs in Figure 26 confirm the tendency of the estimate to decrease with the zenith angle observed on the images: the maximum crown diameter is about 12.2 for the A9 estimate, 7.6 for the AB estimate and 6.1 for the AD estimate. Not only the maximum of the estimate decreases, but the whole cloud of points lowers when the zenith angle increases. The first graph shows that the crown diameter was overestimated for the A9 angle, while the second and third graphs show that the crown diameter was underestimated for the AB and AD angles. In addition, the vertical scattering of the points also decreased when the zenith angle increases. One can also note that the 3 estimates present a higher variability (values between 1 and 13 for the A9 estimate) than the reference data computed from the LiDAR estimate of crown diameter (values between 2 and 4). The high variability of the CHRIS estimates corresponds more to the crown diameter variability observed on the field, which suggest that the CHRIS estimates are more realistic.

The estimates of the crown diameter present a weak correlation with the reference data: Figure 26 shows R-squares of 0.01, 0.05 and 0.01 for the A9, AB and AD estimates respectively. The correlations with the reference crown diameter were very weak. It seems that the estimates of the AB angle are better. However, they provide the best estimate for the crown diameter only 22 times out of the total 79 validation samples, against 39 times for the A9 angle and 18 for the AD angle.

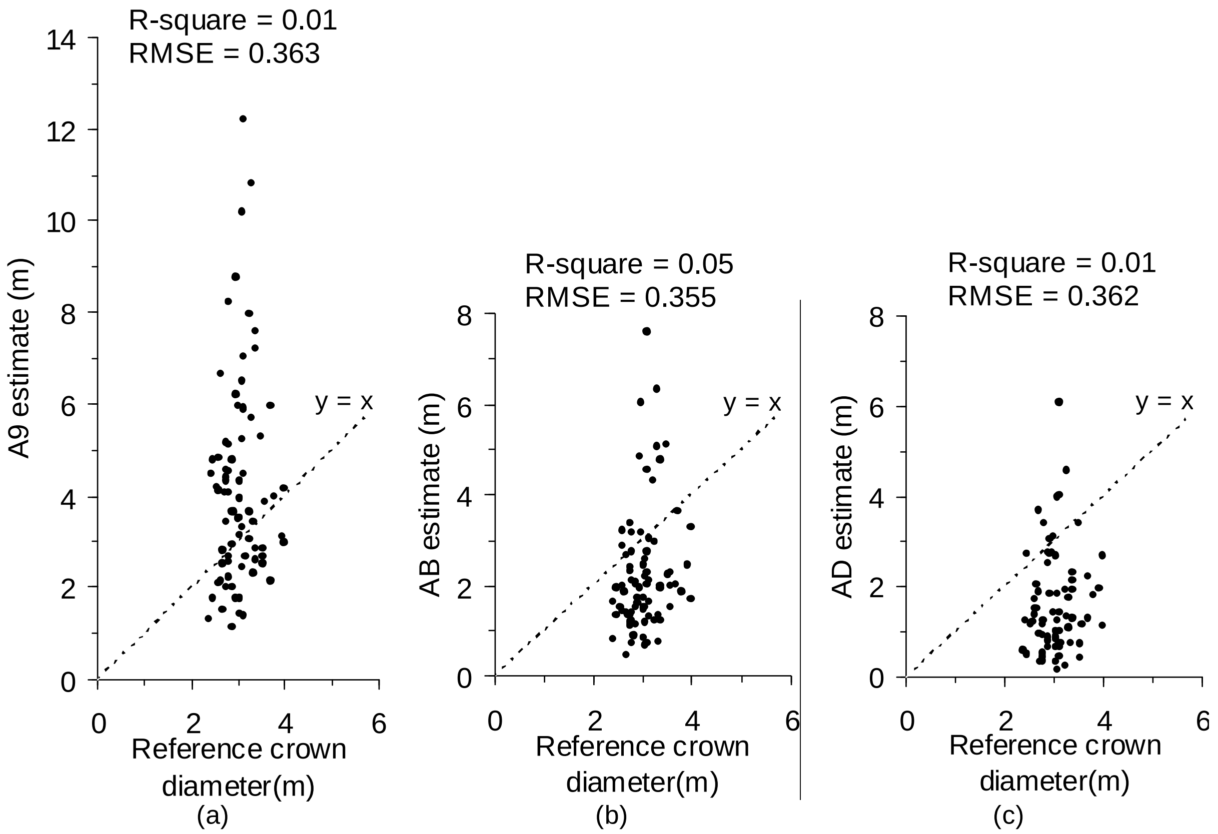

Figure 26: Comparison between the model outputs and the reference data for the crown diameter for the A9 (a), AB (b) and AD (c) viewing angles (79 validation samples).

Table 11 presents the R-squares values of the correlations between the estimates for the different angles. The rather high R-squares values show the quite strong correlations between the estimates for the different angles and indicate a rather good coherence of the outputs of the model inversion between the three angles.

Table 11: Correlation matrix of the crown diameter estimates for the A9, AB and AD viewing angles (79 validation samples).

	A9	**AB**	**AD**
A9	1.00	0.49	0.27
AB	0.49	1.00	0.36
AD	0.27	0.36	1.00

4.3.3.2 Combining the angles

Since both the AB and AD angles underestimated the crown diameter, the interesting angle combinations to try were: the mean of the 3 angles: mean(A9,AB,AD), the mean of A9 and AB: mean(A9,AB), the mean of A9 and AD: mean(A9,AD) and the linear combination of the 3 angles.

The scatter plots of mean(A9,AB,AD), mean(A9,AB) and mean(A9,AD) against the reference crown diameter, the R-square and the RMSE of the linear regression are presented in Figure

27. In the three graphs, most of the points are below the y = x line, indicating that the three variables underestimated the crown diameter. The three R-square is low, indicating that the three tested means have a weak correlation with the crown diameter reference data.

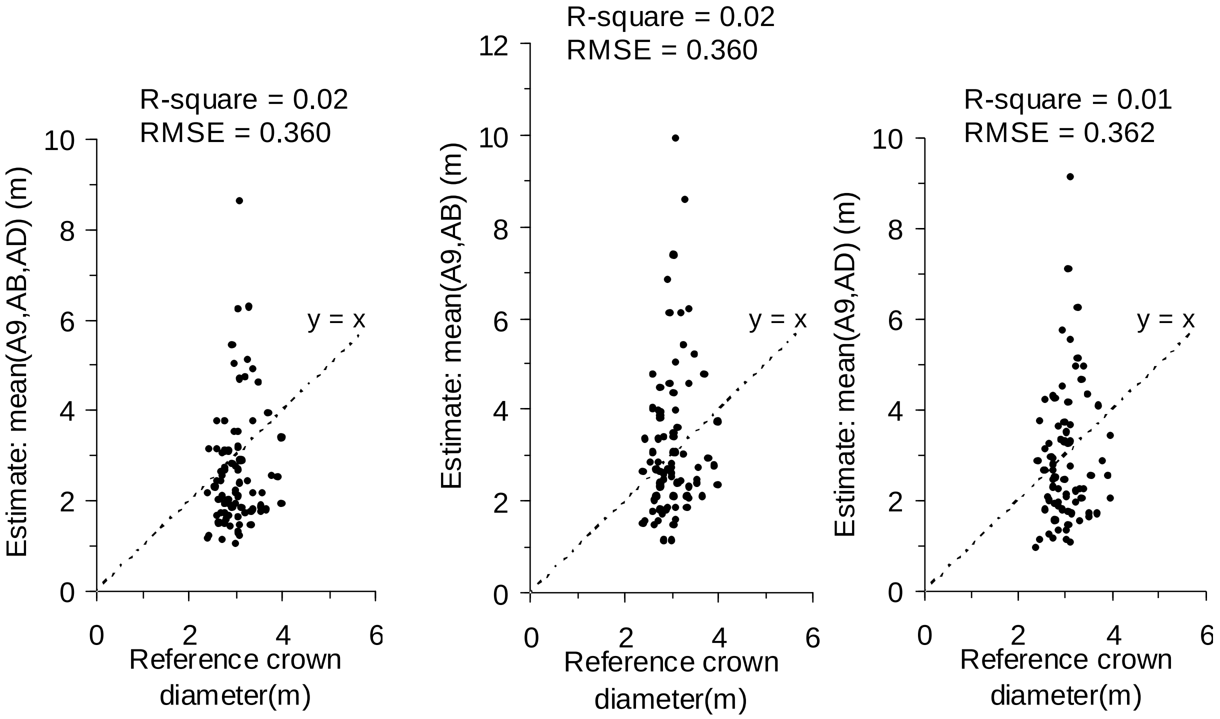

Figure 27: Comparison between mean(A9,AB,AD) (a), mean(A9,AB) (b), mean(A9,AD) (c) and the reference crown diameter (79 validation samples).

Similar to the canopy cover, a multiple linear regression was performed to verify if another combination of the A9, AB and AD estimates could explain the dependent variable “reference crown diameter”. The R-square and adjusted R-square of the correlation between the linear combination estimate and the reference crown cover were low (Figure 28), which indicated a weak correlation between the linear combination estimate and the reference canopy cover. In addition, the graph shows that the points representing the estimated value against the reference value are grouped in a cloud. The cloud has a horizontal shape and is centred on the y = x line. This implies that the low crown diameters were overestimated and the higher values were underestimated. The horizontal shape of the cloud of points can be explained by the high value of the coefficient of constant (Table 12). Moreover, it also has the smaller standard error, meaning that the constant has the most significant regression coefficient.

Finally, the linear combination of the A9, AB and AB estimates was not a good predictor for the crown diameter.

Table 12: Coefficients and their standard errors for the multiple linear regression of the reference crown diameter over the A9, AB and AD estimates.

	A9	AB	AD	Constant
Regression coefficient	-0,002	0,08	-0,02	2,94
Standard error of the coefficient	0,05	0,05	0,03	0,09

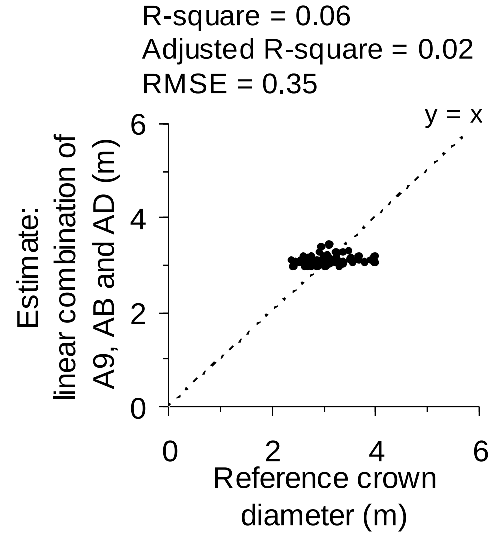

Figure 28: Comparison between the linear combination estimate and the reference crown diameter.

4.3.3.3 Comparison of the estimates

Table 13 shows that the RMSE values all have similar values. It is therefore not possible to discriminate the estimates based of their RMSE. The estimates combining several viewing angles have (adjusted) R-squares of 0.01 or 0.02. They perform as good as or better than the A9 and AD estimates, but worse than the AB estimate. With an R-square value of 0.05, the latter seems to be the best estimate. However, as seen earlier (paragraph 4.3.2.1), it provided the best estimate for the crown diameter only 22 times out of 79, against 39 times for the A9 angle and 18 for the AD angle. It is therefore impossible to designate a best estimate of the crown diameter.

Table 13: Comparative table of the R-squares and RMSE obtained with the different mono or multi-angular estimates for the crown diameter.

Estimate	**R-square**	**RMSE**
A9 estimate	0.01	0.363
AB estimate	0.05	0.356
AD estimate	0.01	0.362
mean(A9,AB,AD)	0.02	0.360
mean(A9,AB)	0.02	0.360
mean(A9,AD)	0.01	0.362
linear combination	0.06	0.354
Adjusted R-square of the multiple linear combination	0.02	

4.3.4 Qualitative analysis of the final results

Even though the correlation between the obtained estimates and the reference data for both canopy cover and crown diameter were weak, some interpretations can be derived. First of all, the model outputs fitted the reasonable threshold set for the inversion for an important number of pixels in the forest of the study area. Then, the three mono-angular estimates were rather highly correlated, showing the good coherence of the outputs. And last, the crown diameter results were coherent with the canopy cover results. Since the model sets the tree density for each pixel (following the Poisson law), a high canopy cover implies a big crown diameter and the other way around. The observations of the estimates showed that both the crown diameter and the canopy cover were overestimated for the A9 angle and underestimated for the AB and AD angles.

4.3.5 Comparison between the quality of the canopy cover and crown diameter results

To facilitate the comparison between the canopy cover and crown diameter results, the R-squares values already presented in Table 10 and Table 13 were gathered in Table 14. The latter shows that, excepting the AD estimate, the (adjusted) R-squares vary between 0.08 and 0.13 for the canopy cover and between 0.01 and 0.05 for the crown diameter. This indicates that the estimates obtained for the canopy cover are better than the estimates obtained for the crown diameter.

Table 14: Comparative table of the R-squares and RMSE obtained with the different mono or multi-angular estimates for canopy cover and crown diameter.

Estimate	**Canopy cover**	**Crown diameter**
A9	0.13	0.01
AB	0.08	0.05
AD	0.01	0.01
mean(A9,AB,AD)	0.10	0.02
mean(A9,AB)	0.12	0.02
mean(A9,AD)	0.10	0.01
linear combination	0.16	0.06
Adjusted R-square of the multiple linear regression	0.13	0.02

4.4 Implications of the mono-angular canopy cover results on the quality of the sunlit background proportion images

Since the sunlit background proportion is the only changing parameter between the model inversions for the three angles, it can be related to the mono-angular canopy cover results. Using equations (9) and (10), the canopy cover can be expressed as:

$$\mathrm{CC} = 1 - \left(\mathrm{K_g}\right)^{\mathrm{a}} \tag{20}$$

Where a is given by:

$$\mathrm{a} = \frac{\pi}{\left(\sec\theta_{\mathrm{i}} + \sec\theta_{\mathrm{v}}\right) \cdot \left(\pi - t + \cos t \sin t\right)} \tag{21}$$

Equation (20) shows that the canopy cover and the sunlit background proportion are negatively related by a “power” relationship. This is illustrated for the three angles in the graphs of Figure 29.

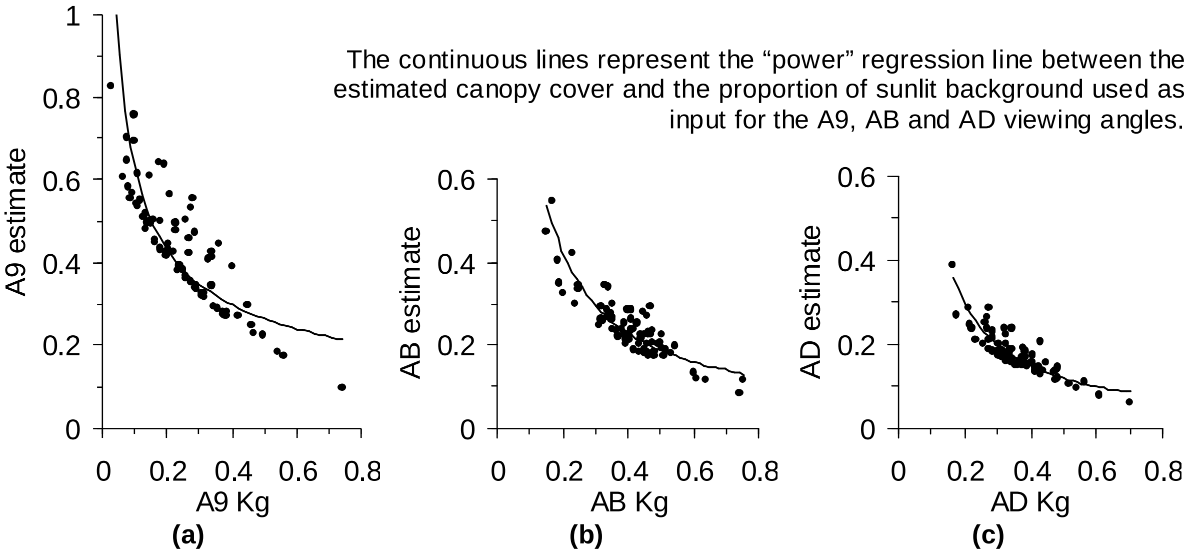

The continuous lines represent the “power” regression line between the estimated canopy cover and the proportion of sunlit background used as input for the A9, AB and AD viewing angles.

(a) **(b)** **(c)**

Figure 29: Relationships between the estimation of the canopy cover and the proportions of sunlit background for the A9 (a), AB (b) and AD (c) viewing angles (79 validation samples).

Since the canopy cover was overestimated with the A9 angle, it can then be inferred that the sunlit background proportion was underestimated for the A9 angle. Similarly, one can conclude that the sunlit background proportion was overestimated for the AB and AD angles.

5 Discussion

This section first discusses why the quality of the estimates is so poor (paragraph 5.1). It then proposes some reasons which could explain why the sunlit background proportion was underestimated for the A9 viewing angle (paragraph 5.2) and explores the effects of the zenith viewing angle on the results (paragraph 5.3). Paragraph 5.4 gives some clues to explain why the results are better for the canopy cover than for the crown diameter. Finally, paragraph 5.5 discusses the results in the framework of the evaluation of the quality of the protection provided by the forest.

5.1 Poor quality of the estimates

There are many available examples of studies which successfully inverted the Li-Strahler model to estimate a number of parameter. Among them, Woodcock et al. (1997) estimated the treeness parameter m, achieving good correlation with the field measured m: the R-squares varied between 0.46 and 0.93, depending on the forest tree species. Franklin and Strahler (1988) and Gemmell (1998) both found high R-squares values for the correlation between the model inversion output for the canopy cover and the ground measurements: respectively 0.62 to 0.78 and 0.76. Similarly, Zeng et al. (2007) found R-squares of 0.61 and 0.39 for the correlation between the estimated and measured canopy closure and crown diameter.

The inversion of the Li-Strahler model was successful in all the above mentioned case, so why are the R-squares values obtained for canopy cover and crown diameter in this study so low? Some possible explanations are explored in this paragraph.

5.1.1 Lack of ground truth data

Even if the methodology was assumed to be perfect, with no assumption, this study would probably end up with poor results. Since the error propagates through the methodological steps, if one of the intermediary results is not accurate, the final results will also be affected by errors. Because of the lack of ground truth data to check the outputs of each step, the errors are only noticed on the final results. In addition, the quality of the reference data used to analyse the final results is questionable.

5.1.1.1 Bias of the classification of the ROSIS image

The classification of the ROSIS image was validated by the confusion matrix presented in Appendix 8.9. Both the overall accuracy and the Kappa coefficient were high (92.6% and 0.89), indicating the good quality of the classification. However, this confusion matrix was not built using ground truth data, but using ROIs visually selected on the original ROSIS image (paragraph 3.5.1). Since it was important to be sure of the component in the pixels used both to obtain the classification and to evaluate it, the pixels used for the “ground truth” ROIs were chosen with the same visual method as to select the pixels for the training areas. So, in the end, the same type of pixels, located in the same areas of the image where it is possible to distinguish between sunlit canopy and sunlit background were used. It is obvious that the confusion matrix would show a high overall accuracy and a good Kappa coefficient.

5.1.1.2 Uncertainty of the endmembers signatures

It would also have been interesting to compare the endmembers signatures obtained by linear spatial unmixing to signatures measured in situ. However, the field work focussed on sunlit endmembers and no field spectrum was available for the shadow endmember. Also the field spectra of the sunlit canopy and the sunlit background did not take the bark into account. Since the bark represent a non negligible proportion of both endmembers (Figure 31 page 66 and Figure 32 page 68), it was not appropriate to use the field spectra to check the outputs of the linear spatial unmixing. In addition, the field campaign did not take place during the CHRIS overflight (June 27th 2004), but on August 14th 2002, so the phenological state of the vegetation was different and probably influenced the signature of the vegetation.

5.1.1.3 Validating the image of the proportion of sunlit background

The quality of the images of the proportion of sunlit background was roughly assessed using the only available indicator: the RMSE of the spectral unmixing. However, Peddle et al. (1999) used nadir photographs taken from a helicopter flying at a height of 100m over the forest to validate the endmembers proportions. No such photographs were available for the study area.

5.1.1.4 Uncertainty of the LiDAR-derived data

As one can see in Figure 30, the adjusted R-square of the correlation between the LiDAR-estimated and the field-measured crown diameter is rather low (0.20). In addition, the graph shows that the majority points are below the y = x line, which mean that the LiDAR tends to overestimate the crown diameter. This is be because the LiDAR sees clumped tree crowns as one big crown and cannot measure the individual diameter of clumped trees. Morsdorf et al. (2004) thus computed an artificial diameter for each tree group which seems to have overestimated the field crown diameter.

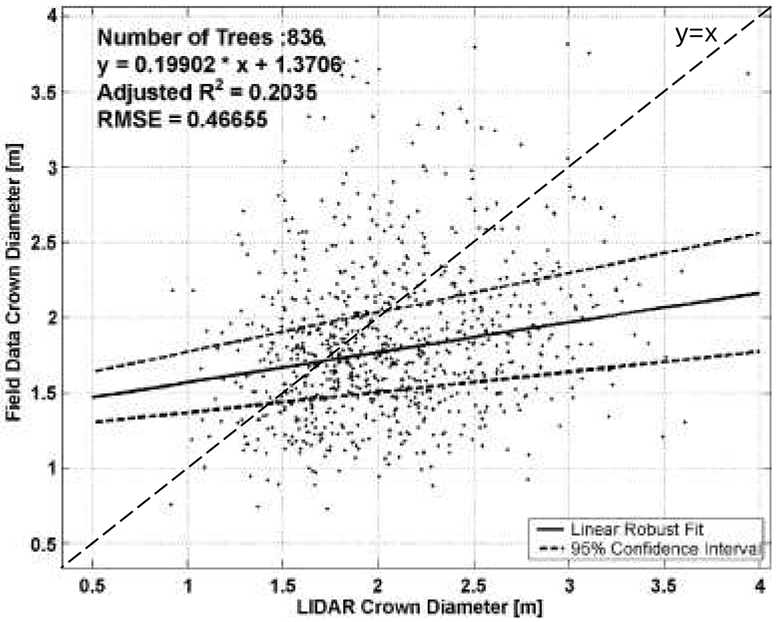

Figure 30: Correlation between the LiDAR-derived and the field-measured crown diameter (Source: Morsdorf et al., 2004).

First of all, the LiDAR-derived crown diameter data was used to calculate the ω coefficient (Table 3 page 26), which is one of the model inputs. The value used to invert the model is probably not correct and therefore probably induced some errors in the model outputs.

However, the model is not very sensitive to variance in the tree shape and size parameters, including the ω parameter (Franklin and Strahler, 1988).

The LiDAR-derived data was also used to derive the reference images because the field data available for the LWF1, LWF2, STA1 and STA2 plots could not be used to validate the data. The plots measure 20 x 20 meters which is about the pixel size of the results (18 x 18 meters) and poses the same problem as comparing the results to the reference images on a pixel basis (see paragraph 3.5.2). In addition, when overlaid with the images, the plots partly cover 4 pixels, which makes the comparison to a single pixel impossible. However, seeing the graph in Figure 30 one can doubt the appropriateness of the LiDAR-derived reference maps to validate the final results of the study.

The analysis of the results showed that the A9 estimate overestimated the reference crown diameter. Since the LiDAR tended to overestimate the crown diameter, it can then be inferred that the A9 estimate overestimated the field-measured crown diameter, and more than the LiDAR estimate.

In addition, the fact that the LiDAR overestimated the crown diameter implies that the mean crown diameter per pixel calculated from this data is also overestimated. The mean of the reference crown diameter is 3.18 m which is much higher than the 1.76 m field value reported by Schaepman et al. (2004). However, one would then expect that the use of the LiDAR data would yield an overestimated canopy cover, which is not the case. Indeed, the mean of the reference canopy cover is 31.9% which is underestimated compared the field values reported by Schaepman et al. (2004): 55%, 46%, 77% and 79% for the LWF1, LWF2, STA1 and STA2 plots respectively (see Figure 2 page 22 for the location of the plots).

5.1.2 Methodology assumptions

In addition to the lack of ground data, many assumptions were made at the different steps of the methodology. The emphasis here is on the assumptions that possibly lead to some errors.

5.1.2.1 Spectral mixing equation

The spectral mixing equation shown in equation (13) states that the reflectance of the pixel can be expressed as a linear combination of the endmembers signatures. It assumes that the chosen endmembers cover the scene entirely and that they contribute linearly to the pixel reflectance. The latter assumption is not completely true: Borel and Gerstl (1994) showed that non linear mixing is caused by multiple reflections between endmembers and that it is more important in the Near Infra Red (NIR) part of the spectrum, where the reflectance of the vegetation endmember is high. However, the linear mixing equation was used consistently during the study: the endmembers were derived from the ROSIS image using the linear spatial unmixing and they were used to spectrally unmix the CHRIS images, also linearly.

5.1.2.2 Assumptions for the linear spatial unmixing

The linear spatial unmixing assumes that the classification of the ROSIS image is accurate and uses it to derive the endmembers proportions in the CHRIS A9 pixels to calculate the endmembers signatures according to the CHRIS reflectances.

Beyond the accuracy of the classification, the solar and viewing geometry of the ROSIS and CHRIS A9 images are also involved. Since the endmembers proportions viewed by the sensor depends of the solar and viewing angles, according to the geometric basis of Li-Strahler theory: it had to be assumed that the illumination and viewing conditions of the ROSIS and CHRIS A9 images were similar. However, if the relative zenith angles between the sun and the CHRIS A9 or ROSIS images are comparable (43.2 against 45.3°), there is a difference of more than 30° between the relative azimuth angle between the sun and the CHRIS A9 or ROSIS images (154.2 against 122.9°). So the assumption of similar illumination and viewing condition is not correct.

5.1.2.3 Assumptions for the linear spectral unmixing

To be able to use the signatures calculated for the A9 image to spectrally unmix the other four CHRIS images which have different viewing conditions, the endmembers were assumed to be Lambertian. This assumption was also made by Li and Strahler (1986). However, Abdou et al. (2001) showed that there were important deviations in the HDRF pattern of a concrete tarmac form that of an equivalent Lambertian surface, especially in the forward scatter direction for which the best results of this study were obtained. Looking at vegetation, Grant (1987) reports that leaves are not Lambertian reflectors. Since the endmembers contain mostly leaves, they are probably not Lambertian reflectors either.

In addition, the composition of the components themselves possibly changes with the zenith azimuth angle. For example, the needles of *Pinus Montana* are clumped on the shoots and a large proportion of bark is visible from high viewing zenith angles, as shown in Figure 31. But when the viewing zenith angle decreases, the bark of the trunk and branches is more and more hidden by the shoots. Using the same signatures for the sunlit and shadowed canopy components to spectrally unmix the 5 CHRIS images is then not accurate.

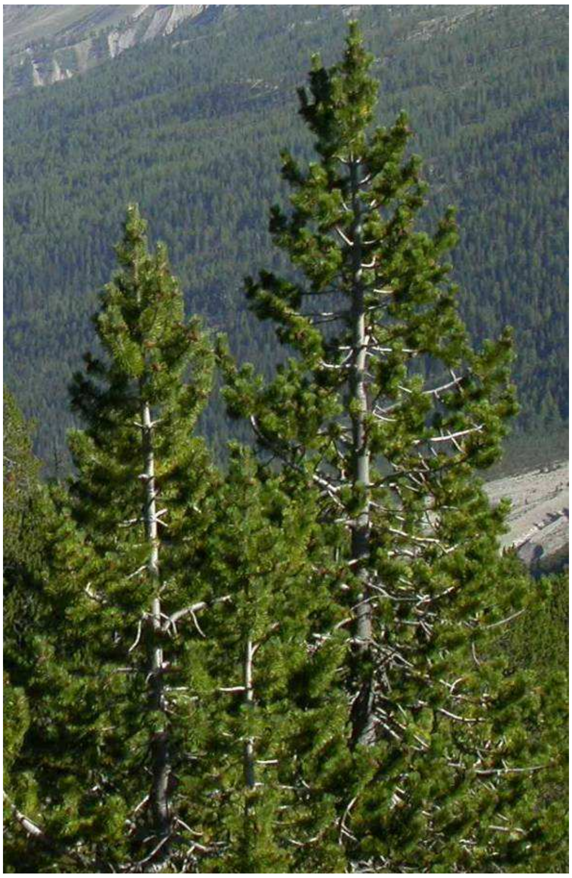

Figure 31: Picture of two crowns of *Pinus Montana* (Source: Koetz B.).

5.1.2.4 Assumptions of the Li-Strahler model

The theory of the Li-Strahler model and its inversion rely on a number of assumptions. They are not all relevant to this study because the model inversion was performed directly on the images of the sunlit background proportion. The spectral unmixing step was not part of the inversion and the related assumption of Lambertian behaviour was discussed in the previous paragraph. For the purpose of this section, only the discussable assumptions are presented here.

The early versions of the model were designed for forests with sparse trees casting their shadows on a contrasting background. The forest of the study area is dense and Li and Strahler (1986) expected the accuracy of the model to decrease with the increasing tree density, so the quality of the results might be not so good. In addition, the background (understory) in the study area consists mainly of various Ericaceae and Sesleria species, but also contains a non negligible amount of bark and small *Pinus Montana* trees. So, the needles and bark elements are not specific to the sunlit canopy signature, but participate to the signature of the background as well.

The model was inverted using an ellipsoid crown shape. But as shown in Figure 31, the top of the trees which are the most visible part of the tree for the sensor have a shape closer to the cone than to the ellipsoid. Rautiainen et al. (2004) observed considerable differences in the HDRF of conifer forests simulated by the Kuusk–Nilson forest reflectance model (2000) when using cone, cylinder, ellipsoid, and cone over cylinder as crown shapes. However, the ellipsoid crown shape was successfully used to invert the model for conifer forests by Peddle et al. (1999) and Zeng et al. (2007).

The use of the Boolean model (paragraph 2.7.2.3) requires assuming that the trees are randomly distributed. But the forest of the study area presents two zones with different densities, so the trees are preferentially located in the dense zone and their distribution might not be considered as random.

Finally, an underlying assumption related to the inversion of the Li-Strahler model is that the BRF and HRDF patterns are similar: the forward model calculates BRF values, whereas HDRF CHRIS data was provided as input for the model inversion. However, this was also the case in the above-mentioned studies, which showed that the inversion of the Li-Strahler model performs well when inputting HDRF instead of BRF data.

5.2 Underestimation of the sunlit background proportion for the A9 viewing angle

The analysis of the results showed that both canopy cover and crown diameter were overestimated for the A9 viewing angle, implying that the sunlit background proportion was underestimated and that the classification of the ROSIS image was not completely accurate.

An explanation for this might be the regeneration of the forest stand present in the understory of the forest (Figure 32). The spectral signature of the small trees is very similar to the signature of the canopy, but they do not belong to the crown layer. So, in case the small trees were sunlit, they participated to the proportion of sunlit canopy when they should have counted as sunlit background, and it could then happen that a ROSIS pixel was classified as sunlit canopy instead of sunlit background. Since the linear spatial unmixing was based on the classification, the errors would have implied the retrieval of incorrect signatures for both sunlit background and sunlit canopy. As a consequence of the error transmission, the proportion of sunlit background would then be under estimated.

Figure 32: Picture of the understory of the forest of the study area (Source: Koetz B.).

5.3 Influence of the zenith angle

The viewing zenith angle influences more the reflectance of vegetation and of conifer forests in particular than the viewing azimuth angle. Deering et al. (1999) who measured approximate BRF values over boreal conifer forests with the PARABOLA instrument found that the extreme values for the BRF were located in the principal plane where only the viewing zenith angle varies. Therefore, the values of the CHRIS reflectances and the subsequent model outputs can be examined according to the zenith angle.

5.3.1 Why AC and AA viewing angles could not be used

The reflectances measured by the CHRIS sensor were low. For the sake of interpretability, the pixel values for all the bands were multiplied by 1000 during the pre-processing. In addition to this, the viewing direction influences the magnitude of the measured reflectance. When the satellite is in the backward direction, it records the sunlit parts of the ground objects whereas when it is situated in the forward direction it mainly records the shadowed side of the objects. This effect is accentuated by the viewing zenith angle: when it increases, the scene becomes brighter (in the backward direction, until the hotspot is reached) or darker (in the forward direction).

As shown in

Figure 3 (page 23), the AC and AA viewing angles are in the forward scatter direction, AC having the highest zenith angle. Therefore, in those two directions, the proportion of shadows is high and the proportion of sunlit background is likely to be low or even null, yielding no data pixels after the model inversion, especially in the AC direction. In addition, the reflectances are very low and it is more difficult to distinguish the components, which makes the RMSE of the spectral unmixing higher.

5.3.2 Decrease of the quality of the canopy cover estimate from A9 to AB to AD viewing angle

As explained in the previous paragraph, the images associated to the AB and AD viewing angles which are in the backward direction are brighter and have higher reflectances. The A9 viewing angle is actually situated in the forward direction, but it is close to nadir and thus does not suffer from low reflectance values.

The main difference between the A9, AB and AD viewing angles that could explain the decreasing quality of the canopy cover estimate is the zenith angle which increases from A9 to AB to AD. This is to be related to the reflectance of the sunlit canopy which depends on the zenith angle because of the visible proportion of bark (paragraph 5.1.2.3).

However, no trend of decreasing estimate quality with the increase of the zenith angle was observed for the crown diameter results. It might be because of their very poor quality that would reflect the reference data too randomly.

5.4 Better results for canopy cover

The canopy cover is directly related to area measures: the area of canopy and the total area viewed from nadir. Areas are easily measurable on remote sensing images. It can therefore be better calculated by the inversion of the geometric model of Li-Strahler.

The measure of the crown diameter, however, relies on the division of the area covered by the canopy by the number of trees. The number of trees per pixel is simulated by the Li-Strahler model following the Poisson law. It is determined based on probabilities and may or may not correspond to the real number of trees in the pixel. The model outputs for the crown diameter are therefore less reliable than for the canopy cover.

The better quality of the canopy cover results compared to the crown diameter results was also observed by Zeng et al. (2007).

5.5 Evaluation of the findings in the framework of the evaluation of the quality of the protection provided by the forest

To evaluate the level of protection provided by a forest against the natural hazards different types of information are needed. The canopy cover and crown diameter on which this study focused are two parameters among the required variables. These two parameters are of interest especially in the framework of the flood and avalanche hazard.

The canopy cover is directly related to the free rainfall proportion (proportion of the rain which falls straight to the ground without striking the canopy = 1 – canopy cover) which is an input of Rutter’s rainfall interception model (1971). However, the knowledge of the amount of intercepted rainfall is not sufficient to evaluate the quality of the protection provided by the forest regarding to the flood hazard. The soil water storage capacity (Sidle et al., 2000) and the rainfall interception of the forest understory should also be taken into account.

The landslide hazard is closely related to rainfall interception: the presence of forest canopy cover improves slope stability (Montgomery et al., 2000; Keim and Skaugset, 2003). Landslide modeling requires additional data about slope, groundwater and root strength (Weimin and Sidle, 1995).

The canopy cover is an input of Hedstrom and Pommeroy’s snowfall interception model (1998). The crown diameter, combined with the canopy cover, enables the retrieval of the canopy gap diameter which is also required to run Hedstrom and Pommeroy’s model. Besides the amount of intercepted snowfall one also needs to know whether the avalanche starting zone is forested (Frey and Thee, 2002).

The canopy cover and crown diameter do not directly participate in evaluating the quality of the protection provided by a forest regarding to the rockfall hazard. An indicator of the latter is the percentage of rocks that pass through the sloping forest. This can be calculated by models that usually require the DEM of the area and the tree density (Dorren, 2003). The tree species should also be taken into account since they do not all have the same mechanical resistance to rockfall (Stokes et al., 2005).

Finally, when evaluating the protection provided by a forest, the forest structural parameters including canopy cover and crown diameter are essential. The tree species, the soil and the understory also play a role in the protection, so the whole forest ecosystem is important. However, the knowledge of all these parameters only enables to evaluate the resistance of the forest to the hazards at a given moment. When talking about protection, the time dimension should also be included. It is important that the forest ecosystem is able to provide a good protection on a long term scale and therefore that the forest has a good elasticity (Brang, 2001). The concepts of resistance and elasticity were defined by Grimm and Wissel (1997): the resistance is the capacity of the forest to stay essentially unchanged despite the hazard impacts and the elasticity is the speed of return to the referential state or dynamics after the hazard disturbance.

Moreover, the size of the forest considered in this study is too small to allow the evaluation of the protection provided by the forest. The area to take into account depends on the hazard: one should use the whole watershed area for the flood, the whole slope for the landslide, the crest area for the avalanche and the slope situated below the escarpment.

6 Conclusion

6.1 Main findings

This study did not successfully retrieve reliable estimates for canopy cover and crown diameter in the studied forest. The R-squares of the correlation between the estimates for the different angles and the reference data were very low (between 0.01 and 0.13). Since the results are not reliable, they cannot be used to evaluate the quality of the protection against the natural hazards provided by the studied forest. Besides, meteorological and soil data as well as additional forest structural parameters are necessary for this purpose. Therefore, using the outcomes of this study, it is not possible to assess the quality of the protection provided by the forest. Even though the results were disappointing, a careful analysis of the results enabled to draw of a number of interesting conclusions.

The backward CHRIS viewing angles (AB and AD) performed better with respect to the retrieval of the canopy cover and crown diameter than the forward viewing angles (AC and AA) which did not enable the retrieval of estimates for a sufficient amount of pixels to be taken into account in the results analysis. Even though the A9 viewing angle is situated somewhat in the backward direction, it performed well.

Regarding the A9, AB and AD viewing angles, it was show that proportion of sunlit background was underestimated for the A9 viewing angle and overestimated for the AB and AD viewing angles. As a consequence, both the canopy cover and the crown diameter were overestimated for the A9 viewing angle and underestimated for the AB and AD viewing angles. However, all the estimated values were in the correct order of magnitude. The estimates obtained by combining the A9, AB and AD estimates did not yield better results than the A9, AB and AD estimates themselves. Despite its high values, the inversion output for theA9 near-nadir viewing angle provided the best estimate of the canopy cover. No best estimate could be distinguished for the crown diameter.

Finally, the analysis of the results showed that the quality of the estimates was better for the canopy cover than for the crown diameter and that the quality of the estimates of the canopy cover decreases when the viewing zenith angle increases. In addition, the A9, AB and AD CHRIS estimates for the crown diameter presented a higher variability than the LiDAR estimates which suggests that they are more realistic.

The poor quality of the results for both the canopy cover and the crown diameter might have been caused by a number of errors that added up and propagated through the methodology. The main possible sources of errors are summarized here.

First, the presence of forest regeneration in the understory might have lead to misclassify some ROSIS sunlit background pixels as sunlit canopy. Then, the assumption that the relative illumination and viewing geometry of the ROSIS and CHRIS images were similar might have caused the spatial unmixing of the CHRIS A9 image to provide incorrect endmembers signatures. In the spectral unmixing step, because of the increasing amount of visible bark with increasing viewing angle, the assumption that the signatures of the sunlit and shadowed canopy do not depend on the viewing angle was probably in correct. For the model inversion, the choice of an ellipsoid crown shape and the use of a random distribution to characterize the repartition of the trees over the scene might be not very well adapted to the studied forest.

Finally, the lack of ground truth data to control the outputs at each step of the methodology facilitated the error propagation during the study. Since they were computed using the poor LiDAR-derived tree crown diameter data, the reference images of canopy cover and crown diameter do not reliably represent the spatial variations of the canopy cover and crown diameter on the field. Therefore, a weak correlation between the inversion outputs and the reference data does not necessarily imply a weak correlation between the inversion outputs and the field measurements.

6.2 Recommendations

Further research should first compare the outputs of the model inversion with field data. The estimates might show better correlation coefficients with the field measurements than with the reference data computed from the LiDAR-derived tree data. The coefficient ω (Table 4) which is one of the inputs for the model inversion should be calculated with field data and compared to the value used in this study. If the difference between the value used for ω in this study and the field value is too large, it would be interesting to re-invert the Li-Strahler model using the field value. The performance of the inversion outputs to estimate the field canopy cover and crown diameter should then be evaluated using field data. The inversion could also be performed using a cone or an ellipsoid with a conical top as a tree crown shape. It would also be interesting to input different tree densities values, e.g. in the form of a tree density image. However, a more accurate image of the proportion of the sunlit background has to be obtained in order to retrieve better results. Every step of the methodology can be subject to improvement. One could first try to get the endmembers signatures to spectrally unmix the five CHRIS images directly. A signature model could provide a sunlit background signature that would take the small trees (and the dead wood) into account and simulate the increasing proportion of bark in the canopy with the viewing angle to provide more realistic sunlit and shadowed canopy signatures. The underestimation of the sunlit background proportion for the A9 viewing angle might then be avoided.

Regarding to the evaluation of the quality of the protection provided by the forest, it is necessary to extend the study area to be able to provide a global overview of the structural characteristic of the whole forested area providing the protection. The inversion of the Li-Strahler model may then require one set of tree parameters per tree species. Besides, on should also collect the meteorological, soil and other kinds of data which influence the quality of the protection provided by the forest.

Moreover, the poor quality of the LiDAR estimates might be improved by using the information contained in the multiple scattering of the waves within the canopy. Kotchenova et al. (2003) recently developed a model which simulates the propagation of LiDAR pulses through forest canopies, taking the multi-scattering events into account. In addition, their model is able to simulate off-nadir and multi-angular observations. The retrieval of forest canopy parameters could be supported by the Earth observation mission Carbon-3D (Hese et al., 2005) which would enable to acquire multi-angular data in the visible, NIR and short-wave infra red part of the electromagnetic spectrum and LiDAR data simultaneously. The Carbon-3D data might help to improve the accuracy of the estimates of canopy parameters by correcting for the contribution of the understory, as suggested by Eriksson et al. (2006).

7 References

ABDOU, W.A., CONEL, J.E., PILORZ, S.H., HELMLINGER, M.C., BRUEGGE, C.J., GAITLEY, B.J., LEDEBOER, W.C., MARTONCHIK, J.V., 2001. Vicarious calibration A reflectance-based experiment with airMISR. *Remote Sensing of Environment* 77, 3, 338-353.

ASRAR, G., MYNENI, R.B., CHOUDHURY, B.J., 1992. Spatial heterogeneity in vegetation canopies and remote sensing of absorbed photosynthetically active radiation: a modelling study. *Remote Sensing of Environment* 41, 2-3, 85-103.

BARNSLEY, M.J., SETTLE, J.J., CUTTER, M.A., LOBB, D.R., TESTON, F., 2004. The PROBA/CHRIS mission: A low-cost smallsat for hyperspectral multiangle observations of the earth surface and atmosphere. *IEEE Transactions on Geoscience and Remote Sensing* 42, 7, 1512-1520.

BOREL, C.C., GERSTL, S.A.W., 1994. Nonlinear spectral mixing models for vegetative and soil surfaces. *Remote Sensing of Environment* 47, 3, 403-416.

BRANG, P., 2001. Resistance and elasticity: Promising concepts for the management of protection forests in the European Alps. *Forest Ecology and Management* 145, 1-2, 107-119.

CHEN, J.M., LIU, J., LEBLANC, S.G., LACAZE, R., ROUJEAN, J.L., 2003. Multi-angular optical remote sensing for assessing vegetation structure and carbon absorption. *Remote Sensing of Environment* 84, 4, 516-525.

DEERING, D.W., ECK, T.F., BANERJEE, B., 1999. Characterization of the reflectance anisotropy of three Boreal forest canopies in spring-summer. *Remote Sensing of Environment* 67, 2, 205-229.

DINER, D.J., ASNER, G.P., DAVIES, R., KNYAZIKHIN, Y., MULLER, J.P., NOLIN, A.W., PINTY, B., SCHAAF, C.B., STROEVE, J., 1999. New directions in Earth observing: Scientific applications of multiangle remote sensing. *Bulletin of the American Meteorological Society* 80, 11, 2209-2228.

DINER, D.J., BRASWELL, B.H., DAVIES, R., GOBRON, N., HU, J., JIN, Y., KAHN, R.A., KNYAZIKHIN, Y., LOEB, N., MULLER, J.P., NOLIN, A.W., PINTY, B., SCHAAF, C.B., SEIZ, G., STROEVE, J., 2005. The value of multiangle measurements for retrieving structurally and radiatively consistent properties of clouds, aerosols, and surfaces. *Remote Sensing of Environment* 97, 4, 495-518.

DORREN, L.K.A., 2003. A review of rockfall mechanics and modelling approaches. *Progress in Physical Geography* 27, 1, 69-87.

ERIKSSON, H.M., EKLUNDH, L., KUUSK, A., NILSON, T., 2006. Impact of understory vegetation on forest canopy reflectance and remotely sensed LAI estimates. *Remote Sensing of Environment* 103, 4, 408-418.

FAO, 2006. Chapter 2: Extent of forest resources. *Global forest resources assessment 2005: Progress towards sustainable forest management*, pp. 11-36.

FRANKLIN, J., STRAHLER, A.H., 1988. Invertible canopy reflectance modelling of vegetation structure in semiarid woodland. *IEEE Transactions on Geoscience and Remote Sensing* 26, 6, 809-825.

FRANKLIN, J., DAVIS, F.W., LEFEBVRE, P., 1991. Thematic Mapper analysis of tree cover in semiarid woodlands using a model of canopy shadowing. *Remote Sensing of Environment* 36, 3, 189-202.

FREY, W., THEE, P., 2002. Avalanche protection of windthrow areas: A ten year comparison of cleared and uncleared starting zones. *Forest Snow and Landscape Research* 77, 1-2, 89-107.

GEMMELL, F., 1998. An investigation of terrain effects on the inversion of a forest reflectance model. *Remote Sensing of Environment* 65, 2, 155-169.

GRANT, L., 1987. Diffuse and specular characteristics of leaf reflectance. *Remote Sensing of Environment* 22, 2, 309-322.

GRIMM, V., WISSEL, C., 1997. Babel, or the ecological stability discussions: an inventory and analysis of terminology and a guide for avoiding confusion. *Oecologia* 109, 323-334.

HALL, F.G., STREBEL, D.E., NICKESON, J.E., GOETZ, S.J., 1991. Radiometric rectification: toward a common radiometric response among multidate, multisensor images. *Remote Sensing of Environment* 35, 1, 11-27.

HEDSTROM, N.R., POMEROY, J.W., 1998. Measurements and modelling of snow interception in the boreal forest. *Hydrological Processes* 12, 10-11, 1611-1625.

HESE, S., LUCHT, W., SCHMULLIUS, C., BARNSLEY, M., DUBAYAH, R., KNORR, D., NEUMANN, K., RIEDEL, T., SCHRÖTER, K., 2005. Global biomass mapping for an improved understanding of the CO2 balance - The Earth observation mission Carbon-3D. *Remote Sensing of Environment* 94, 1, 94-104.

HEWITT, K., 1992. Mountain hazards. *GeoJournal* 27, 1, 47-60.

KEIM, R.F., SKAUGSET, A.E., 2003. Modelling effects of forest canopies on slope stability. *Hydrological Processes* 17, 7, 1457-1467.

KNEUBÜHLER, M., KOETZ, B., RICHTER, R., SCHAEPMAN, M.E., ITTEN, K.I., 2005. Geometric and radiometric pre-processing of CHRIS/PROBA data over mountainous terrain. *3rd ESA CHRIS/Proba Workshop*.

KOETZ, B., 2003. Field data report of SNP2002 campaign, Part of the European Project SPREAD WP1.2. *RSL, University of Zurich*, 59 p.

KOETZ, B., SCHAEPMAN, M., MORSDORF, F., BOWYER, P., ITTEN, K., ALLGÖWER, B., 2004. Radiative transfer modelling within a heterogeneous canopy for estimation of forest fire fuel properties. *Remote Sensing of Environment* 92, 3, 332-344.

KOETZ, B., KNEUBÜHLER, M., WIDLOWSKI, J.-L., MORSDORF, F., SCHAEPMAN, M.E., ITTEN, K.I., 2005. Assessment of canopy structure and heterogeneity from multi-angular CHRIS/PROBA data. *9th International Symposium on Physical Measurements and Signatures in Remote Sensing*, pp. 76-78.

KOTCHENOVA, S.Y., SHABANOV, N.V., KNYAZIKHIN, Y., DAVIS, A.B., DUBAYAH, R., MYNENI, R.B., 2003. Modeling lidar waveforms with time-dependent stochastic radiative transfer theory for remote estimations of forest structure. *Journal of Geophysical Research D: Atmospheres* 108, 15.

KUUSK, A., NILSON, T., 2000. A directional multispectral forest reflectance model. *Remote Sensing of Environment* 72, 2, 244-252.

LACAZE, R., ROUJEAN, J.L., 2001. G-function and HOt SpoT (GHOST) reflectance model application to multi-scale airborne POLDER measurements. *Remote Sensing of Environment* 76, 1, 67-80.

LE ROUX, X., GAUTHIER, H., BÉGUÉ, A., SINOQUET, H., 1997. Radiation absorption and use by humid, savanna grassland: Assessment using remote sensing and modelling. *Agricultural and Forest Meteorology* 85, 1-2, 117-132.

LI, X., STRAHLER, A.H., 1985. Geometric-optical modelling of a conifer forest canopy. *IEEE Transactions on Geoscience and Remote Sensing* 23, 5, 705-721.

LI, X., STRAHLER, A.H., 1986. Geometric-optical bidirectional reflectance modelling of a conifer forest canopy. *IEEE Transactions on Geoscience and Remote Sensing* 24, 6, 906-919.

LI, X., STRAHLER, A.H., 1992. Geometric-optical bidirectional reflectance modelling of the discrete crown vegetation canopy: Effect of crown shape and mutual shadowing. *IEEE Transactions on Geoscience and Remote Sensing* 30, 2, 276-292.

MEA, 2005. Chapter 21: Forest systems. *Ecosystems and human well-being: Current state and trends*. Vol. 1, Washington, DC, pp. 587-621.

MONTGOMERY, D.R., SCHMIDT, K.M., GREENBERG, H.M., DIETRICH, W.E., 2000. Forest clearing and regional landsliding. *Geology* 28, 4, 311-314.

MORSDORF, F., MEIER, E., KOETZ, B., ITTEN, K.I., DOBBERTIN, M., ALLGÖWER, B., 2004. LIDAR-based geometric reconstruction of boreal type forest stands at single tree level for forest and wildland fire management. *Remote Sensing of Environment* 92, 3, 353-362.

MOTTA, R., HAUDEMAND, J.C., 2000. Protective forests and silvicultural stability. An example of planning in the Aosta Valley. *Mountain Research and Development* 20, 2, 180-187.

MYNENI, R.B., ASRAR, G., GERSTL, S.A.W., 1990. Radiative transfer in three dimensional leaf canopies. *Transport Theory and Statistical Physics* 19, 1-54.

PEDDLE, D.R., HALL, F.G., LEDREW, E.F., 1999. Spectral mixture analysis and geometric-optical reflectance modelling of boreal forest biophysical structure. *Remote Sensing of Environment* 67, 3, 288-297.

RAUTIAINEN, M., STENBERG, P., NILSON, T., KUUSK, A., 2004. The effect of crown shape on the reflectance of coniferous stands. *Remote Sensing of Environment* 89, 1, 41-52.

RUTTER, A.J., KERSHAW, K.A., ROBINS, P.C., MORTON, A.J., 1971. A predictive model of rainfall interception in forests, I. Derivation of the model from observations in a plantation of Corsican pine. *Agricutural Meteorology* 9, 367-384.

SCHAAF, C.B., LI, X., STRAHLER, A.H., 1994. Topographic effects on bidirectional and hemispherical reflectances calculated with a geometric-optical canopy model. *IEEE Transactions on Geoscience and Remote Sensing* 32, 6, 1186-1193.

SCHAEPMAN-STRUB, G., SCHAEPMAN, M.E., PAINTER, T.H., DANGEL, S., MARTONCHIK, J.V., 2006. Reflectance quantities in optical remote sensing - Definitions and case studies. *Remote Sensing of Environment* 103, 1, 27-42.

SCHAEPMAN, M.E., KOETZ, B., SCHAEPMAN-STRUB, G., ZIMMERMANN, N.E., ITTEN, K.I., 2004. Quantitative retrieval of biogeophysical characteristics using imaging spectroscopy - A mountain forest case study. *Community Ecology* 5, 1, 93-104.

SCHÖNENBERGER, W., NOACK, A., THEE, P., 2005. Effect of timber removal from windthrow slopes on the risk of snow avalanches and rockfall. *Forest Ecology and Management* 213, 1-3, 197-208.

SCHULZ, J., PIEPEN, H.V.D., 1998, *The Airborne Imaging Spectrometer ROSIS* http://www.op.dlr.de/ne-oe/fo/rosis/home.html. Accessed on 32/01/2007.

SHULTIS, J.K., MYNENI, R.B., 1988. Radiative transfer in vegetation canopies with anisotropic scattering. *Journal of quantitative spectroscopy and radiative transfer* 39, 115-129.

SIDLE, R.C., TSUBOYAMA, Y., NOGUCHI, S., HOSODA, I., FUJIEDA, M., SHIMIZU, T., 2000. Stormflow generation in steep forested headwaters: A linked hydrogeomorphic paradigm. *Hydrological Processes* 14, 3, 369-385.

SINOQUET, H., BONHOMME, R., 1992. Modelling radiative transfer in mixed and row intercropping systems. *Agricultural & Forest Meteorology* 62, 3-4, 219-240.

STOFFEL, M., WEHRLI, A., KUHNE, R., DORREN, L.K.A., PERRET, S., KIENHOLZ, H., 2006. Assessing the protective effect of mountain forests against rockfall using a 3D simulation model. *Forest Ecology and Management* 225, 1-3, 113-122.

STOKES, A., SALIN, F., KOKUTSE, A.D., BERTHIER, S., JEANNIN, H., MOCHAN, S., DORREN, L., KOKUTSE, N., ABD, G.M., FOURCAUD, T., 2005. Mechanical resistance of different tree species to rockfall in the French Alps. *Plant and Soil* 278, 1-2, 107-117.

STRAHLER, A.H., JUPP, D.L.B., 1990. Modelling bidirectional reflectance of forests and woodlands using Boolean models and geometric optics. *Remote Sensing of Environment* 34, 3, 153-166.

SWISSTOPO, *Swiss Grid for GIS applications*, http://www.swisstopo.ch/en/basics/geo/system/swiss_grid. Accessed on 18/03/2007.

VERHOEF, W., 1984. Light scattering by leaf layers with application to canopy reflectance modelling: the SAIL model. *Remote Sensing of Environment* 16, 2, 125-141.

WEIMIN, W., SIDLE, R.C., 1995. A distributed slope stability model for steep forested basins. *Water Resources Research* 31, 8, 2097-2110.

WEISS, M., BARET, F., MYNENI, R.B., PRAGNÈRE, A., KNYAZIKHIN, Y., 2000. Investigation of a model inversion technique to estimate canopy biophysical variables from spectral and directional reflectance data. *Agronomie* 20, 1, 3-22.

WOODCOCK, C.E., COLLINS, J.B., JAKABHAZY, V.D., LI, X., MACOMBER, S.A., WU, Y., COMPANY, A.S., 1997. Inversion of the Li-Strahler canopy reflectance model for mapping forest structure. *IEEE Transactions on Geoscience and Remote Sensing* 35, 2, 405-414.

WOODCOCK, C.E., COLLINS, J.B., GOPAL, S., JAKABHAZY, V.D., LI, X., MACOMBER, S., RYHERD, S., HARWARD, V.J., LEVITAN, J., WU, Y., WARBINGTON, R., 1994. Mapping forest vegetation using Landsat TM imagery and a canopy reflectance model. *Remote Sensing of Environment* 50, 3, 240-254.

XIAO, Q., MCPHERSON, E.G., SIMPSON, J.R., USTIN, S.L., 1998. Rainfall interception by Sacramento's urban forest. *Journal of Arboriculture* 24, 4, 235-243.

ZENG, Y., SCHAEPMAN, M., WU, B., CLEVERS, J.G.P.W., BREGT, A.K., 2007. Forest structural variables retrieval using EO-1 Hyperion data in combination with linear spectral unmixing and an inverted geometric-optical model. *Journal of Remote Sensing* 11, 5, in press.

ZURITA-MILLA, R., CLEVERS, J.G.P.W., SCHAEPMAN, M., 2006. LANDSAT TM and MERIS FR image fusion for land cover mapping over the Netherlands. *2nd Workshop of the EARSeL SIG on Land Use and Land Cover*, pp. 34-40.

ZURITA-MILLA, R., CLEVERS, J.G.P.W., SCHAEPMAN, M.E., KNEUBÜHLER, M., 2007. Effects of MERIS L1b radiometric calibration on regional land cover mapping and land products. *International Journal of Remote Sensing* 28, 3-4, 653-673.

8 Appendices

8.1 Parameters used for the spatial reference in ArcMap

Source: Swisstopo

Projection	Oblique Mercator (azimuth)
Units	Meters
Scale factor at centre of projection	1
Longitude of centre of projection	7° 26' 22.50''
Latitude of centre of projection	46° 57' 08.66''
Azimuth of centre of projection	90°
False Easting	-9419820.5907 m
False Northing	200000 m
X shift	0
Y shift	0
Spheroid	Bessel 1841

8.2 Model inputs

8.2.1 CHRIS viewing angles and solar illumination angles

	Zenith angle (º)	Azimuth angle (º)
AD	-54.59	208.88
AB	-37.76	216.02
A9	21.21	315.20
AA	33.33	341.17
AC	51.15	357.01
Sun	24.30	161.00

8.2.2 Stand and tree characteristics

Parameter	**Notation**	**Unit**	**Value**
Tree density	λ	ha^{-1}	1228
Mean half height of the crown	b	m	2.5
Mean horizontal crown radius	R	m	0.882
Coefficient $\omega = \frac{\text{mean}(r^2)}{\text{variance}(r^2)}$	ω	m^{-2}	1.235
Mean tree height from ground to mid-crown	h	m	9.5

8.2.3 Terrain data

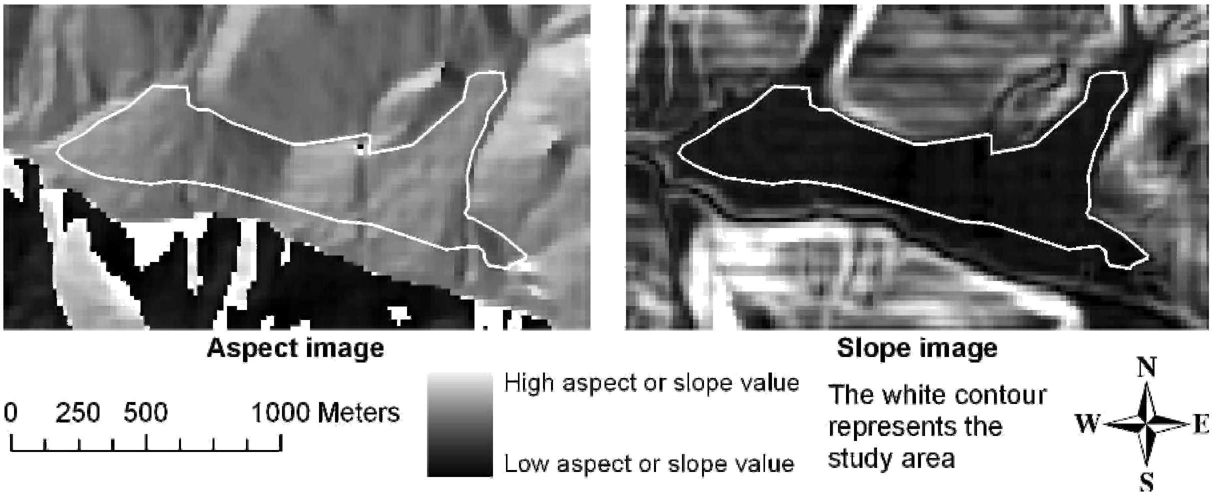

8.2.4 Sunlit background proportions images for the 5 CHRIS angles

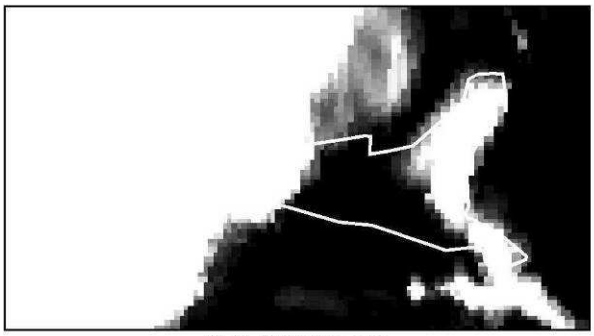
Kg_AC image

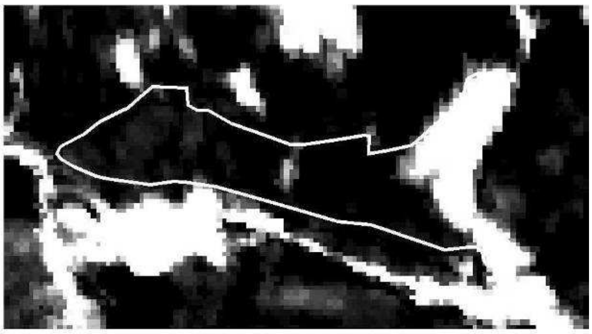
Kg_AA image

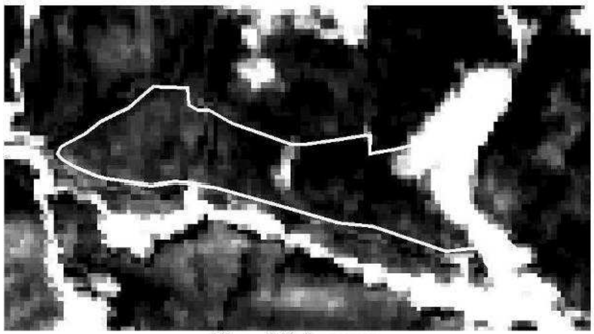
Kg_A9 image

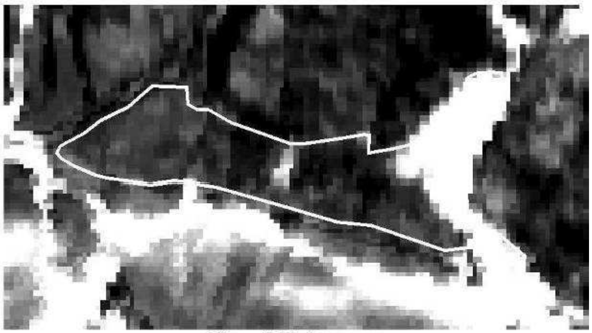
Kg_AB image

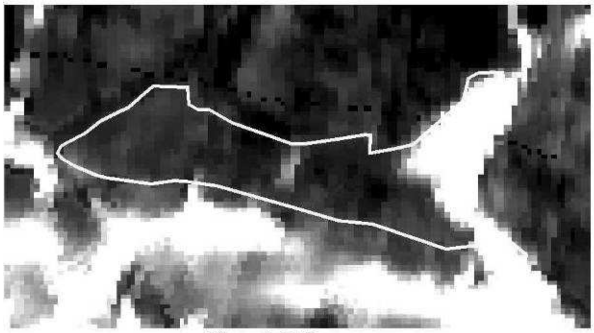
Kg_AD image

The white contour represents the study area

8.3 Flowchart of the first methodology to retrieve the sunlit background proportion images

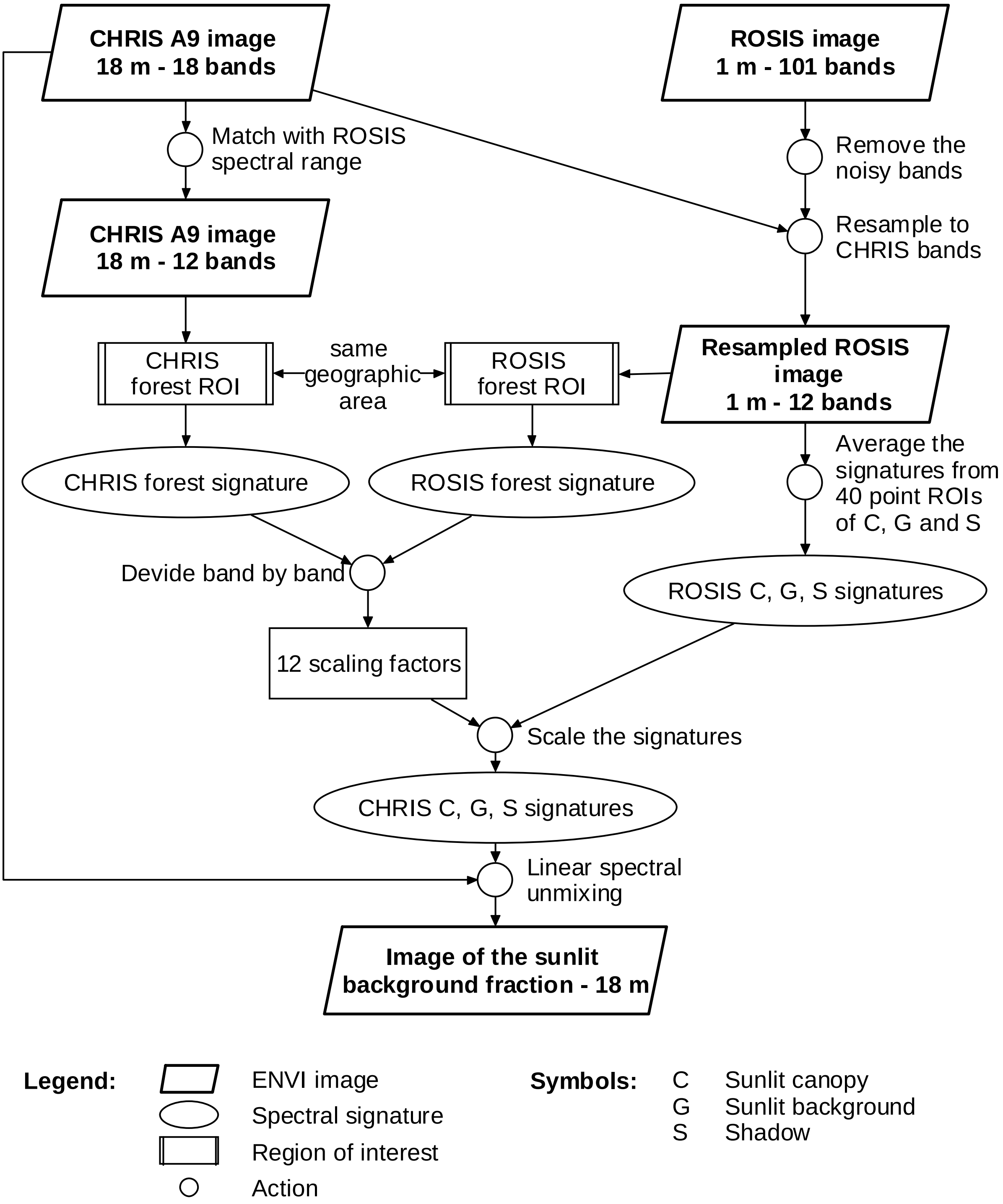

8.4 Unmixing output of the first methodology

With low sunlit background signature

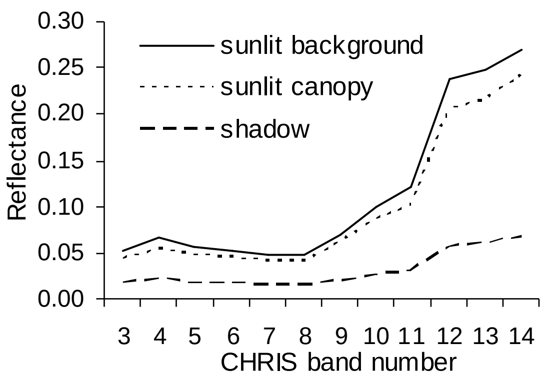

Endmembers signatures

With high sunlit background signature

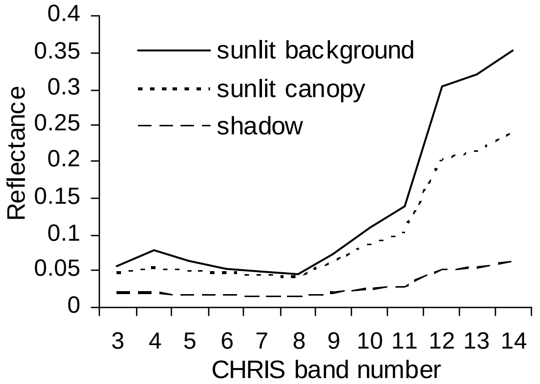

Endmembers signatures

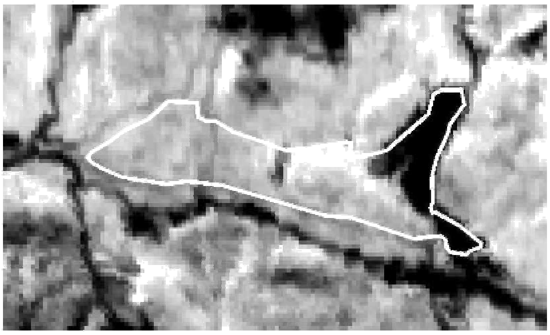

Shadow proportion

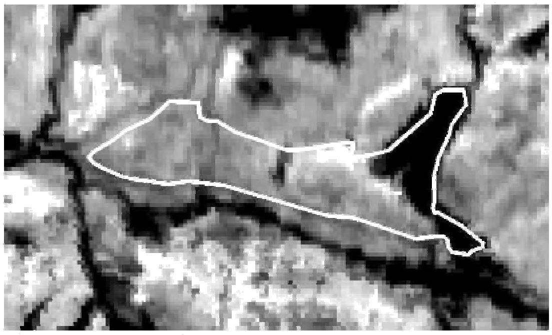

Shadow proportion

Sunlit canopy proportion

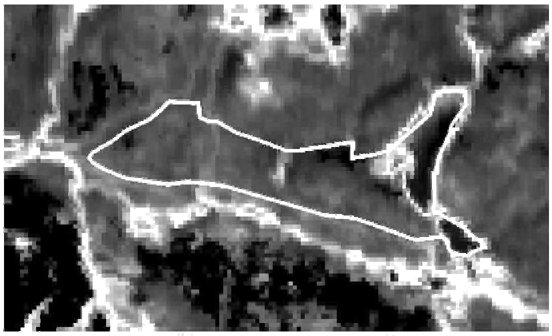

Sunlit canopy proportion

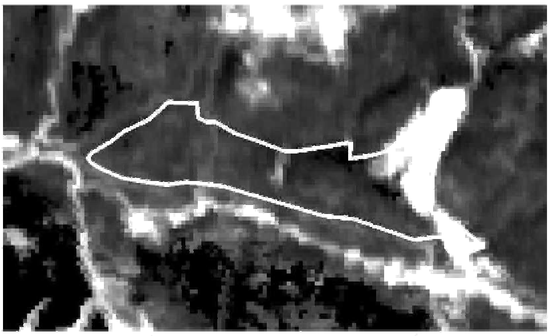

Sunlit background proportion

Sunlit background proportion

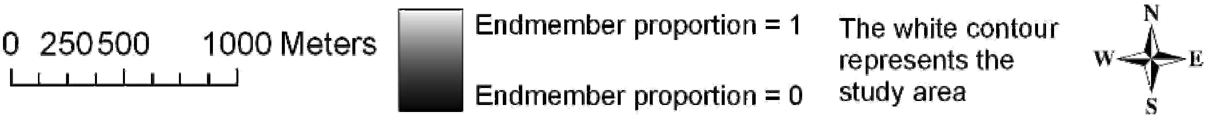

8.5 Geographical characteristics of the images subsets for spatial unmixing

	Extent	Upper left corner coordinates (m)	Lower right corner coordinates (m)
Subset area on the map	540*432 m	x = 813 384 y = 171 882	x = 813 924 y = 171 450
Classification subset in ENVI	540*432 pixels	x = 813 384 y = 171 882	x = 813 923 y = 171 451
CHRIS A9 subset in ENVI	30*24 pixels	x = 813 384 y = 171 882	x = 813 906 y = 171 468

8.6 Map of the number of trees per pixel

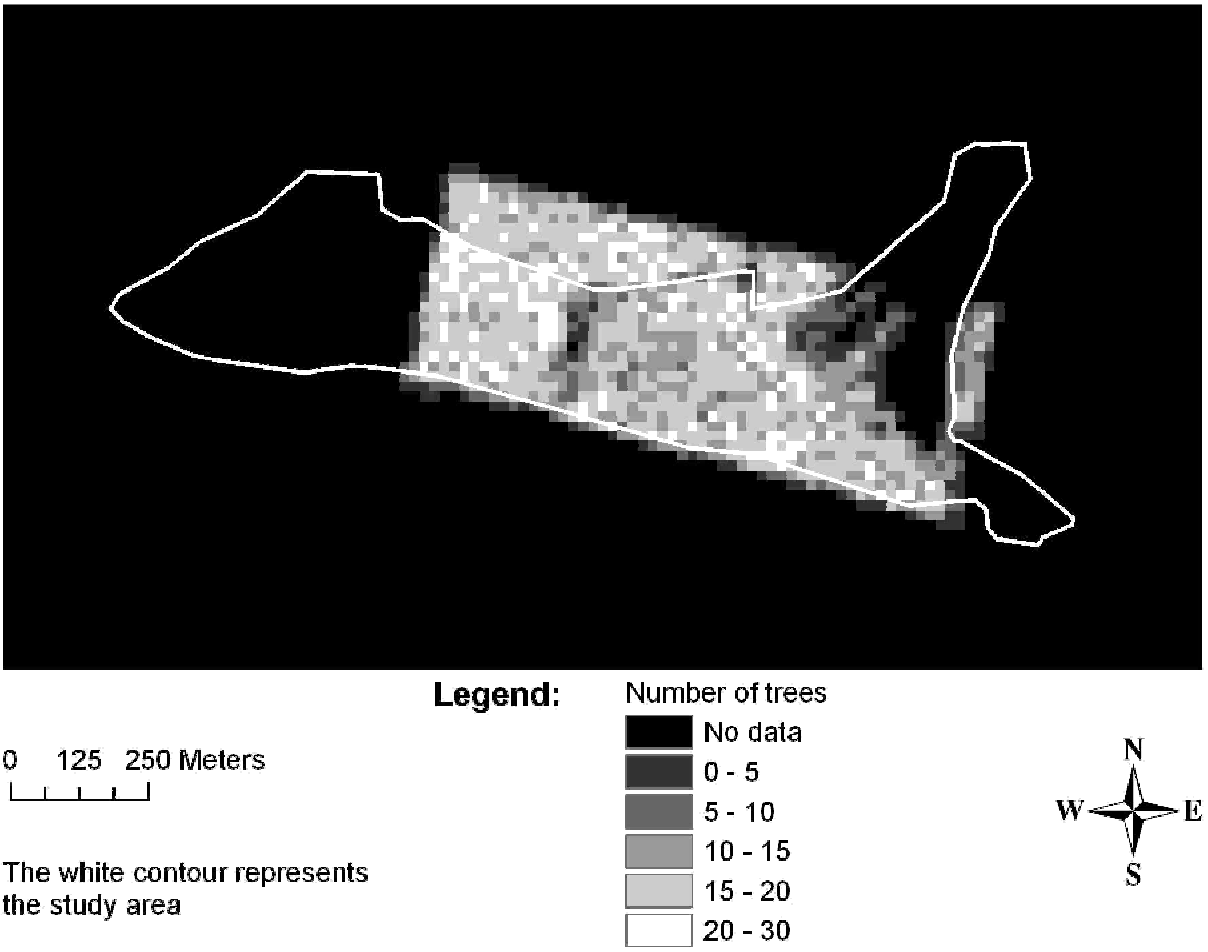

8.7 IDL scripts

8.7.1 Make_no_data.pro: to fill in the pixels without data with “NaN”

```
pro make_no_data
; Created by Jochem Verrelst

cd, 'D:\Valerie\Data\Data_Val\IDL'
envi, /restore_base_save_files
envi_batch_init, log_file='batch.log'

;Open the data file
data=envi_pickfile(Title= 'Select the data file', /no_change)

ENVI_OPEN_FILE,data, r_fid=fid_data
IF (fid_data eq -1)  THEN BEGIN
      ENVI_BATCH_EXIT
      print, 'bad data entry'
      RETURN
ENDIF

ENVI_FILE_QUERY,fid_data,ns=nsc,nl=nlc,nb=nbc, bnames=bnamesCH
dimsc = [-1,0,nsc-1,0,nlc-1]
data = ENVI_GET_DATA(fid=fid_data, dims=dimsc, pos=0)

;Locate the no data pixels and fill them with "NaN"
data[where(data lt -1)]=!VALUES.F_NAN

;Save the output file to disk
bnames=['canopy_cover']
descrip='pixel_canopy_cover'
file_type=ENVI_FILE_TYPE('ENVI Standard')
ENVI_WRITE_ENVI_FILE, data, out_name='canopy_cover', $
file_type=file_type, bnames=bnames, descrip=descrip

end
```

8.7.2 Overlay_all_data.pro: to set to NaN all the pixels having NaN or 0 in one of the model output or reference or mask images

```
pro overlay_all_data
; 190206 created by Jochem Verrelst

;PURPOSE
; 1- This script first loads all the data in a multi-layer "matrix"
; 2- Then set to NaN all the pixels having NaN or 0 in any layer
; 3- Then it saves the multi-layer "matrix" with the NaN pixels
;    to an ENVI file (one band per layer)
; 4- Finally, it calculates the number of usable pixels



cd, 'D:\Valerie\Data\Data_Val\IDL'

; envi, /restore_base_save_files
envi_batch_init, log_file='batch.log'




; 1- Open the model output files
modeloutputs=envi_pickfile(Title= 'Select the model outputs',$
             /multiple_files, /no_change)
;Sort the model output layers alphabetically
modeloutputs=modeloutputs[SORT(modeloutputs)]

valid=envi_pickfile(Title= 'Select the reference data', /no_change)
forestmask=envi_pickfile(Title= 'Select the mask', /no_change)

; Put all the paths together
; so that they can all be opened in one loop.
allpath=[valid, modeloutputs, forestmask]

a=N_ELEMENTS(allpath)
FOR i=0, a-1 DO BEGIN
    modelo=allpath(i)
    ENVI_OPEN_FILE,modelo, r_fid=fid_modelo
        IF (fid_modelo eq -1)  THEN BEGIN
           ENVI_BATCH_EXIT
          PRINT, 'bad data entry'
           RETURN
        ENDIF
    ENVI_FILE_QUERY,fid_modelo,ns=nso,nl=nlo,nb=nbo,bnames=bnameso
    dimso = [-1,0,nso-1,0,nlo-1]
    data = ENVI_GET_DATA(fid=fid_modelo, dims=dimso, pos=0)
        IF i EQ 0 THEN BEGIN
        new=SIZE(data,/dimensions)
        alldata=FLTARR(new[0], new[1],a)
        ENDIF
    alldata[*,*,i]=data
ENDFOR


; 2- Set to NaN all the pixels having NaN or 0 in any layer
FOR b=0, a-1 DO BEGIN
    FOR c=0, new[1]-1 DO BEGIN
    v=WHERE(~FINITE(alldata[*,c,b]) or alldata[*,c,b] eq .0)
```

```
    if v[0] ne -1 then   alldata[v,c,*]=!Values.F_NAN
    ENDFOR
ENDFOR




; 3- Save the multi-layer "matrix" with the NaN pixels to an ENVI file
; We are interested in
; 5, 4 (without AC) or 3 (without AC and AA) viewing angles
IF a-2 eq 5 THEN bnames=['ref','A9','AA','AB','AC','AD','forest mask']
IF a-2 eq 4 THEN bnames=['ref','A9','AA','AB','AD','forest mask']
IF a-2 eq 3 THEN bnames=['ref','A9','AB','AD','forest mask']

descrip='All layers are stacked'
file_type=ENVI_FILE_TYPE('ENVI Standard')
ENVI_WRITE_ENVI_FILE, alldata, out_name='alldata', $
file_type=file_type, bnames=bnames, descrip=descrip




; 4- Calculate the number of usable pixels:
; Put the reference data in a line
ref_line=REFORM(alldata[*,*,0],N_ELEMENTS(alldata[*,*,0]))

; Locate the NaN pixels from the line and
; then calculate the number of 'valid' elements in the line
; = number of usable pixels
ref_no_nan=ref_line[WHERE(FINITE(ref_line))]
print, 'number of usable pixels: ', N_ELEMENTS(ref_no_nan)


end
```

8.8 Map of the validation samples

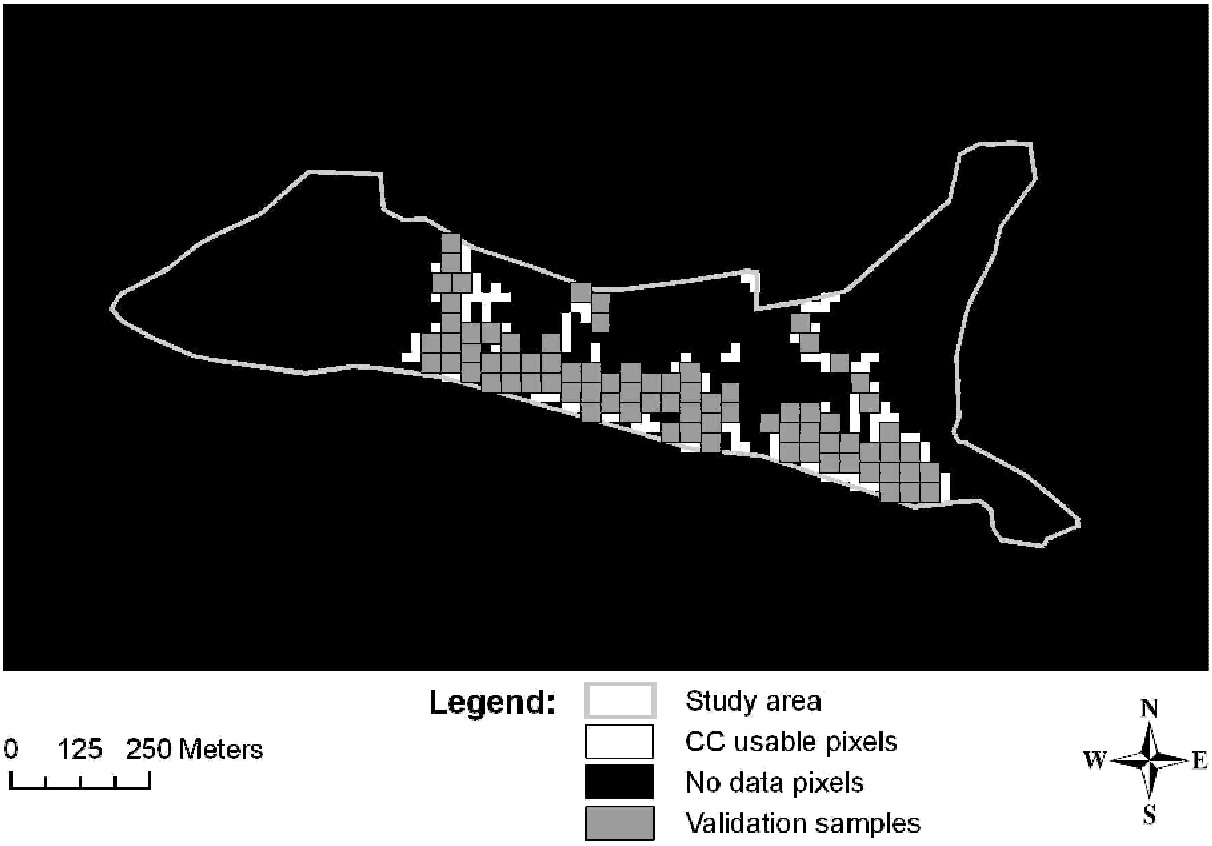

8.9 Confusion matrix and accuracies of the classification of the ROSIS image

		Ground truth						Error of commission		User accuracy
	Class name	Sunlit background	Sunlit canopy	Shadow	Riverbed	Road	**total**	Pixels	%	
Classification result	Sunlit background	50	7	0	0	0	**57**	7	12.3	87.7
	Sunlit canopy	4	142	1	0	0	**147**	5	3.4	96.6
	Shadow	0	6	56	0	0	**62**	6	9.7	90.3
	Riverbed	0	0	0	20	1	**21**	1	4.8	95.2
	Road	0	0	0	3	9	**12**	3	25.0	75.0
	Total	**54**	**155**	**57**	**23**	**10**	**299**	**22**	**7.4**	**92.6**
Error of omission	Pixels	4	13	1	3	1	**22**			
	%	7.4	8.4	1.8	13.0	10.0	**7.4**			
Producer accuracy		**92.6**	**91.6**	**98.2**	**87.0**	**90.0**	**92.6**			

Overall classification accuracy:	92.6%
Kappa coefficient:	0.89